Escola de Camins
Escola Tècnica Superior d'Enginyeria de Camins, Canals i Ports
UPC BARCELONATECH

MASTER FINAL THESIS

A Regional Assessment on the Influence of Climate Change on Summer Rainfall:

An application to shallow landsliding in Wanzhou County, China

Final Thesis developed by:
Joaquin Vicente Consunji Ferrer

Directed by:
Vicente Cesar De Medina Iglesia
Carolina Puig Polo
Marcel Hürlimann

Master of Science in
Flood Risk Management

Barcelona, August 2021

Erasmus Mundus Programme in Flood Risk Management

Erasmus Mundus Masters Programme in Flood Risk Management

A Regional Assessment on the Influence of Climate Change on Summer Rainfall:

An application to shallow landsliding in Wanzhou County, China

Joaquin Vicente Consunji Ferrer

Master of Science Thesis
August 2021

Univerza v Ljubljani

A Regional Assessment on the Influence of Climate Change on Summer Rainfall:

An application to shallow landsliding in Wanzhou County, China

Master of Science Thesis
by

Joaquin Vicente Consunji Ferrer

Supervisors:
Vicente Cesar De Medina Iglesias (UPC Barcelona)
Carolina Puig Polo (UPC Barcelona)
Marcel Hürlimann (UPC Barcelona)

Examination committee
Vicente Cesar De Medina Iglesias (UPC Barcelona)
Allen Bateman Pinzon (UPC Barcelona)
Raul Sosa Perez (UPC Barcelona)

This research is done for the partial fulfilment of requirements for the Master of Science degree in the Erasmus Mundus Flood Risk Management Programme.

Barcelona
August 2021

Abstract

Fatal landslides are devastating and widespread geohazard events that have affected millions of people and claimed the lives of thousands around the globe. Rainfall-induced landslides can occur at scales and magnitudes resulting in catastrophic damage and fatalities. Changes in climate have significantly changed rainfall patterns, manifesting in more frequent extreme rainfall events around the world. The results of which have led to an increase in fatal landslides triggered by rainfall that is aggravated by human activity along sloped areas. Therefore, integrating climate projections with landslide susceptibility models will be crucial in assessing risk in the future.

This study looks into the future of evolving triggering rainfall conditions in a changing climate, and aims to establish a link to tools in the present to assess shallow landslide susceptibility. Focus is given to the triggering rainfall conditions represented by extreme daily rainfall and mean seasonal rainfall. The study site selected in this research was Wanzhou County, China. This county lies in a region of China that receives 90% of its annual rainfall during the summer months. The effect of which is observed with 80% of shallow landslides occurring between June to August from 1995-2005.

A methodology was developed to determine the triggering rainfall conditions from historical landslides, assess the rainfall conditions in the present, and bias-correct climate model outputs to obtain future projections for Wanzhou County. The results delivered in this research project provides practical value in integrating the climate change projections as inputs to physically-based shallow landslide susceptibility model inputs.

This study finds that the historical 30-day antecedent rainfall conditions that triggered shallow landslides during the summers of 1995 to 2005 were statistically similar to the mean seasonal rainfall derived from May to August, over the same period of time. This indicates that the mean seasonal rainfall can adequately represent the antecedent rainfall that can trigger shallow landslides over the summer season. The analysis of the present extreme daily rainfall finds that a large central area of Wanzhou along the Yangtze River is currently exposed to high magnitude, low frequency events. The spatial distribution of extreme daily rainfall patterns suggests that the compounding events due to shallow landslides, urban floods or flash floods along the Yangtze River should be thoroughly investigated.

In order to assess climate change, an ensemble of four Regional climate model (RCM) outputs was considered. The RCM outputs were bias-corrected based on the daily distribution of precipitation observed between 1980-2018. The trends for extreme

daily rainfall and mean seasonal rainfall were corrected independently. The climate change analysis derived future Climate Change Factors (CCFs) for scenarios in the Mid 21st Century (2021-2060) and the Late 21st Century (2061-2100). The climate change projections show a decrease in magnitude of extreme daily rainfall in the Mid 21st century. The Late 21 Century ensemble projections indicate a similar increases in magnitude for extreme daily rainfall and mean seasonal rainfall. The coefficient of variation of the ensemble reveals less uncertainty in the ensemble projections for extreme daily rainfall compared to that of the mean daily rainfall.

This research project delivered proof-of-concept for a methodological framework to derive shallow landslide triggering rainfall scenarios from climate model outputs. The presentation of the results and the identification of sources of uncertainties in this study demonstrated a viable link between for climate change projections to provide future rainfall scenarios as inputs for physically-based shallow landslide susceptibility models.

Acknowledgments

This research would not have been possible without the supervisory committee at the *Universitat Politècnica de Catalunya.* I would like to extend my deepest gratitude to Vicente Medina for the brilliant scientific discussions and the deeply insightful life conversations over our cups of coffee. I am extremely grateful to Marcel Hürlimann for trusting in my ability to deliver such extensive work in your research group, and guiding me during our weekly scientific discussions. I am thankful to Carol Puig for directing my thesis away from the infeasible, and rekindling my excitement for field work and travel. I would like to extend my sincere thanks to Zizheng Guo for the trust to support your doctoral research. I also wish to thank Ona Torra and Claudia Abanco for sharing your studies and insights to improve my research project. I am thankful to Schalk Jan van Andel for the insight in finalizing this thesis.

I gratefully acknowledge the opportunity provided by the Erasmus Mundus Flood Risk Management Programme consortium and the Erasmus+ Scholarship to pursue my graduate studies. I am grateful to all the professors and lecturers in the consortium who have dedicated time and effort to provide meaningful education throughout this pandemic.

I'm thankful for the many life lessons I've learned from my FRM8 batchmates. I'm grateful to Marcos, Eugen, Manuel, Rodrigo, and Siamak; thank you for your friendship and all our adventures during this pandemic. A special thanks to Dominique, Analia, Siva, Faisal, Tharindu, Amin, Helen, Nele, Alina, Camilo, Valeria, Manoel, and Yue for the debates and discussions during our case studies that have expanded my perspective. Thank you, Buse; you were always there to support, and motivate me.

I'm deeply thankful to my family in Galizano for being home away from home. I owe my deepest gratitude to my mom, dad, and brother. Thank you for the endless encouragement, love and support. You are my pillars.

This masters research was preformed in the middle of the COVID-19 pandemic. I owe a debt of gratitude to all those who have supported me in completing this program.

Contents

Abstract 1

Acknowledgments 3

Contents 5

1 Introduction 1
- 1.1 Background . . . 1
- 1.2 Formulation of Research Questions . . . 1
- 1.3 Study Area . . . 6
- 1.4 Research Objectives . . . 7
- 1.5 Innovation and Practical Value . . . 8

2 State of the Art 9
- 2.1 Definition of Terms . . . 9
  - 2.1.1 Triggering Rainfall Conditions . . . 9
  - 2.1.2 Extreme and Mean Daily Rainfall Conditions . . . 10
- 2.2 Determination of Triggering Rainfall Conditions . . . 12
- 2.3 Shallow Landslide Susceptibility and Climate Change . . . 16

3 Case Study on Wanzhou County, China 19
- 3.1 General Site Description . . . 19
- 3.2 Landslide Studies in Wanzhou County . . . 20
- 3.3 Shallow Landslides in Wanzhou . . . 24
- 3.4 Climate Impact Assessments on the Upper Yangtze River Basin . . . 26

4 Methodology 33
- 4.1 Methodological Framework . . . 33
- 4.2 Precipitation Data and Climate Model Outputs . . . 33
  - 4.2.1 Gridded Precipitation Observations . . . 33
  - 4.2.2 Multi-model Climate Projection Ensemble . . . 36
- 4.3 Reconstruction of Triggering Rainfall Conditions . . . 39
- 4.4 Extreme Daily Rainfall Analysis . . . 41
- 4.5 Climate Change Analysis . . . 44
  - 4.5.1 Bias Correction Methodology . . . 44

4.5.2 Quantile Delta Mapping 45
4.5.3 Cross-Validation for Bias-corrected Daily Rainfall 49
4.5.4 Validation for Bias-corrected Extreme Daily Rainfall 50
4.5.5 Climate Change Factors 51

5 Results and Discussion **53**
5.1 Part 1: The Reconstruction of Triggering Rainfall Conditions 53
5.1.1 Triggering Rainfall Conditions in Summer 54
5.1.2 An Assessment of Temporal Uncertainty in the Inventory . . . 63
5.1.3 An Analysis of the Reconstructed Antecedent Rainfall 76
5.2 Part 2: An Analysis of the Present Summer Season Rainfall 78
5.2.1 A Spatio-Temporal Analysis of Mean Monthly Rainfall 78
5.2.2 Analysis of the Mean Seasonal Rainfall Reference Scenario . . . 84
5.2.3 An Analysis of Extreme Daily Rainfall over Wanzhou 88
5.2.4 An Analysis of the Extreme Daily Rainfall Reference Scenario . 95
5.3 Part 3: Projected Summer Rainfall Under Climate Change 97
5.3.1 Validation of Bias Correction by Quantile Delta Methods 98
5.3.2 Climate Change Projections for Mean Seasonal Rainfall 104
5.3.3 Climate Change Projections for Extreme Daily Rainfall 107

6 Conclusions and Recommendations **115**

Bibliography **123**

List of Figures

1.1 Location map and the digital elevation model of Wanzhou County within China depicting the locations of the Tangjiao, Sanzhouxi, and Jinzhuquji landslide events [18]. 6

1.2 Schematic landslide-climate modelling logical framework. Figure cited from Gariano & Guzzetti [3]. 8

2.1 Definition of time scales for triggering rainfall conditions for the event rainfall (*Pe*) and the 30-day antecedent rainfall (*Pa*). 10

2.2 Definition of time scales for rainfall considered under climate scenarios. Extreme daily rainfall (red), mean monthly rainfall (yellow), and mean seasonal rainfall (green). 11

2.3 Comparison of the relationship between cumulative rainfall before failure and daily rainfall at failure over the Nepal Himalayas for different durations of consideration. The broken line (guide line) represents daily and cumulative rainfalls are the same at failure. Cited from Dahal & Hasegawa [33]. 14

3.1 Lithological units in Wanzhou district: J_1 (quartz sandstone, shale, limestone), J_2 (sandy mudstone, quartz sandstone, shale, feldspatite, siltstone), J_3 (quartz sandstone, aubergine mudstone, lithic sandstone, shale), T_1 (dolomitic limestone, flaglike limestone), T_2 (argillaceous limestone, dysaerobic fauna, aubergine mudstone, calcareous shale), and T_3 (lithic Sandstone, arenaceous shale, coal seam). Cited from Huang *et al.* [20]. 20

3.2 Locations of the 639 distinct landslides inventoried within the Wanzhou district from 1970 to 2013 Cited from Huang *et al.* [20]. 21

3.3 Susceptibility map for Wanzhou County developed in a study with self-organizing -map network and extreme learning machine. Cited from Huang *et al.* [20]. 22

3.4 Location of the Sunjia landslide, Wanzhou County, Three Gorges Reservoir, China. Cited from Xiao *et al.* [21]. 23

3.5 Histogram of monthly occurrences of shallow landslide events in the inventory from 1995 to 2005. 24

3.6 Monthly rainfall derived from the rain gauge observations within the study area from 1954 to 2015. . . . 25
3.7 Shallow landslide occurrences from the Wanzhou Institute of Geological Environment Monitoring and the location of the Chinese Meteorological Agency rain gauge. . . . 26
3.8 Major river basins across China with shaded topography (meters). Cited from Tong *et al.* [37]. . . . 27
3.9 Hydrological basins within the Upper Yangtze River Basin. Cited from Huang *et al.* [38]. . . . 28
3.10 Near-future multi-year average changes in precipitation (mm/day) over the UYRB under the RCP8.5 scenarios compared to reference observations from 1971 to 2000. Cited from Huang *et al.* [38]. . . . 29
3.11 Mean monthly precipitation (mm) over the Yangtze River Basin from 1990 to 2010 derived from observations (CN05 in black), reanalysis model (ERA-Interim in blue) and the RCM model (RegCM in red). Cited from Gao *et al.* [41]. . . . 30

4.1 Conceptual methodological framework of this research project. . . . 34
4.2 Spatial distribution of shallow landslides, center points of the CMFD gridded observations, and the location of the available rain gauge. . . . 36
4.3 Schematic of the extraction of event rainfall (Pe) and the 30-day for antecedent rainfall (Pa) corresponding to landslide occurrences (red points) for one CMFD pixel time series within the study area (encircled in red in the insert map). . . . 40
4.4 Flowchart of data required and bias correction methods and workflows to derive climate change projections for extreme daily rainfall and antecedent rainfall. . . . 45
4.5 Flowchart of cross-validation procedure from splitting the data into training and testing to deriving performance metrics. . . . 49

5.1 A 2D density distribution of event rainfall versus the 30-day antecedent rainfall for the reconstructed rainfall conditions for June-August 1995 to 2005. . . . 54
5.2 Histograms and density distributions of seasonal rainfall reconstructions for event rainfall (in blue along the left column panes), and the antecedent rainfall (in green along the right column panes. . . . 56
5.3 Time series of average monthly recharge parameters (C_r) over the study area for the period of 1995-2005. *Data from: [65].* . . . 57
5.4 Monthly average recharge parameters (C_r) from 1995 to 2005. *Data from: [65].* . . . 58

5.5 Yearly average recharge parameters (C_r) from May to July of 1995 to 2005. *Data from: [65].* 59
5.6 Histogram (A) and density distribution (B) of the reconstructed 30-day mean effective antecedent recharge for landslides occurring between June to August 1995 to 2005. 60
5.7 A 2D density distribution of Event Rainfall versus the 30-day Effective Antecedent Recharge from June to August 1995 to 2005. 61
5.8 A comparison of the effect of the time-shifting algorithm (in red circles) for 2 to 11 day periods (left to right, top to bottom) and the difference between the original record dates (in blue triangles) with focus on reconstructed rainfall conditions occurring during summer season months from 1995-2005 with no estimated recharge. 62
5.9 A comparison of the percentage of the inventory affected by the detection of a maximum event rainfall for different periods of days prior to the record date 64
5.10 An inter-comparison between the percentage of the inventory affected by the detection of maximum event rainfall between paired intervals of consecutive days prior to the record date. 65
5.11 A 2D density plot of the event rainfall and the antecedent rainfall with a 7-day uncertainty period applied occurring from June-August 1995-2005. 67
5.12 A 2D density plot of the event rainfall and the effective antecedent recharge resulting 7-Day uncertainty period occurring from June-August 1995-2005. 68
5.13 Box Plot comparison of the 30-day mean antecedent rainfall for landslides occurring in June-August with the consideration of temporal uncertainty under different intervals of days prior to the inventory record date. 70
5.14 Density distributions of 30, 15 and 10-day mean antecedent rainfall (top to bottom) reconstructed around the original inventory record date and results of the time-shifted results of 2 to 11 days. 72
5.15 Comparison of the empirical cumulative distribution functions ($F(x)$) derived from the original record date and the results of a 7-day period of uncertainty for 30, 15 and 10 day periods of antecedent rainfall (top to bottom). 74
5.16 Comparison of the density distributions of antecedent rainfall of the reconstructed inventory with a 7-day window of uncertainty and the distribution antecedent rainfall in CMFD observations from 1995 to 2005. 76

5.17 Average seasonal mean rainfall (MSR) over the study area from May to August 1979 to 2018 over Wanzhou (blue solid line), with maximum MSR in the study area (red dashed line), and the minimum MSR (yellow dashed line) . . . 79

5.18 Average seasonal mean rainfall (MSR) from May to August 1979 to 2018 over Wanzhou (blue dashed line), with the standard deviation (in error bars). . . . 80

5.19 Mean monthly rainfall (MMR) showing the average MMR value derived from the period of 1979-2018 for the months of May (A), June (B), July (C), and August (D). . . . 81

5.20 Coefficients of variation in mean monthly rainfall derived over the period of 1979 to 2018 for the months of May (A), June (B), July (C), and August (D). . . . 83

5.21 Reference scenario derived from mean seasonal rainfall derived from May to August over the period of 1979 to 2018. . . . 84

5.22 Coefficient of variation measuring the temporal variation in mean seasonal rainfall from 1979 to 2018. . . . 85

5.23 Relative deviation of the reference scenario mean seasonal rainfall from the mean monthly rainfall for the months of May (A), June (B), July (C), and August (D). . . . 87

5.24 Cumulative distribution functions ($F(x)$)derived from mean monthly rainfall values from 1979 to 2018 for May (blue), June (green), July (pink), August (orange), and the mean seasonal rainfall (black). . . . 88

5.25 Density distribution curves derived from mean monthly rainfall values from 1979 to 2018 for May (blue), June (green), July (pink), August (orange), and the MSR (black). . . . 89

5.26 Maximum extreme daily rainfall (A) derived from the monthly block maxima approach, and the relative deviation of the maxima in each grid cell from the spatial mean of maximum daily rainfall (B) from the period of June to August 1979 to 2018. . . . 91

5.27 Minimum extreme daily rainfall (A) derived from the monthly block maxima approach, and the relative deviation of the minima each grid cell from the spatial mean of extreme daily rainfall representing relatively dry years (B) from the period of June to August 1979-2018. . . . 92

5.28 Skewness coefficient of the extreme daily rainfall of each grid cell within the study area for 1979 to 2018. . . . 93

5.29 Return period curves derived from Gumbel fittings in all pixels across the study area (grey lines) with the relationship curves for the mean extreme daily rainfall (blue), the maximum (green), and the minimum (red). 95
5.30 Comparison of the spatial distribution in extreme daily rainfall corresponding to return periods of 10, 20, 50 and 100 years (left to right, top to bottom) calculated through the Gumbel fittings. 96
5.31 Box plot comparison of cross-validation performance of the daily rainfall bias correction measured by mean average error (MAE) for each grid point results of the four GCM-RCM ensemble member combinations. . 99
5.32 Box plot comparison of cross-validation performance of the daily rainfall bias correction measured by root-mean squared error (RMSE) for each grid point results of the four GCM-RCM ensemble member combinations. 100
5.33 Comparison of validation performance of the extreme daily rainfall bias correction measured by mean average error (MAE) for each grid point results of the four GCM-RCM ensemble member combinations. 101
5.34 Comparison of validation performance of the extreme daily rainfall bias correction measured by root-mean squared error (RMSE) for each grid point results of the four GCM-RCM ensemble member combinations. . 102
5.35 Comparison of validation performance of the extreme daily rainfall bias correction measured by Pearson correlation coefficient for each grid point results of the four GCM-RCM ensemble member combinations. . 103
5.36 Mean seasonal rainfall climate change factors (CCF_{MSR}) derived from the ensemble mean for the months of May to August for the Mid 21st Century (A) and Late 21st Century (B) scenario projections. 105
5.37 Coefficients of variation of the ensemble projections of climate change factors (CCF_{MSR}) derived from mean seasonal rainfall for May to August for the Mid 21st Century (A) and Late 21st Century (B) scenario projections. 106
5.38 Mid 21st Century scenario projections of extreme daily rainfall climate change factors ($CCF_{EDR,T}$) for return periods (T) of 5, 10, 50 and 100 years derived from the ensemble mean projections covering the months of June to July. 109
5.39 Late 21st Century scenario projections of extreme daily rainfall climate change factors ($CCF_{EDR,T}$) for return periods (T) of 5, 10, 50 and 100 years derived from the ensemble mean projections covering the months of June to July. 110

5.40 Coefficients of variation for Mid 21st Century scenario projection ensemble projections of climate change factors ($CCF_{EDR,T}$) with return periods (T)of 5, 10, 50 and 100 years derived from the ensemble mean projections covering the months of June to July. 112
5.41 Coefficients of variation for Late 21st Century scenario projection ensemble projections of climate change factors ($CCF_{EDR,T}$) with return periods T of 5, 10, 50 and 100 years derived from the ensemble mean projections covering the months of June to July. 113

List of Tables

4.1 Summary of ensemble specifications. 38
4.2 Definitions of climate change scenarios. 45

5.1 Summary of the Kolmogorov-Smirnov (KS) Test results between CDFs of the original record date data and the 7-day time-shifted data for different antecedent durations. 75
5.2 Summary of minimum, mean and maximum Gumbel fit parameters. . . 94
5.3 Summary Goodness-of-fit test statistics with p-values (in parenthesis). 94
5.4 Summary of the Kolmogorov-Smirnov (KS) test between bias-corrected ensemble members with minimum, mean and maximum test statistics and p-values (in parenthesis). 102
5.5 Summary of the bias-corrected RCM cells passing a Kolmogorov-Smirnov Test and the total number of cells corrected with a $p - value \geq 0.05$ . . 104

List of Abbreviations

AD	Anderson-Darling
AHI	Advanced Himawari Imager
APHRODITE	Asian Precipitation—Highly Resolved Observational Data Integration Towards the Evaluation of Water Resources
CAR	Calibrated Antecedent Rainfall
CCF	Climate Change Factor
CDF	Cumulative Distribution Function
CMA	Chinese Meteorological Agency
CMFD	China Meteorological Forcing Dataset
CMIP5	Coupled Model Intercomparison Project 5
CORDEX	Coordinated Downscaling Experiment
CVM	Cramer-von-Mises
EDR	Extreme Daily Rainfall
EVS	Extreme Value Statistics
FSLAM	Fast Shallow Landslide Assessment Model
GCM	Global Climate Model
GERICS	Climate Service Center Germany
GEV	General Extreme Value
GLDAS	Global Land Assimilation System
GPM	Global Precipitation Measurement
HadGEM	Hadley Global Environment Model
KS	Kolmogorov-Smirnov
MAE	Mean Absolute Error
MMR	Mean Monthly Rainfall

MSR	Mean Seasonal Rainfall
MPI	Max Planck Institute
MPI-ESM	Max Planck Institute Earth System Model
NDVI	Normalized Difference Vegetation Index
RainFARM	Rainfall Downscaling by a Filtered Auto-Regressive Model
RCM	Regional Climate Model
RCP	Representative Concentration Pathways
REA	Reliable Ensemble Averaging
RegCM	Regional Climate Model of the International Centre for Theoretical Physics'
REMO	Regional Climate Model of the Climate Service Center Germany
RMSE	Root-mean-squared Error
QDM	Quanntile Delta Mapping
QM	Quantile Mapping
TMPA	TRMM Multi-satellite Precipitation Analysis
TRMM	Tropical Rainfall Measuring Mission
TRIGRS	Transient Rainfall Infiltration and Grid-Based Regional Slope-Stability Model
UYRB	Upper Yangtze River Basin
YRB	Yangtze River Basin
WRF	Weather Research and Forecasting

1 Introduction

1.1 Background

Fatal landslides are devastating and widespread geohazard events that have affected millions of people and claimed the lives of thousands around the globe [1]. Froude & Petley [2] have determined that rainfall is the main driver of fatal landslide occurrences between 2004-2016. Furthermore, it was determined that landslides triggered by human activity along the slopes is increasing. As society looks to manage landslide risk in the future, consideration of the causal relationship between landslides and climate change is essential [3]. Therefore, the interaction between rainfall under a changing climate and the increase in human activity is critical to assessing and managing landslide risk in the future.

There is evident impact of anthropogenic influences on the change in climate at a global scale throughout the Industrial Period from 1750-2011 [4]. Centuries of increasing widespread land cover changes driven by human activity have resulted in the reduction of global forest areas [5]. This trend of declining forest cover across the globe affects mountainous and sloped areas through the alteration of vegetation and soil stability characteristics.

The changes in global climate are apparent in the observation of trends in precipitation and records of more frequent extreme precipitation events. An empirical assessment of the upper 0.3% of daily rainfall observations showed a widespread increase in frequency during the past 50 to 100 years [6]. Alexander *et al.* [7] find a period of accelerated global warming between 1964-2013, where 7% more extreme events were observed.

The temporal variation in rainfall characteristics is a significant driver in landslide initiation across the world. A strong correlation between mean monthly rainfall and landslides was observed in Central America, South America, South Asia and East Asia. Increased human activity through land development and illegal mining practices are foreseen to instigate landslides in the future [2].

1.2 Formulation of Research Questions

The relationship between climate change and landslide risk is a critical topic in regions across the globe. Gariano & Guzzetti [3] find a causal relationship between landslides

and climate across literature. Although an increase in risk is expected in the future, quantifying risk to the population and projecting the precise impact of climate change is difficult due to large uncertainty derived from the landslide-climate projection modelling chains. Peres & Cancelliere [8] observed significant indicators of seasonality and inter-annual variation in the occurrence of landslides from 2004-2016. Their findings suggest that antecedent conditions influence soil moisture and interact with mechanical soil properties to increase the probability of slope failure.

This research focuses on rainfall-induced shallow landslides that occur on sloped surfaces and are capable of causing devastating damage and massive fatalities. Li & Mo [9] provide a contemporary classification of shallow landslides determined by the depth of the rupture surface being less than 10 meters, consisting of mostly soil material with possible soft and hard rock from the slip surface. Rainfall-triggered shallow landslides occur due to rainfall events that increase the top-soil water content and pore pressure. In effect, the effective stresses are reduced, the soil is destabilized and a debris flow that can propagate a significant volume of soil mass several kilometers at high velocities can be mobilized. This characteristic propagation of mass particular to the shallow landslide results in deadly debris flows with heightened risk to communities along the flow paths. In cases where soil on a slope with significant soil moisture is subjected to heavy rainfall, a faster propagation of wetting between the soil-bedrock interface can create conditions of landslide initiation [10].

There are multiple approaches in modeling to quantitatively assess shallow landslide susceptibility. The classification of these methods mainly use statistical models, machine learning models and physically-based models. Although data-driven models are reliable and widely accepted, they do not describe the complex interactions occurring and physical processes that govern the behaviour of shallow landslide susceptibility and thus risk in future scenarios [3, 11, 12]. Physically-based models are able to describe the processes of soil-vegetation interactions, influences of event rainfall on infiltration, and the effects of antecedent rainfall events to subsurface flows. These processes are essential to assess the shallow landslide risk in the future under the conditions of a changing climate and changes to land use.

A gap in research on modeling shallow landslide susceptibility under climate change scenarios exists in the inability of current models to incorporate the non-stationary trends of increasing precipitation, and the effects of specific triggers on the magnitude of future landslides. [3] identified these issues and recommended the development of new models to cope with the non-stationary climate characteristics, and investigate temporal variations in risk that are driven by a combination of climate and vegetation changes along the slope environments.

Their research indicates the influence of antecedent rainfall, and land use change scenarios that induce stable slopes into marginally stable conditions, while bringing

marginally stable slopes into critical risk conditions. Modeling climate change requires incorporating interactions between stability under antecedent rainfall events, and changes in vegetation- derived resistance. All are essential when analyzing risks against the future impacts of landslide-triggering extreme precipitation events. Therefore, this research project aimed to address the gap in research when modeling shallow landslide susceptibility under climate change scenarios. A focus on evaluating future rainfall conditions that can trigger shallow landslides was the primary research objective with the question stated as:

What is the influence of climate change on rainfall conditions that could trigger shallow landslides?

In order for this research project to accomplish its main objective, a set of auxiliary objectives were established. The first auxiliary research question revolves around understanding the rainfall conditions that triggered previous shallow landslide events.

Physically-based models require scenarios of triggering rainfall conditions that incorporate the non-stationary trends of increasing precipitation to determining areas at risk under climate change conditions. This study particularly supports the development of rainfall scenarios that are compatible with the The "Fast Shallow Landslide Assessment Model" (FSLAM), developed by [11]. This model utilizes geotechnical and hydrological models to enable the investigation of future climate and land use scenarios involving changes in daily rainfall patterns and soil cohesion. The geotechnical model incorporates cohesion derived from root strength alongside cohesion in the soil matrix to account for vegetation characteristics accompanying environmental changes. Furthermore, the hydrological model combines the influences of antecedent recharge through a steady-state lateral flow, and event precipitation through vertical flow on the water table. While the sensitivity analysis of the model reveals antecedent recharge has a considerable influence over the probability of failure compared to the event rainfall.

A fundamental variable in the performance of models is the antecedent rainfall. It is recognized in literature as an influential factor in the occurrence of soil slips and thus, the initiation of shallow landslides [13]. In the determination of rainfall thresholds for landslide occurrences, approaches with antecedent rainfall conditions comprise the second most used approach. A variety of methods in incorporating antecedent rainfall have been observed, where some studies prefer the use of rainfall indices instead of direct rainfall measurements to account for the infiltration, storage and saturation [14].

The use of indices to represent antecedent rainfall and account for soil storage capacity is an important consideration of the dynamics of soil moisture during event intervals [10]. It is difficult to generalize the approach and threshold to which antecedent rainfall influences shallow landslide initiation due to the regional climate interaction with in situ geotechnical properties and watershed's hydrological characteristics [13].

The importance of antecedent rainfall as a factor for rainfall- triggered landslides was observed in Calabria, Italy, by Polemio & Petrucci [15]. This research project identified shallow landslide triggering rainfall conditions as event rainfall and antecedent rainfall. The first auxiliary research question was formulated to evaluate the rainfall conditions in that past that had led to landslide occurrences in survey inventories and literature. This auxiliary question is stated as:

What rainfall conditions triggered the historic shallow landslides in the study area?

This research question was intended to develop a task to use inventory data to reconstruct the event rainfall, antecedent rainfall, and antecedent recharge in order to derive insight on patterns and trends in landslide triggering at a site-specific scale. The understanding of the rainfall conditions that triggered landslides in the inventory aid to establish a reference to determine rainfall conditions in the present that could trigger landslides in the near future. Thus, an assessment of the present conditions is necessary to capture the recent spatio-temporal patterns.

The findings of Alexander *et al.* [7] indicate that while there is significant warming throughout the 20th century and a general increase in precipitation volume from 1951-2003 was detected at a global level. Donat *et al.* [16] presented an analysis of "wet" and "dry" regions determined by changes in total precipitation from global observation data sets for the period of 1951–1980. Their study showed a statistically significant increase in annual-maximum daily precipitation observed in both wet and dry regions around the globe.

The precipitation observations indicate that the present climate conditions are characterized by the dynamics of a changing climate that have already seasonal volumes of precipitation, and maximum daily precipitation [4]. This insight is critical to the shallow landslide triggering rainfall conditions. An increase in precipitation volume at a seasonal level affects antecedent rainfall conditions, while a trend of increasing maximum daily precipitation could influence the frequency of event rainfall.

Furthermore, the importance of incorporating the accompanying frequency of extreme events is emphasized by Scheidl *et al.* [12] in a study that simulated the interaction of changing vegetation cover with design precipitation events with 100-year recurrence.

Polemio & Petrucci [15] find that the number landslides was correlated to monthly precipitation, wet days and precipitation intensity. Therefore, a site-specific analysis of the prevailing rainfall conditions is essential to establish a reference scenario for future rainfall projections in a changing climate. An auxiliary research question developed to establish a reference scenario based on present rainfall conditions is stated as:

What are the return periods of extreme daily rainfall and the magnitudes of seasonal rainfall?

Gariano & Guzzetti [3] expect an increase in frequency and intensity of severe rainfall events, that will result increase in the number of people ex- posed to landslide risk. Scheidl *et al.* [12] indicated that a general increase in shallow landslide risk was observed under climate change, highlighting the significance of the change in frequency of extreme precipitation events as a triggering mechanism. The incorporation non-stationary events under climate change will enhance the analysis for adaptive management approaches by ac- counting for the influence of the changing climate on the return periods of triggering event rainfall. Therefore, the final auxiliary research question was formulated to assess the change in frequency and magnitude of extreme daily rainfall, and the volume of seasonal precipitation in the future. This research question is formulated as:

How do the distributions and magnitudes of rainfall events change based on climate models projections?

The main goal of the research task following this auxiliary research question is to derive projections of climate change conditions from an ensemble of Regional climate models (RCMs) selected for the study area. An ensemble of three RCMs were utilized by Peres & Cancelliere [8] to investigate landslide-triggering return periods. Although there was an indication of projected increases in the interarrival time between rainfall events, the high spread of spatial variation stipulates the effect of model uncertainty and points to the use of a wider range of models in an ensemble to analyze the impacts of climate change.

An analysis of annual maximum 1-day precipitation events under climate change scenarios by Brönnimann *et al.* [17] shows a shift in seasonality that results in less frequent events. Scheidl *et al.* [12] suggests that in regions where extreme precipitation events are less likely to occur under drying climate scenarios, a decrease in frequency of landslide-triggering events can be expected. Thus, indicating that there is significant uncertainty and variability from assessing landslide risk using rainfall scenarios from projections of the numerous available regional climate models.

Translating projected rainfall magnitudes as direct input to physically-based susceptibility models will introduce significant uncertainty into the risk assessments. Therefore, the perspective in assessing the influence of climate change adapted to this research project manifested in the calculation of a factor of change derived from the climate model projections. This captured relative change in the climate signal that could be applied to the reference scenario in the present to project future events.

1.3 Study Area

Froude & Petley [2] reported a strong correlation between rainfall and landslide occurrence in East Asia. The Wanzhou County in China, shown in Figure 1.1, is an area of particular interest due to the frequency and magnitudes of landslides in contemporary literature.

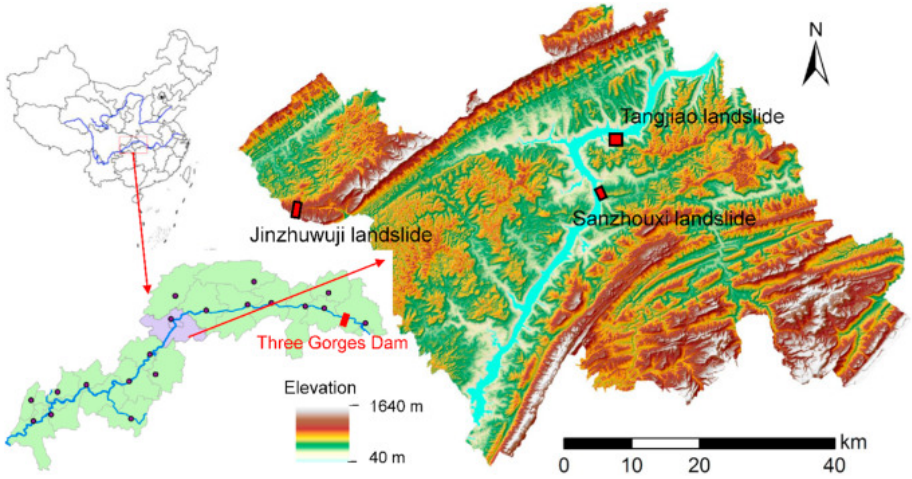

Figure 1.1: Location map and the digital elevation model of Wanzhou County within China depicting the locations of the Tangjiao, Sanzhouxi, and Jinzhuquji landslide events [18].

This area lies within the a subtropical humid monsoon region with a mean annual precipitation of 1191.3 mm. Rainfall between May and September is significant, with 90% of the volume occurring in this period. Intense rainfall exceeding 100 mm/day also occurs during this season. Xiao *et al.* [19].

The heavy rainfall has been attributed as a significant landslide trigger within the study area. Between 1970 and 2013, 639 rock and soil landslides occurred with nearly half the sites being reactivated sites Huang *et al.* [20]. It was found that a confluence of human activity, land use change and heavy rainfall are main drivers for the reactivation of old landslide sites.

Furthermore, large landslide events have also occurred within the Wanzhou County area. In 2013, the Sunja landslide displaced 1.5 million cubic meters of soil over a period of 148 days Xiao *et al.* [21]. Therefore, the frequency and magnitude of landslide occurrences in the study area, together with the significant amount of precipitation over the summer season made Wanzhou County a relevant study are to investigate the research questions proposed in Section 1.2.

1.4 Research Objectives

This section specifies the specific research objectives derived from the primary and auxiliary research questions presented in Section 1.2. This section presents a summary of the objectives of this research project applied over Wanzhou County, China:

- *Develop a methodology to assess rainfall conditions under climate change.*
- *Reconstruct the historical triggering rainfall conditions corresponding to an inventory of shallow landslide events.*
- *Establish reference scenarios for extreme daily rainfall and antecedent rainfall in the present.*
- *Derive climate change factors based on climate model projections for rainfall in future scenarios.*

1.5 Innovation and Practical Value

The aim of this study is to establish a methodology for assessing scenarios of future rainfall events, their relationship with shallow-landslide triggering events, and predicting the changes of these events under climate change.

The practical value of this methodology is in linking climate change modeling chains with physically-based shallow landslide susceptibility models. In the logical framework of landslide-climate modeling chains proposed by Gariano & Guzzetti [3], this research adds innovation in the link between *"Future Climate Projections"* and *"Projected Landslide Models"*, indicated in the red box in Figure 1.2. The scope of this research is limited to using bias correction techniques to create scenarios that incorporate future climate projections that can be beneficial to slope stability modelers.

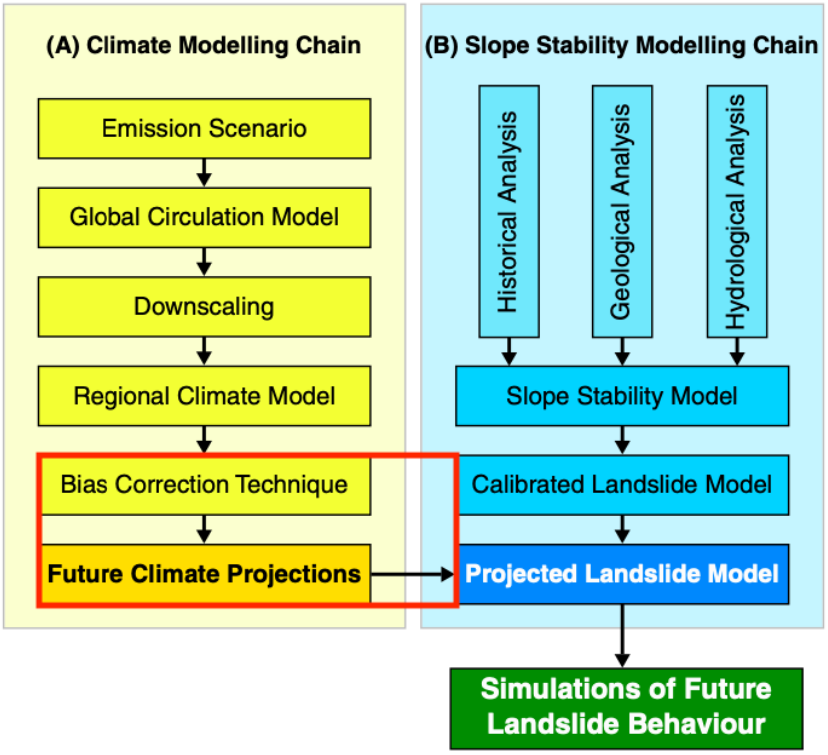

Figure 1.2: Schematic landslide-climate modelling logical framework. Figure cited from Gariano & Guzzetti [3].

2 State of the Art

This chapter reviews related literature to present the state of the art in research on the triggering mechanisms of shallow landslides, and the advances in assessing shallow landslide susceptibility under changing climate conditions.

2.1 Definition of Terms

The primary task of this research project is to establish a methodology to integrate modeling chains from the areas of atmospheric and climate modeling with hydrological and landslide modeling. Thus, it is essential to establish a clear definition of terms to different rainfall events and establish time scales for each term used in this document.

2.1.1 Triggering Rainfall Conditions

The first set of terms revolve around the definitions for triggering rainfall conditions. These set of terms describe the rainfall conditions that correspond to a landslide event in different time scales. The event rainfall (Pe) corresponds to the daily rainfall on the date of the landslide, while the antecedent rainfall (Pa) corresponds to a duration of days prior to the landslide event. An illustration of the definition of these triggering rainfall condition terms is presented in Figure 2.1.

The antecedent rainfall depicted in Figure 2.1 represents the mean precipitation of a duration of 30-days prior to the landslide event. This value describes the average amount of precipitation coming from the atmosphere. In order to calculate the amount of this rainfall that infiltrates through the soil and interacts with the groundwater table, the effective antecedent recharge (qa) for the event is also taken into consideration. The effective antecedent recharge describes the amount of precipitation infiltrating through the soil, after the antecedent rainfall is subject to hydrological processes of evapotranspiration, runoff and interception. The calculation of effective antecedent recharge is shown in Equation (2.1)

$$qa = C_r \cdot Pa_i \tag{2.1}$$

where C_r is the empirical recharge parameter dependent on the drainage capacity, climate characteristics and hydrological properties of the study area, Pa is the antecedent

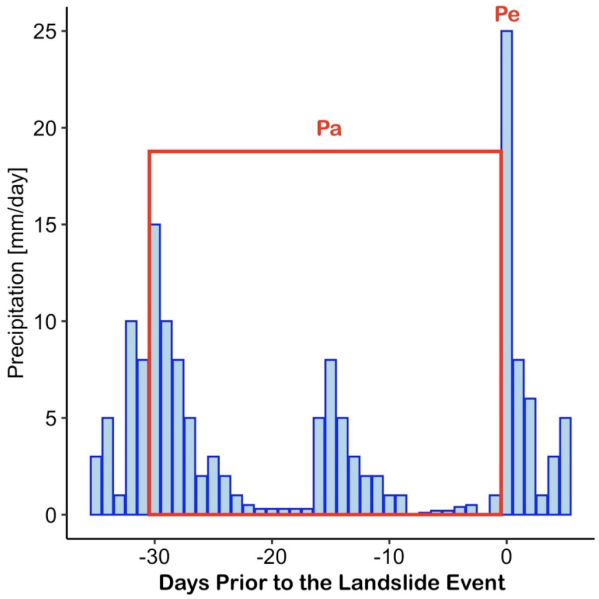

Figure 2.1: Definition of time scales for triggering rainfall conditions for the event rainfall (*Pe*) and the 30-day antecedent rainfall (*Pa*).

rainfall for the duration of days i prior to the landslide, and qa is the effective antecedent recharge.

2.1.2 Extreme and Mean Daily Rainfall Conditions

This section aims define daily rainfall used to identify extreme rainfall events and the mean rainfall conditions. It was necessary to establish terms for the prevalent and future precipitation patterns, frequencies and magnitudes in the study area. This is key to establishing common terminology between the hyrdological analysis of the present conditions and impact of future of climate change on rainfall conditions that could trigger landslides.

The mean rainfall conditions use the description of monthly rainfall to describe the average daily rainfall of a month taken into consideration. While, the mean seasonal rainfall considers the average daily rainfall considered. This research project focuses on the summer season analysis of landslide events, defined as the months of May to August. The extreme daily rainfall describes the monthly maximum daily rainfall detected. This term takes the block maxima perspective for defined extreme rainfall

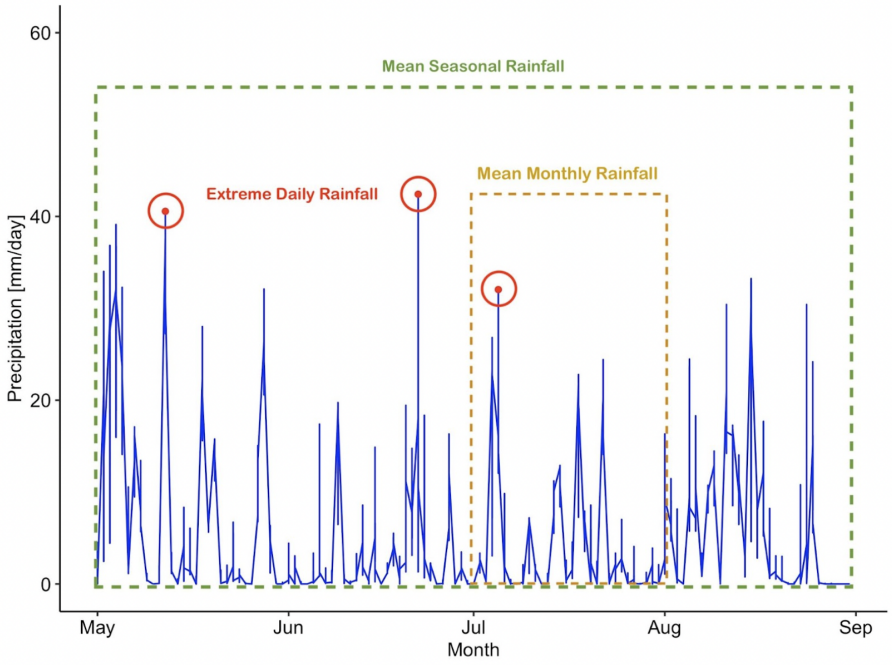

Figure 2.2: Definition of time scales for rainfall considered under climate scenarios. Extreme daily rainfall (red), mean monthly rainfall (yellow), and mean seasonal rainfall (green).

events [22]. Figure 2.2 provides an illustration of the time scales for the daily rainfall terms presented in this section.

2.2 Determination of Triggering Rainfall Conditions

The role of antecedent rainfall as a determining factor for landslide initiation is recognized through the extensive studies on deriving statistically-based thresholds, investigating water table field observations and in influencing slope stability of physically-based models [23–31]. Relevant literature in defining antecedent rainfall events in triggering shallow landslides are discussed in this section. Segoni *et al.* [32] observes that while antecedent rainfall is widely used in establishing rainfall-duration thresholds, there is an overwhelming variety of approaches taken by research groups in treating these events. Although this is the case, it was observed that researchers often do not directly use rainfall measurements in incorporating antecedent rainfall into their studies, but rather derive an antecedent rainfall index to incorporate degrees of saturation across the study area's terrain.

The processing of rainfall measurements to reconstruct an antecedent rainfall index is performed to account for a decrease in influence of rain events with respect to time due to the drainage processes across the terrain. A calibrated antecedent rainfall index was proposed by Crozier [23] and is presented in in Equation 1:

$$CARx_n = KP_1 + K_2P_2 + \ldots + K_nP_n \tag{2.2}$$

where CAR_x is the calibrated antecedent rainfall index for day x;P_n is the daily rainfall x days prior to x. The constant K is the decay constant and an empirical parameter dependent on the draining capacity and the hydrological characteristics of the area. In order to determine the K-value decay constant, studies conduct trials but a consensus arrives at K=0.9 with a limit to 30-day antecedent rainfall in study sites spread across Bangladesh, Korea, and Portugal [25, 26, 28].

The study of Kim *et al.* [26] assessed that an appropriate determination of a calibrated antecedent rainfall index to identify landslide-triggering events at a regional scale requires a detailed study on the hydrological processes, instead of insight from a data-driven analysis.

The calibrated antecedent rainfall index is used to define an effective antecedent rainfall-duration threshold to analyze patterns of rainfall-triggering rainfall conditions and determine thresholds for operational early warning systems. Although this is a widely used method, the results of Ma *et al.* [27] on a study area in Zhejiang, China, show that the false positive rates for K-values between 0.9 and 0.75 go from 63% to 51%. While this method is useful for operational purposes and early warning systems in ungauged basins, the false-positive rates and spatial variation of the hydrological processes across a catchment should be considered when being used to define an appropriate constant for identifying critical antecedent rainfall.

Another method in determining the duration to which antecedent rainfall can trigger

a shallow landslide is a comparison of cumulative antecedent rainfall and event rainfall using a 1:1 line to graphically assess the correlation between antecedent rainfall and event rainfall as triggering rainfall conditions, as illustrated in Figure 2.3. A study by Dahal & Hasegawa [33] on landslides in the Nepalese Himalayas utilizes this method to determine the role of cumulative antecedent rainfall versus event rainfall, based on an inventory of historical landslides. The population bias is measured across a 45-degree line on a bivariate plot to determine the influence of either event rainfall or antecedent rainfall. It was determined that while 55% of inventory landslide events considering 3-day antecedent rainfall were determined by the event rainfall, 30-day antecedent rainfall determined 98.4% of landslide events when compared to the event rainfall. Furthermore, this study examines the relationship between slope failure, and daily rainfall versus cumulative rainfall in the Nepalese Himalayas during the critical monsoon season. The results using the same method find that the 10-day cumulative rainfall at failure showed a higher correlation coefficient compared to 3,5, and 30-day periods.

The results depicted in Figure 2.3 demonstrate insight that can be derived through the method of population bias measurement versus a 1:1 diagonal line on a bivariate plot and an analysis correlation coefficient for different antecedent event periods.

Mathew *et al.* [29] utilized the same method of analysis in the Garhwal Himalaya, India, to assess combinations of rainfall parameters and their influence on triggering slope failures. Their analysis found that comparing daily rainfall values of the failure events to the 3-day cumulative rainfall and 30-day cumulative rainfall yield identical results. In this area, the distinction of antecedent rainfall in terms of influence on determining slope failure is not evident. The literature reviewed on studies utilizing the 1:1 bivariate plot method have shown how this simple approach to establishing a correlation between cumulative antecedent rainfall and event rainfall has been effective in analyzing the influence of antecedent rainfall, identification of major rainfall-triggers for shallow landslides and the effects of different durations in antecedent rainfall and event rainfall on landslide occurrence.

The methods of antecedent rainfall index and the 1:1 bivariate plot analysis are data-driven insights to fortify the definition of antecedent rainfall in an area, region or study site. Observations from field experiments and insight from physically-based models account for responses to geotechnical and hydrological processes and provide more definitive thresholds for durations critical antecedent rainfall.

Tu *et al.* [31] in a field experiment on an engineered loess slope, subjected the soil to artificial rainfall and measured the response of the slope with instruments to measure matric suction, volumetric water content, and pore pressure at different depths. Their findings revealed that matric suction decreases rapidly for 120 mm/day rainfall, with an influence depth reaching 3 meters. It was determined in this study that the 9-day

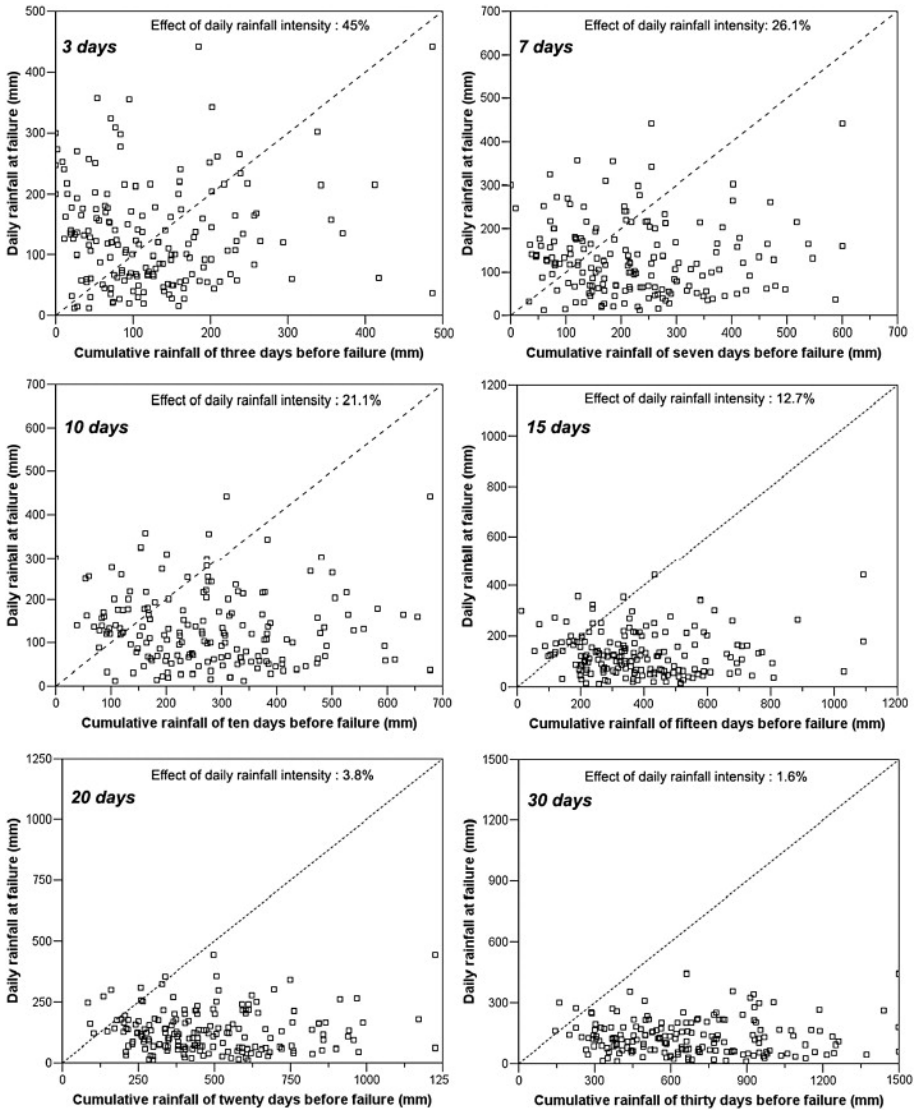

Figure 2.3: Comparison of the relationship between cumulative rainfall before failure and daily rainfall at failure over the Nepal Himalayas for different durations of consideration. The broken line (guide line) represents daily and cumulative rainfalls are the same at failure. Cited from Dahal & Hasegawa [33].

antecedent rainfall was critical to slope stability, where the matric suction at a 3-meter depth was almost zero. The analysis of results from this study suggests that it is possible for 9-day antecedent rainfall with 120 mm/day event rainfalls to have serious consequences on slope stability for loess-type engineered slopes. While this may not be directly applicable to all slopes, these results provide a reasonable starting point for further analysis with a data-driven approach.

Tang *et al.* [30] used a physically-based model using two-dimensional seepage analysis to analyze the effects of antecedent rainfall with data from the Three Gorges Reservoir Area, China, with a homogeneous slope model. The model results show significant variation depending on the permeability coefficient of the soil, thus deriving different conclusions for sandy and clayey soil type slopes. In particular, the recommendations look at minimum durations of consideration following heavy rainfall events, and maximum durations, where the influence of antecedent rainfall is minimal. It was concluded that the 15-day antecedent rainfall was the minimum to reflect a real factor of safety for slope stability for sandy slopes, while the influence beyond a 30-day antecedent rainfall duration is minimal. The results for clayey slopes suggest a minimum consideration of 20-day antecedent rainfall and a maximum of 40-day antecedent rainfall. While the model results show that the minimum factor of safety does not have a direct relationship with the maximum daily rainfall, the maximum accumulating rainfall over a 10-day period for sandy slopes and a 15-day period for clayey slopes can be related to a minimum factor of safety. The recommendations from this physically-based model expands the results from field observations to provide initial values in defining significant antecedent rainfall duration.

The analysis of literature in this section provides reasonable initial considerations of significant antecedent rainfall duration based on field experiment observations as well as physically-based model analysis of slope stability for different soil types. It was also established that two methods that can be used in assessing the agreement of the initial critical antecedent rainfall duration and the observed landslide occurrences from an inventory of historical events.

2.3 Shallow Landslide Susceptibility and Climate Change

This section analyzes studies and literature that attempts to estimate future landslide susceptibility with Global Climate Models (GCMs) or Regional Climate Models (RCMs), and looks at insight on means of dealing with the uncertainty and bias inherent to landslide-climate modeling chains.

Gariano & Guzzetti [3] presented a framework for landslide-climate modeling and recommended that scenarios investigating the impact of climate and environmental changes on landslide susceptibility is crucial to understanding the future of landslide risk, shown in Figure 1.2. A current gap in the landslide-climate modeling chains are found in the lack of performance of global climate models, and the uncertainty from climate change scenarios. It was determined in their study that regional-scale study results are strongly dependent on the selection of the driving models, the downscaling methods and the adopted reference scenarios. These factors reduce confidence in the landslide projections from studies, and a way forward can be found in the utilization of an ensemble of models to quantify the uncertainties of projections.

Alvioli *et al.* [34] investigates the relationship between downscaled climate projections and landslide occurrences for the years 2010-2049. The study used a model chain consisting of Weather Research and Forecasting (WRF) RCM simulation outputs with Rainfall Downscaling by a Filtered AutoRegressive Model (RainFARM) to provide input rainfall data, while using the Transient Rainfall Infiltration and Grid-Based Regional Slope-Stability Model v. 2.0 (TRIGRS) slope stability model to analyze the future landslide susceptibility. The resulting increased uncertainty between the model evaluation based on measured events and the distribution of events from the output of downscaled RCM. The large uncertainties in the landslide-climate modeling chain were found to make this approach less robust than establishing rainfall thresholds. The parametrization, resolution and processes of different climate models were established to be an important source of potential uncertainty in the conclusion by this study.

Peres & Cancelliere [8] combined the use of a stochastic rainfall generator, a simplified Richards vertical infiltration hydrological model, and an infinite slope model to estimate landslide probability through Monte Carlo simulations. This study investigated the impacts of climate change projections from an ensemble of three RCMs through the extraction of change factors to adjust duration and rainfall depth parameters in the stochastic rainfall generator. Their results find that the change factors in Representative concentration pathways (RCPs) 4.5 and 8.5 reflect significant seasonal variation, and the results indicate a variation between RCM results based driving GCM affects the projected frequency of rainfall events. The changes in standard deviation are found to be more significant than the mean precipitation.

The results of the study implementing this combined modeling framework indicate that the presence of a high spread of climate modeling uncertainty can be partially

addressed with the use of a wider ensemble of RCMs. This study demonstrates a simplified approach to utilizing projections from RCMs in establishing trends, and characteristics of climate change in reducing uncertainty along the landslide-climate modeling chain.

Scheidl *et al.* [12] investigated combined climate change and land use change scenarios through an integrated landslide-climate-landscape modeling chain. Although climate scenarios were considered in this study for the landscape simulations, three design rainfall events were considered in this study based on a 100-year recurrence. The recommendations identified incorporating possible influences derived from the change in frequency of extreme precipitation events under climate change in future studies.

The review of literature in this section looks at results and recommendations from studies using landslide-climate model chains. It was observed that the greatest source of uncertainty in the model chain is from the climate models and the resulting projections [3, 34]. It has been suggested that utilizing a wider ensemble of GCM-RCM combinations will allow for the quantification of uncertainty in determining impact of climate change on shallow landslide risk [8].

Scheidl *et al.* [12] indicated that another approach for long-term modeling is the simplification of representing triggering rainfall events through implementing design rainfalls with a return period. Careful consideration must be taken into account when specifying return period events in future cases, due to the changing distribution of events driven by the non-stationary nature of climate change. Finally, Peres & Cancelliere [8] present the idea of deriving change factors from global climate models instead of directly applying downscaled RCM results to shallow landslide models is an approach to reducing uncertainty in a complex modeling chain.

3 Case Study on Wanzhou County, China

A focus on the descriptive site details and contemporary landslide research is presented for the selected study area of Wanzhou County, China. Climate change impact research and assessments over China and specific to the Yangtze River Basin are also discussed. The discussion of this chapter gives context to the trends and factors that could affect the study site from a wider climate outlook.

3.1 General Site Description

Wanzhou County, China was selected as a study site of this research project and accomplish the objectives presented in Section 1.4. The study site is bounded by the coordinates N 30°24′25′′, E 107°52′22′′to N 31°14′58′′, E 108°53′25′′, with an area of 3 457 km^2. The district is located within Three-Gorges Reservoir along the Yangtze River, and upstream of the Three Gorges Dam, shown in Figure 1.1. This region of China is categorized as subtropical humid monsoon zone with a mean annual precipitation of 1191.3 mm. The precipitation patterns in this area are characterized by 90% of the annual rainfall occurring between May and September. Summer rainfall can be characterized by short intense rainstorms with daily rainfall values exceeding 100 mm/day [19].

The Lithology in the Wanzhou district comprises of the a Jurassic (J) system and a Triassic (T) system, illustrated in Figure 1.1. The Jurassic system mainly consists of mudstone, sandstone, siltstone and shale. The Triassic system is primarily composed of limestone, clay stone, sandstone, siltstone, and coal.

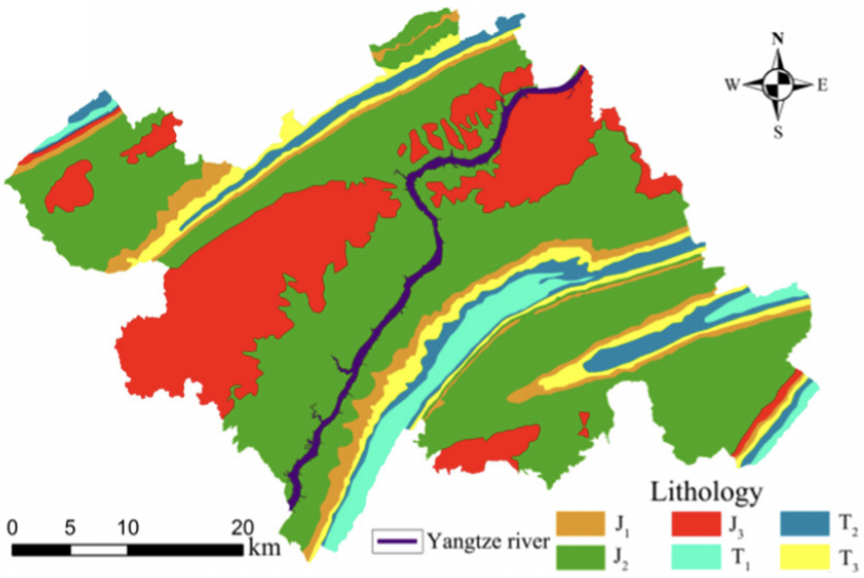

Figure 3.1: Lithological units in Wanzhou district: J_1 (quartz sandstone, shale, limestone), J_2 (sandy mudstone, quartz sandstone, shale, feldspatite, siltstone), J_3 (quartz sandstone, aubergine mudstone, lithic sandstone, shale), T_1 (dolomitic limestone, flaglike limestone), T_2 (argillaceous limestone, dysaerobic fauna, aubergine mudstone, calcareous shale), and T_3 (lithic Sandstone, arenaceous shale, coal seam). Cited from Huang *et al.* [20].

3.2 Landslide Studies in Wanzhou County

Landslide occurrences in the Wanzhou County are of concern, with large and numerous events occurring over recent years. Such frequent occurrences have been a subject of interest for advances in research towards better landslide susceptibility mapping and disaster risk reduction. The heavy rainfall in the study area was attributed to be a driver of the significant and frequent landslides that have occurred. [20, 21, 35].

In 2016, the Wanzhou District was selected to pilot community-based DRR program to reduce landslide risk instigated by survey findings indicating the occurrence 921 landslides surveyed in the region. It was determined that many of these landslides occurred after the filling and drawdown operations of the Three Gorges Dam [18]. The Tangjiao, Sanzhouxi, and Jinzhuquji landslides, shown in Figure 3.2, are examples of landslides of concern that were monitored and studied in the implementation of this program.

In another study, an inventory of 639 rock and soil landslides occurring between 1970 to 2013 was utilized to explore machine learning techniques for susceptibility mapping [20]. The analysis of this inventory finds that nearly half of the 639 landslides occurred

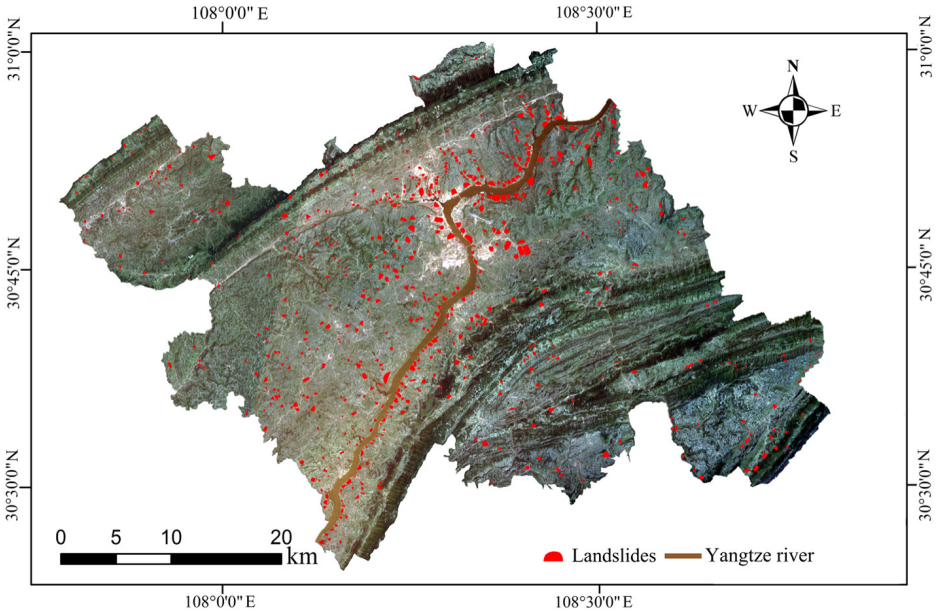

Figure 3.2: Locations of the 639 distinct landslides inventoried within the Wanzhou district from 1970 to 2013 Cited from Huang *et al.* [20].

between 1993 to 2013, while the rest were reactivated old landslide sites. The triggering factors for soil landslides in this inventory were determined to have been triggered by heavy rainfall and influence from fluctuations in the reservoir level. Anthropogenic activities that involve slope modification were attributed as an increasingly influential triggering factor.

The susceptibility map derived from the implementation self-organizing-map network and extreme learning machine method in the study of Huang *et al.* [20], is presented in Figure 3.2. Their analysis of the landslide triggering mechanisms based on the inventory resulted in the development of the data-driven model around geophysical characteristics, land cover, and distance to the Yangtze River. Naturally, the critical areas within the district are present in proximity to the river. The final result of this study was a susceptibility map for Wanzhou County developed with self-organizing -map network and extreme learning machine.

The implementation of data-driven approaches to perform landslide susceptibility mapping in Wanzhou were further developed in studies by Song *et al.* [35] and Xiao *et al.* [36] to implement a variety of statistical-based machine learning techniques. The test site of Song *et al.* [35] particularly focused on the river area, showing more detailed results than those in Figure 3.3 by incorporating annual rainfall as the most important factor in determining landslide susceptibility.

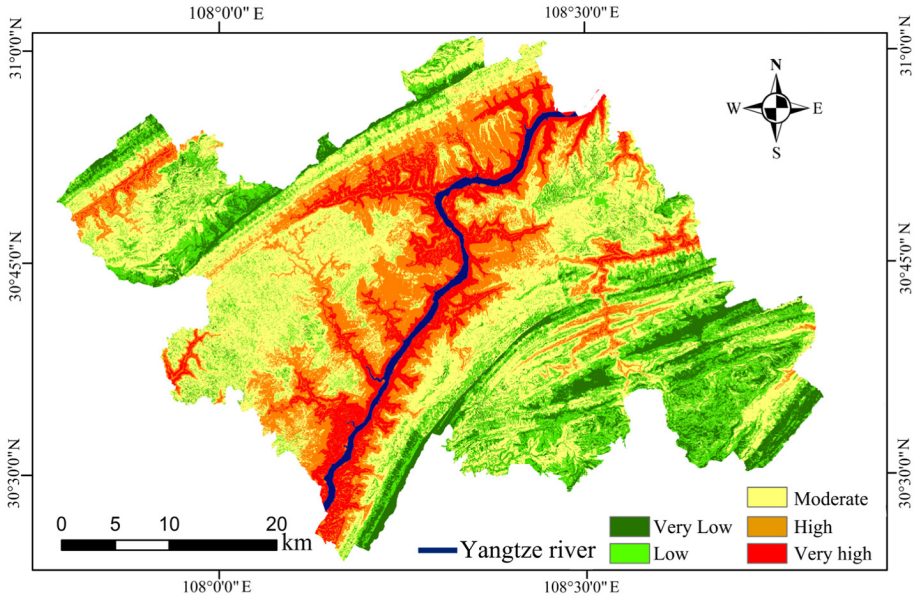

Figure 3.3: Susceptibility map for Wanzhou County developed in a study with self-organizing -map network and extreme learning machine. Cited from Huang *et al.* [20].

The abundance of rainfall and the intensity wherein 90% of the annual rainfall is realized between May to September has manifested in serious large landslide events. In 2013, the Sunja landslide occurred in Wanzhou County, displacing 1.5 million cubic meters. The mechanism of failure associated with this landslide was a rather complex displacement of soil that occurred over the period of 5 April to 31 August [21]. The location of the landslide within the district is shown in Figure 3.4.

In the risk assessment of the Sunja landslide conducted by Xiao *et al.* [21], it was determined that the 10-day duration of extreme rainfall was a critical triggering mechanism of this complex landslide event. The cause of failure for the Sunja landslide event was determined to be a combination of heavy rainfall and slope excavation activities. The outcome of this study was risk assessment derived from a combination of propagation and slope stability models for 10-day intensity scenarios corresponding to 20 to 100-year return period events.

Although there has been success in measured performance of these data-driven methods techniques to model landslide susceptibility, there has been no specific focus mapping the susceptibility based on detailed rainfall scenarios nor any interactions between landslide susceptibility and climate change. Even the risk assessment of the Sunja landslide was limited in the consideration of rainfall conditions due to future changes in climate.

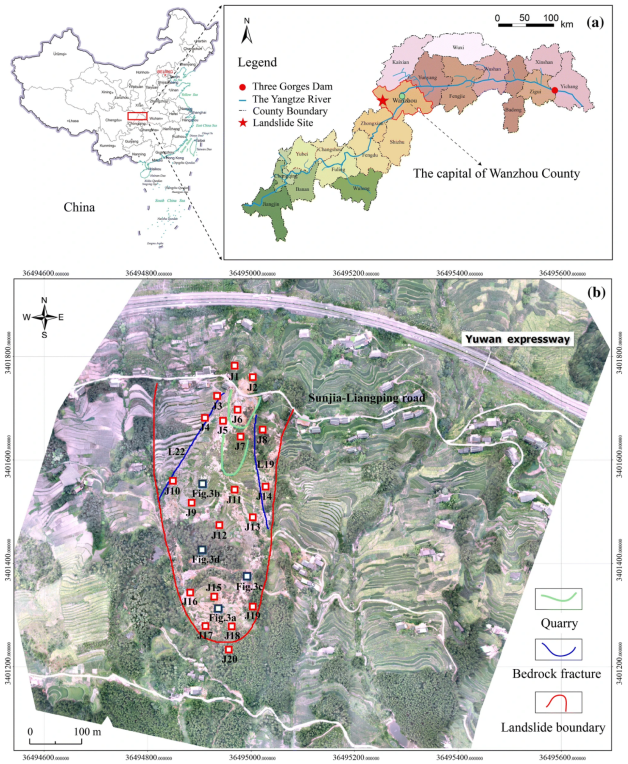

Figure 3.4: Location of the Sunjia landslide, Wanzhou County, Three Gorges Reservoir, China. Cited from Xiao *et al.* [21].

The location and details of the landslide inventories are discussed in detail though there has been no in-depth analysis of the reconstruction of the potential triggering rainfall events. The gap in research in incorporating possible rainfall triggering scenarios, detailed assessments of events reconstructed from the inventory and changes in landslide-triggering rainfall scenarios under climate change conditions was identified in this section.

It was determined that the researched questions proposed in Section 1.2, would be of scientific interest and add research value to the existing body of knowledge on landslide susceptibility mapping in Wanzhou County.

3.3 Shallow Landslides in Wanzhou

The shallow landslide inventory utilized in this study was created by the Wanzhou Institute of Geological Environment Monitoring and provided a spatial distribution of events within the Wanzhou county area from 1995-2005. Within this period, 186 shallow landslide events occurred across the study area.

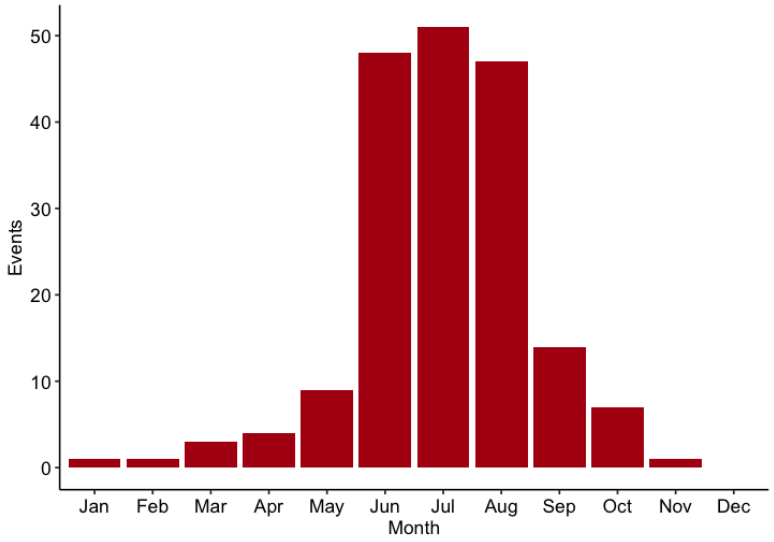

Figure 3.5: Histogram of monthly occurrences of shallow landslide events in the inventory from 1995 to 2005.

An analysis of the monthly shallow landslide inventory over the 10 years, shown in Figure 3.5, indicates that 146 of the recorded events occurred during the months of June to August, thus coinciding with the summer rainfall period. Given the frequency of event occurrence during the summer season, it was determined that this would be the critical period of analysis for rainfall scenarios to assess the susceptibility of slopes to shallow landslides under climate change conditions.

A single a rain gauge, located at 30.77 N, 108.40 E, from the Chinese Meteorological Agency (CMA) was made available for this study. The spatial distribution of the landslide occurrences captured by this inventory, and the location of the rain gauge are illustrated in Figure 4.2. The distribution of shallow landslides reveals areas of interest along the Yangtze River banks, and in the northwest corner of Wanzhou County.

It was determined that the scale of the study area was not compatible with the single point covered by this rain gauge. Therefore, the rain gauge data was solely used to

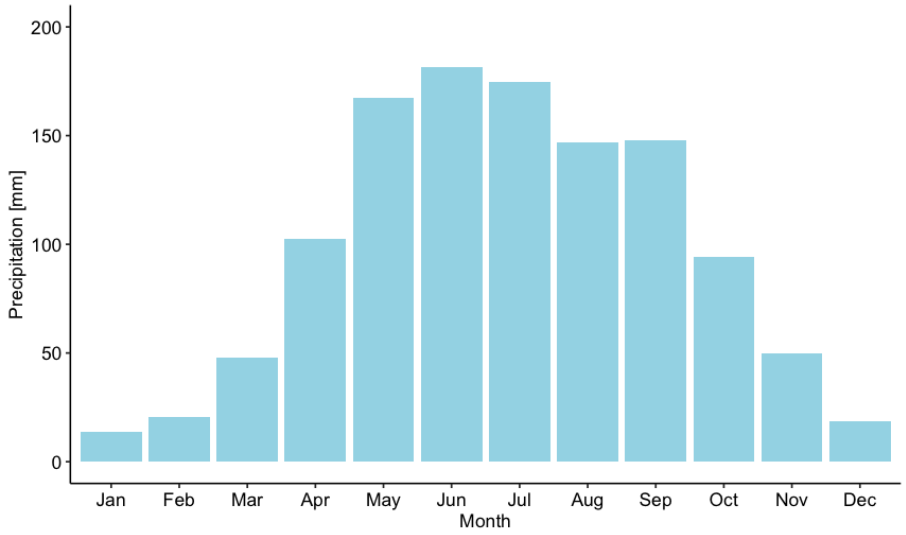

Figure 3.6: Monthly rainfall derived from the rain gauge observations within the study area from 1954 to 2015.

give an estimate to characterize rainfall over the study area in assessing the shallow landslide inventory. Figure 3.6 reveals that a trend in significant accumulated rainfall prior to the critical summer period occurs from May.

The significant accumulation of monthly rainfall occurring a month prior to the beginning of the season of increased shallow landslide occurrence in June suggests that recharge derived from the antecedent rainfall in May is potentially the triggering mechanism for some of these events.

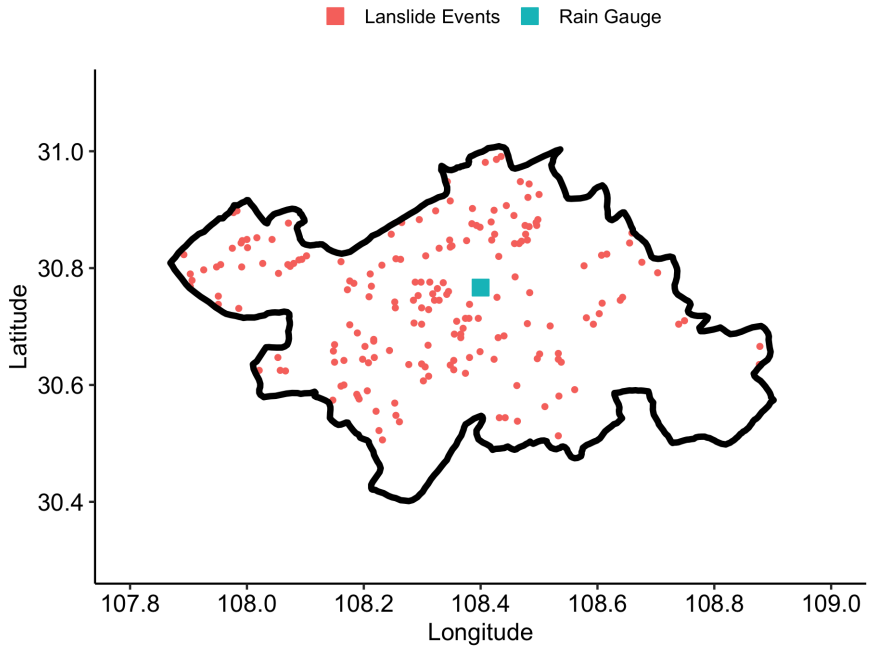

Figure 3.7: Shallow landslide occurrences from the Wanzhou Institute of Geological Environment Monitoring and the location of the Chinese Meteorological Agency rain gauge.

3.4 Climate Impact Assessments on the Upper Yangtze River Basin

A larger scale climatological perspective of China places the Wanzhou County area within the Yangtze River Basin (YRB), as shown by zone 6 in Figure 3.8, From the perspective of hydrological applications, Wanzhou is specifically in the Upper Yangtze River Basin (UYRB) and within the Sichuan Basin. Downstream from Wanzhou, is the Three Gorges Dam, therefore placing it with the Three Gorges River Basin. While there has been no specific research on climate change and landslide assessments in Wanzhou County, extensive research on the assessment of climate change models and their impact on extreme events and the hydrological cycle across China.

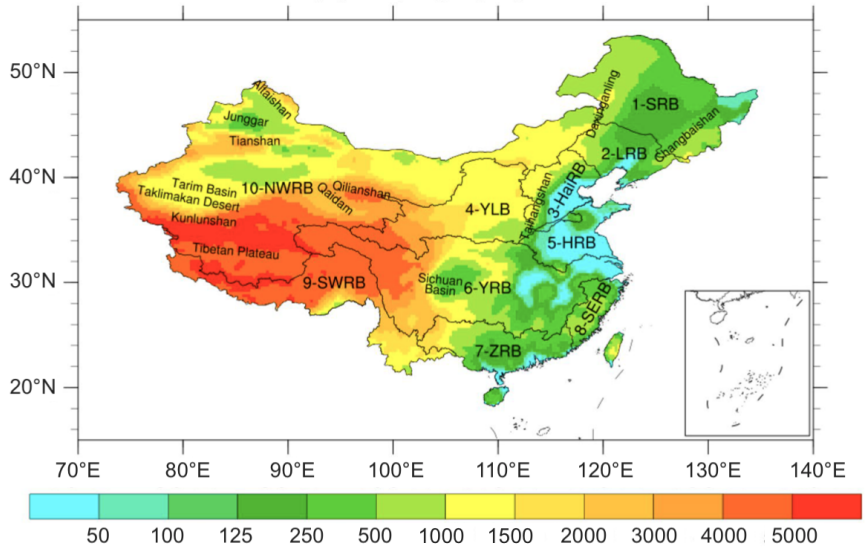

Figure 3.8: Major river basins across China with shaded topography (meters). Cited from Tong *et al.* [37].

The UYRB is a region of interest along the Yangtze River Basin that is of particular interest in climate change studies due to the frequency of floods and the sensitivity of this region to global warming . The influence of the East Asian summer monsoon and the South Asian summer monsoon on the Yangtze River Basin's precipitation patterns has presented unique and complex regional climate characteristics [38].

A study by Yang *et al.* [39] utilized 7 coarse resolution Global Climate Models (GCM) from CMIP5 to evaluate the present climate over China. The results of this climate model evaluation over the Yangtze River Basin indicated the limitation of GCMs results by wet biases present in January to May and dry biases present from July to October. The result of these biases is an early onset of monsoons, and a bias in the magnitude and timing of the East Asian summer monsoon, when compared to observations.

In order to obtain better results for the East Asian monsoon, Gao *et al.* [40] recommends that results from dynamically downscaled climate models from Regional Climate Models (RCM) would yield better results. The insights derived from the GCMs are limited and underestimate the higher magnitude daily precipitation events found in the upper quantiles of the observed frequency distributions.

A study on hydrological projections for 2020 to 2050 over the UYRB, covering the basins of the UYRB depicted in Figure 3.9 was conducted by Huang *et al.* [38]. This study utilized results of high-resolution RCM from International Centre for Theoretical Physics' Regional Climate Model (RegCM4). The RCM models implemented in this

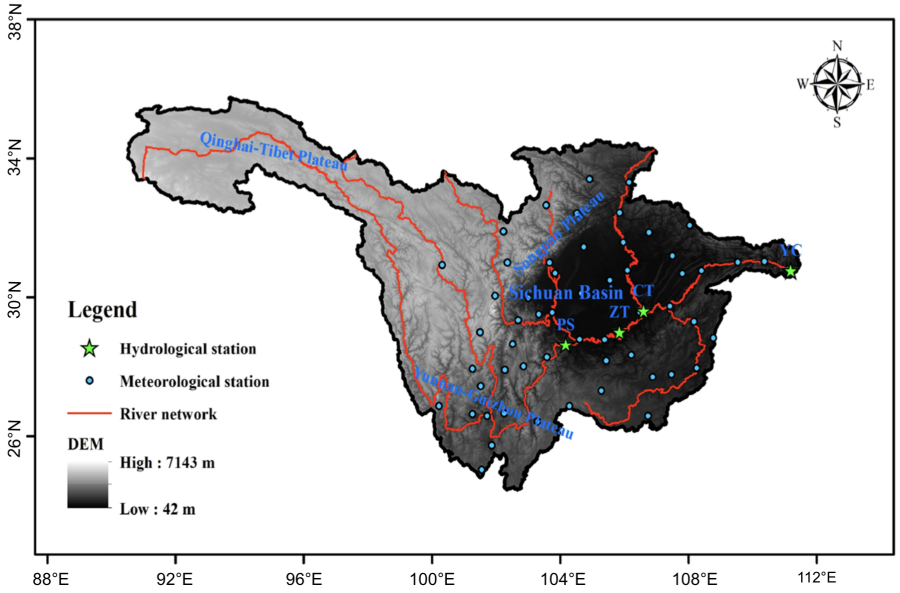

Figure 3.9: Hydrological basins within the Upper Yangtze River Basin. Cited from Huang *et al.* [38].

study were driven by the GCMs submitted to the Coupled Model Intercomparison Project Phase 5 (CMIP5).

The models were corrected for systematic model biases with the parametric quantile mapping method though a mixture of fitted frequency distributions. The findings for the near-future scenario project a warm-humid climate in the western UYRB with an expected decrease of precipitation at a rate of 19.05–19.25 mm/10 a. Furthermore, variation of precipitation on a multiyear average annual basis is projected to vary between -0.5 to 0.5 mm/day in the near-future precipitation projection in this study exhibits an insignificant downward trend, with significant variation between east and west of the UYRB.

The multiyear average precipitation in the Sichuan Basin significantly increased under the RCP 8.5 climate change scenario in the northwestern region while significantly decreasing in the southeastern areas. The separation of regions projecting increase and decrease across the Sichuan basin are illustrated in Figure 3.10.

The discussion of this section gives a brief overview of the insight derived from climate change studies including the UYRB. It is evident that there are limitations in studies that derive insight from coarse resolution climate models in capturing the critical East Asian monsoon. This is a critical limitation for climate studies over the UYRB and in effect, for climate studies about Wanzhou County, since this region's precipitation

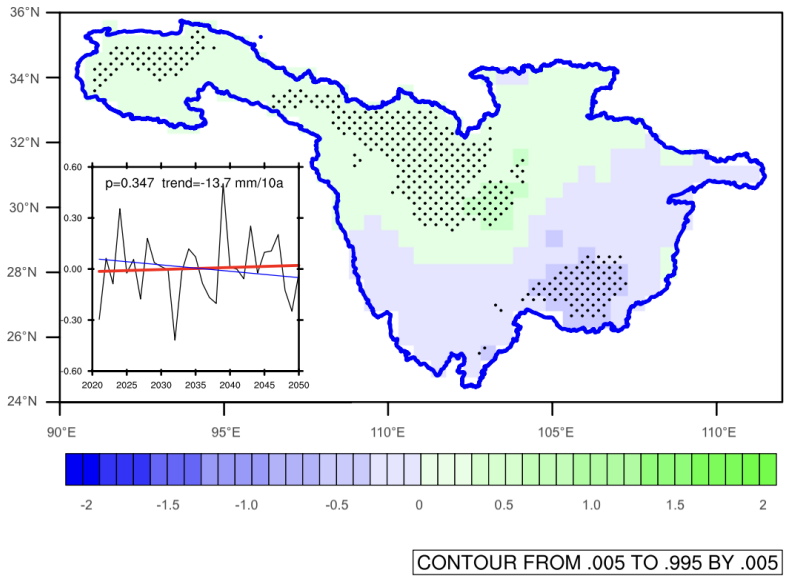

Figure 3.10: Near-future multi-year average changes in precipitation (mm/day) over the UYRB under the RCP8.5 scenarios compared to reference observations from 1971 to 2000. Cited from Huang *et al.* [38].

patterns are affected by the interaction of the East Asian and Indian summer monsoons. Thus, utilizing finer resolution RCMs should be a consideration in capturing that climate dynamics that are critical to assessing climate change.

The spatial distribution of change precipitation in the near-future, compared to the reference observations shown in Figure 3.10 places Wanzhou at the border of the region of significant increase and decrease. The study area is approximately place within the region of a mild decrease in precipitation in the near-future under the RCP 8.5 scenario.

A study by Gao *et al.* [41] assessed the performance of ERA-Interim reanalysis-driven RegCM4 simulations over the period of 1990-2010. Their results showed that this model was capable of reproducing present day climatology over China. The results of June to August were performed better than December to February, when compared to observations.

A comparison of biases of mean climatology and extremes find similarities in the reanalysis-driving model and the RCM outputs. This indicates that the performance of the RCM to produce mean seasonal climate and extreme daily rainfall is dependent on the performance of the driving models. The dependence and dynamics of the relationship between the boundary condition model and the implementation of the

dynamic downscaling through an RCM is depicted in the estimation of mean monthly precipitation over the YRB, shown in Figure 3.11.

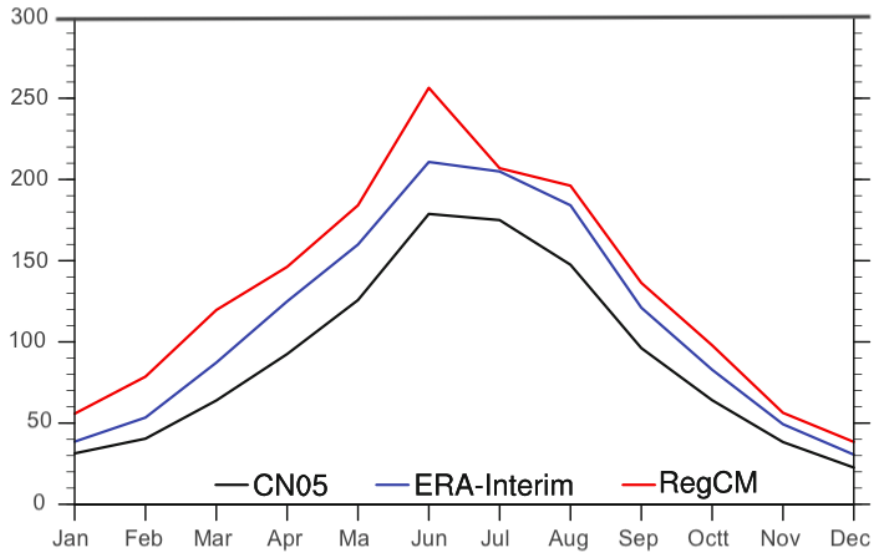

Figure 3.11: Mean monthly precipitation (mm) over the Yangtze River Basin from 1990 to 2010 derived from observations (CN05 in black), reanalysis model (ERA-Interim in blue) and the RCM model (RegCM in red). Cited from Gao *et al.* [41].

The performance of the RegCM in estimating seasonal precipitation over the YRB shows that it follows the trend of overestimation by the reanalysis model when compared to the CN05 observations. This overestimation is evident between May to July, while coming closer to the ERA-Interim results from July to August.

Additionally, the spatial correlation of precipitation of the model simulations, compared to the observations indicated an insignificant relationship. The limitation of RCM results based on the driving model is illustrated in these results. This underlines the importance of an ensemble approach highlighted by previous studies on assessing climate impact on shallow landslide susceptibility [3, 8]. The inclusion of results variation of driving models as input to RCM is an important consideration in this case study.

Recognizing the importance of selecting an driving model for dynamic downscaling with RCMs, the study on hydrological projections for the Yellow River and Yangtze River in China determined the Hadley Global Environment Model2-Earth System (HadGEM2-ES) gave adequate representation of present-day climate based on the validation in previous studies over China [42]. The findings from the projections for 2040-2060 for three RCP scenarios and utilizes the China Meteorological Forcing Dataset for

observations for 1980-2000. Though the study focuses on the Tibetan Plateau, in western region of China in Figure 3.8, the performance of this GCM-RCM combination was determined to adequately represent the dataset. This presents an alternative driving model to those utilized in Huang *et al.* [38], and suggests the options to expand effectiveness of an ensemble approach to assessing future climate impact.

The research on climate change models over China and in the YRB regions, have to this point highlighted the advantage of deriving insight from high resolution RCMs and the dependence and limitation of the results based on the boundary conditions from the driving GCM models.

An alternative model that has been used to assess climate impact across China is the Regional Climate Model (REMO), developed at the Max-Planck-Institute for Meteorology, and maintained by the Climate Service Center Germany (GERICS). Jingwei *et al.* [43] assess the performance of the REMO over China from 1989-2008 using the ERA-Interim reanalysis.

Their findings indicate that the REMO model is accurately able to reflect the distribution of total precipitation, and closely represents the temperature in the summer and total precipitation in the winter. Although findings showed a low spatial correlation of results for precipitation, while maintaining an annual mean bias of 300m across China. It was determined that the REMO performance is challenged by complex terrains across China.

A further study conducted by Xu *et al.* [44] utilized a similar combination of ERA-Interim and REMO simulation results from 1980 to 2012 to assess the impact of orography in the Hengduan Mountains on downstream the climate of East China. This study focuses on wind circulation but provides valuable insight on the performance of the REMO model on dynamics that affect precipitation.

The REMO simulations perform better in the summer when the westerly winds from southern China are less than the southwesterly prevailing winds in the winter. It was determined that the simulation overestimated the flow over the Hengduan Mountains and increased the transport of water vapor downstream. Therefore, these dynamics in circulation are responsible for excessive precipitation, a decrease in cloud cover and an overestimation of temperature. The downstream effects of the dynamics of the Hengduan Mountain in the REMO simulation affect the domain of East China and thus could influence the climate simulations and projections for Wanzhou County.

The presentation of the performance of various GCM and RCM combinations are discussed in this section to establish a perspective of performance and limitations in assembling an ensemble for this research on Wanzhou County. The ensemble approach to climate projections was implemented by Gu *et al.* [45] to analyze the changes in hydrological extremes for projections of 2020-2049 under the RCP 4.5 and 8.5 scenarios.

The study utilized an ensemble of 5 RCMs from the CMIP5 outputs, but were only driven by the HadGEM2-AO GCM.

The historical annual precipitation was best simulated by the HadGEM2-AO GCM, based the comparison of Gu *et al.* [46] on the performance of 26 CMIP5 GCMs. The resulting annual precipitation of 2020-2049 increases by 7.65%, compared to the period of 1980-2005 under the RCP 8.5 scenario.

The multi-model ensemble projected increases in extreme stream flow due to intense short-period precipitation events. The 5-member RCM ensemble projected slightly higher values, compared to the results of a similar 27-member GCM ensemble.

This study illustrates the implementation for an RCM ensemble for hydrological applications to assess climate change impacts in the YRB. The discussion of related climate literature over the study area suggests that the multi-model ensemble mean in this study could have been heavily influenced by the selection of one driving GCM. The consideration of more than one GCM in constructing a multi-model ensemble could thus avoid a potential overestimation in the ensemble mean projection.

4 Methodology

The methodology chapter presents the details of the conceptual framework applied to investigate landslide triggering rainfall conditions and derive climate change projections from regional climate models. The methodology established in this pilot case study area connects extreme statistics techniques from hydrology with atmospheric model correction methods to derive projections of future scenarios, and quantify the uncertainty in these projections.

4.1 Methodological Framework

The methodological framework presented in Figure 4.1 illustrates the three phases involved in this study to create shallow landslide-triggering rainfall scenarios.

The first phase of this study incorporated the landslide inventory available for 1995-2005 to reconstruct the antecedent rainfall and event rainfall based on the China Meteorological Forcing Dataset (CMFD) precipitation data set [47]. A present rainfall analysis was then carried out to explore the extreme daily rainfall using the CMFD data set. This analysis involved reconstruction of the seasonal antecedent rainfall conditions for the summer season (June-August) by accounting for average rainfall from May-July.

The projected rainfall analysis utilized model outputs from the Regional Climate Models (RCM) from the Coupled Model Intercomparison Project 5 (CMIP5) outputs [48]. The process to derive projected rainfall involved bias correction of RCM outputs for daily rainfall and extreme daily rainfall. Finally, climate change factors were computed to apply the present rainfall scenarios and produce quantified future triggering rainfall scenarios. The methodology was implemented across the Wanzhou County area, and procedure is discussed in this chapter.

4.2 Precipitation Data and Climate Model Outputs

4.2.1 Gridded Precipitation Observations

In order to understand the interaction between climate change and the magnitude of shallow landslide-triggering rainfall conditions, a reconstruction of rainfall using the dates of the landslides, and the coordinates from the inventory was conducted. Due to the spatial variation of the inventory events, the analysis of rainfall within

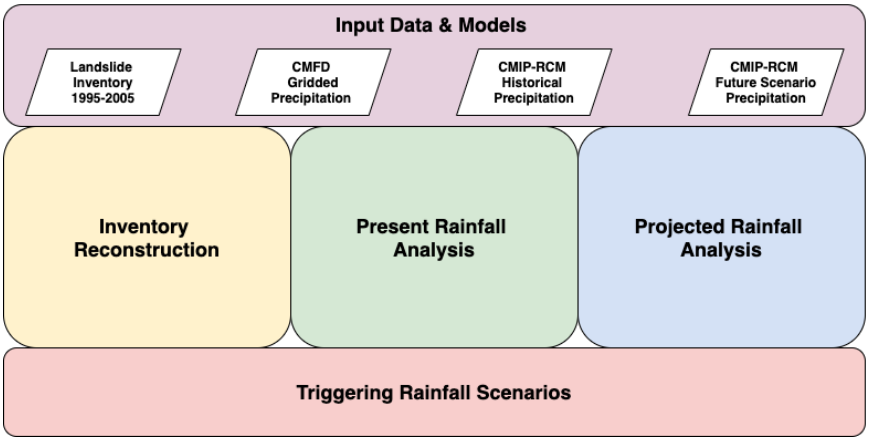

Figure 4.1: Conceptual methodological framework of this research project.

the study area utilised gridded precipitation data to capture the spatial characteristics and distribution of rainfall conditions. This section will discuss available rainfall data products, and the approach to modeling the frequency distribution across the study area.

A precipitation dataset representing the spatial variability of the study area was determined to be essential, given the regional scale of the area considered, and dispersed locations of the occurrences in the landslide inventory. The sole rain gauge available for this study would not be sufficient to reconstruct the rainfall conditions during and prior to each shallow landslide occurrence. Combinations of gridded precipitation datasets derived from satellite observations and interpolated rain gauge data were taken into consideration to analyse the rainfall-triggering characteristics within the study area.

Several satellite-derived precipitation estimate products were evaluated over the Yangtze River basin by Zhe *et al.* [49]. The conclusion of this evaluation was the ability of the TRMM Multi-satellite Precipitation Analysis (TMPA) research product (3B42V7) to perform adequately in estimating high rainfall intensity event rainfall. The more recent Global Precipitation Measurement (GPM) mission's Integrated Multi-satellite Retrievals of GPM data (GPM IMERG) over the Yangtze River Basin was determined to have better ability to estimate precipitation at a monthly time scale compared to the daily time scales [42].

Although the TMPA satellite product has considerable performance to assess the spatial characteristics of rainfall in the study area, the availability of TMPA estimates, beginning in the year 1998, was not compatible with the inventory of landslides that began in 1995 [50].

Two rain-gauge derived gridded precipitation datasets were assessed to obtain

spatially-distributed rainfall estimates within the study area. The first dataset is the daily gridded precipitation dataset at 0.25° × 0.25° resolution under the Asian Precipitation— Highly Resolved Observational Data Integration Towards the Evaluation of Water Resources (APHRODITE) project.

The APHRODITE gridded precipitation dataset was estimated through the interpolation of a dense network of rain gauge observations from 1961-2005 across Asia [51]. An updated APHRODITE-2 improves the ability of the dataset in analysing extreme precipitation events through the integration of multi-satellite merged precipitation products and the ERA-Interim reanalysis to ensure uniformity in the daily accumulation of precipitation across domains [52].

The assessment of Zhenyu & Tianjun [53] on the APHRODITE product when compared to rain gauge station data shows accurate seasonal precipitation characterization in mean states. However, it was concluded the APHRODITE dataset underestimated precipitation intensity and showed significant difference in spatial patterns of intensity trends, when compared to station data.

The second precipitation dataset, which was selected for study, was from the China Meteorological Forcing Dataset (CMFD) with a temporal resolution of 3 hours and a spatial resolution of 0.1°. This data set was derived from the integration of multi-satellite remote sensing products, reanalysis datasets and rain gauge observations from 1979 to 2018. The algorithm for the creation of the precipitation dataset utilised a monthly scale for interpolation, due to a smoother spatial distribution compared to results from sub-daily interpolation.

The sub-daily values were obtained through the integration of Chinese Meteorological Agency (CMA) station observations to gridded data from the Global Land Data Assimilation System (GLDAS) and Tropical Rainfall Measuring Mission (TRMM) at 0.1°. The interpolated sub-daily precipitation rate was then proportionally adjusted to the interpolated precipitation estimates at a monthly scale to obtain the spatial and temporal characteristics described above [47].

Daily precipitation at a spatial resolution of 0.1° was selected from the CMFD dataset for the rainfall analysis and reconstruction of inventory precipitation characteristics for this study.

The spatial variability of the shallow landslide inventory depicted in Figure 4.2, together with centers of the CMFD pixels highlight the importance of the gridded precipitation dataset in contrast to the sole rain gauge made available for this study area. The spatial coverage and resolution of the CMFD data set was determined to give better representation of precipitation conditions of the nearest corresponding inventoried landslide.

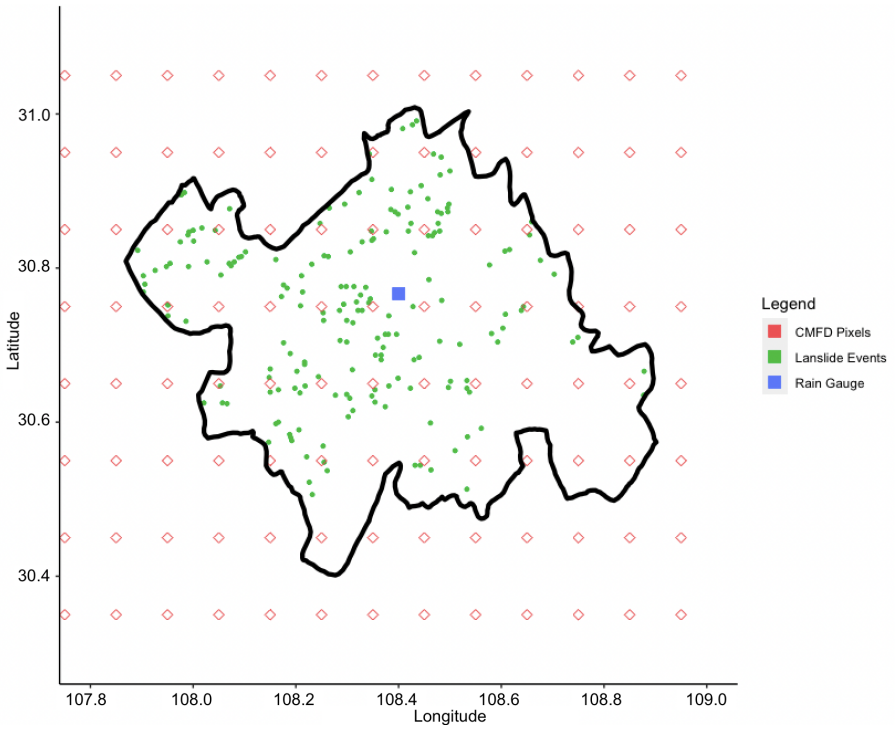

Figure 4.2: Spatial distribution of shallow landslides, center points of the CMFD gridded observations, and the location of the available rain gauge.

4.2.2 Multi-model Climate Projection Ensemble

In order to determine the change in magnitude and precipitation of landslide triggering, as proposed in the research questions, this study utilized projections from climate change models part of the outputs from Phase 5 Coupled Intercomparison Modeling Project (CMIP5) outputs [54], under the Coordinated Downscaling Experiment (CORDEX) Project.

These climate model outputs enabled the development of rainfall scenarios derived from the projected changes in precipitation. The climate model outputs used in this study consist of model outputs from Global Circulation Models (GCMs) that simulate emission scenarios to represent changing boundary conditions defined by Representative concentration pathways (RCPs). Different RCPs represent different cases of optimistic (RCP 2.5), moderate (RCP 4.5), and extreme (RCP 8.5) scenarios in emission releases with the objective of understanding possible outcomes based on insight from earth system dynamics modeled in GCMs [55].

A particular scenario of interest in this research project is the RCP 8.5 scenario. This

is the scenario that assumes high population growth, low income and slow rates of technological adaptation that will lead to long-term increases harmful emission in the absence of climate change policies [56]. This scenario the climate interaction with socioeconomic driving factors that could result conditions that will increase shallow landslide risk.

One limitation of large-scale simulations covering long time scales is the spatial resolution of information on the projections. While GCMs simulate climate dynamics to the spatial order of magnitude in the range of 100 kilometers, the projection information is likely incompatible with site-specific assessments that require higher spatial resolution to analyze changes in precipitation regime. The introduction of dynamic downscaling with Regional Climate Models (RCMs) aimed to provide higher resolution projection information through taking the climate output from the GCMs as boundary conditions to locally simulate the atmospheric physics at finer spatial resolutions between 10-20 km.

A combination of GCMs and RCMs were considered in this methodology to develop a multi-model ensemble projection. An overview of the climate studies conducted in Section 3.2, and the review of the state of the art in climate change assessments for shallow landslide susceptibility, discussed in Section 2.3, suggested the ensemble approach provides more robust and comprehensive climate change projections. Giorgi *et al.* [57] find that the utilization of a multi-model ensemble is a necessary approach to characterize uncertainties in climate projections. Thus, this research project considered an ensemble of 4 members considering 2 GCM and 2 RCM outputs to pilot the methodological framework, presented in Figure 4.1.

This research project utilizes a relatively small ensemble, where Giorgi & Coppola [58] recommend that a minimum of 4 to 5 RCM models are necessary to obtain robust precipitation projections. Further research on the optimal multi-model ensembles of GCM on the other hand suggests that 9 GCMs can adequately represent the climatology over China [52].

In assessing the importance of ensemble members, a study on exploring performance-based weighting for RCMs by Christensen *et al.* [59] found no compelling evidence for improved projections of this method when compared to the application of equal weights.

Advances in building robust projections through the reliable ensemble averaging (REA) method has demonstrated ability to reduce uncertainty and address systematic errors in RCMs to produce more reliable hydrological impact assessments [60].

In order to accomplish the research objectives in this project, a simpler equal weight approach was adopted, but the application of the REA method to improve the ensemble projections was taken into consideration for future research recommendations. This methodology was proposed to answer the research question, 4 ensemble members were

selected and given equal weight and the ensemble mean was analyzed to represent the projection.

The discussion on the individual performance of various GCMs and RCMs over China, in Section 3.2, established precedent to suggest an ensemble of climate models to be used in this study. It was determined that a combination of the HadGEM and MPI GCMs with the RegCM4 and REMO RCMs would be adequate to assess the impact of climate change on Wanzhou County. The identification of these models to pilot the methodological framework was based on the discussion on the results from bias correction, and adequacy of performance of these individual models, based on precious studies. The specifications of the selected ensemble members are shown in Table 4.1.

Table 4.1: Summary of ensemble specifications.

Ensemble Members	GCM Model	RCM Model
Member 1	HadGEM2-ES	REMO2015
Member 2	HadGEM2-ES	RegCM4
Member 3	MPI-ESM-LR	REMO2015
Member 4	MPI-ESM-MR	RegCM4

The selection of ensemble climate model members was based on the review of literature on climate studies over China and the YRB region in Section 3.2, and access to the outputs over the East Asian (EAS) CORDEX project. The next criteria was the time frequency and resolution of the model outputs. Only climate model results with spatial resolutions 0.22^o or approximately 25 km2 and daily time frequencies were considered for this research project.

In accordance with this criteria, RCM model outputs from the REMO2015 model [48], and the RegCM4 model [61] were selected from outputs under the EAS-CORDEX project domain. Both RCM models have been applied and studied in previous climate impact research projects discussed in Section 3.2.

The outputs of the experiments considered in this research project were those belonging to the historical configuration, and the RCP 8.5 scenario. Two driving models providing boundary conditions for the RCM models were considered. The first was the HadGEM2-ES GCM, developed by the United Kingdom's Met Office Hadley Centre [62]. The performance of the HadGEM Models over China were evaluated to adequately represent the climatology of the YRB, as discussed Section 3.2.

Two Max Planck Institute for Meteorology Earth system model (MPI-ESM) versions were utilized in this study. The first was the MPI-ESM-MR, driving the RegCM4 outputs, and the MPI-ESM-LR, driving the REMO2015 outputs. The differences in configuration in the MPI-ESM models are in their grid configuration. The MPI-ESM-LR runs on a bipolar grid with a 1.5° horizontal resolution, while the MPI-ESM-MR runs on a "eddy-

permitting" tripolar grid with 0.4° horizontal resolution. The simulation period for both models covered the years 1980-2100, with the HadGEM2-ES beginning in 1970 [63].

4.3 Reconstruction of Triggering Rainfall Conditions

Definition of the Antecedent Rainfall Duration

Antecedent rainfall is an important shallow landslide triggering mechanism, and a potential determinant for slope stability, as established in Section 2.2. Though studies do not usually directly use the average or accumulated rainfall, but rather utilize a Calibrated Antecedent Rainfall (CAR) Index to estimate the amount of rainfall that proceeds to recharge and contributes to the groundwater head.

While Segoni *et al.* [14] observed that there was a prevalence of variety in methodologies for incorporating antecedent rainfall conditions in shallow landslide susceptibility thresholds, Kim *et al.* [26] suggest that estimations of the recharge contributions through a thorough detailed model of the hydrological cycle is crucial for studying the contribution of shallow landslides at a regional scale. Thus, the determination of the landslide-triggering antecedent rainfall period is highly dependent on the in situ geological characteristics and the groundwater conditions.

The causal relationship between the observed season for a majority of landslides occurrences in Wanzhou with the significant accumulated monthly rainfall beginning in May suggest a significant influence of antecedent rainfall at monthly scale on shallow landslide triggering.

The study of Dahal & Hasegawa [33] suggested that in the Nepalese Himalayas, 30-day antecedent rainfall determined a majority of landslides observed, when compared to the event rainfall. Mathew *et al.* [29] find that in the Garwhwal Himalayas, 3-day cumulative rainfall and 30-day cumulative rainfall yield identical results in predicting failure. The similar results of the two studies on different areas of the Himalayan Mountain range indicate that 30-day antecedent rainfall is an important indicator of slope failure.

A seepage model study conducted by Tang *et al.* [30] on the Three Gorges Reservoir area in China suggested that the 15-day antecedent rainfall was the minimum duration of consideration to reflect a real factor of safety for slope stability for sandy slopes, while the influence beyond a 30-day antecedent rainfall duration is minimal. The same study also suggests minimum duration of 20-day antecedent rainfall and a maximum of 40-day antecedent rainfall was applicable for clayey slopes.

The study cases, and model insights presented in this section indicate that the antecedent rainfall 30 days prior to a shallow landslides can have considerable influence on its occurrence. Thus, the 30-day antecedent rainfall condition was selected as a significant period by which the recharge prior to landslide would be estimated.

Extraction Algorithm

An algorithm to match the precipitation information from CMFD dataset based on the recorded date and the spatial coordinates in the inventory. First the precipitation time series was extracted from the CMFD raster datasets using the landslide coordinates. Using the extracted time series, the event rainfall (*Pe*) was then identified as by the daily precipitation for the CMFD pixel. The average 30-day antecedent rainfall (*Pa*) was then extracted from the same pixel's time series of daily rainfall. Figure 4.3 illustrates the data extracted from this algorithm implemented in R.

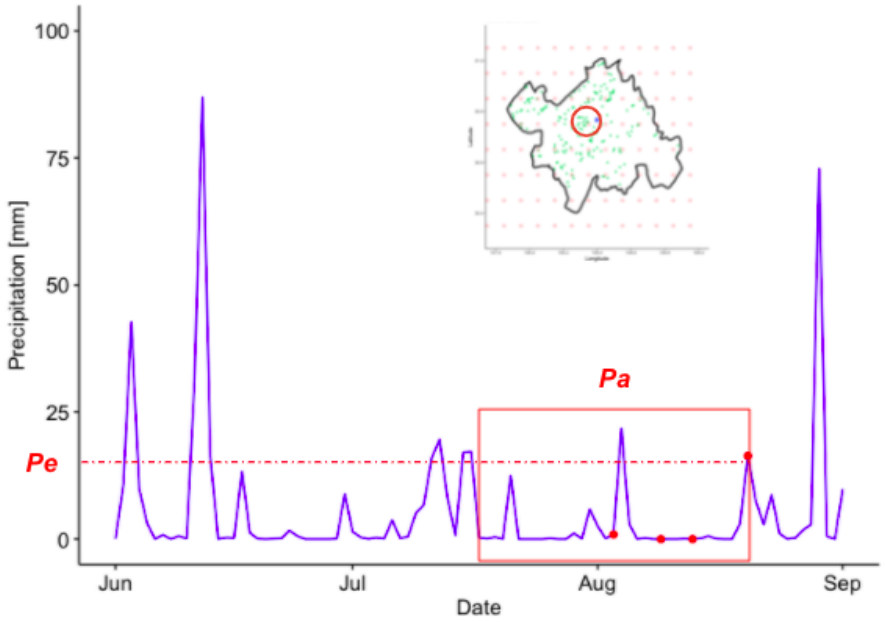

Figure 4.3: Schematic of the extraction of event rainfall (Pe) and the 30-day for antecedent rainfall (Pa) corresponding to landslide occurrences (red points) for one CMFD pixel time series within the study area (encircled in red in the insert map).

Effective Antecedent Recharge Estimation

Monthly recharge factors were then made available for the Wanzhou County area, through an EasyBal Hydrological Model [64] analysis for the period of 1995-2005 [65]. The EasyBal model incorporated precipitation, evapotranspiration, and temperature time series and resulted in an estimated monthly recharge fraction that can be applied to the average 30-day antecedent rainfall.

4.4 Extreme Daily Rainfall Analysis

The procedure for estimating the parameters of the Gumbel distributions was applied after extracting a time series of daily precipitation from each CMFD pixel within the study area. The goodness-of-fit based on the AD tests, KS test, and CVM criterion was then assessed within a 95% confidence interval.

Monthly Block Maxima

The application of extreme value statistics (EVS) in this study area was implemented to determine the frequency distribution of extreme rainfall-triggering event rainfall. This study utilized the Block Maxima approach to derive the probability distribution functions of extreme daily rainfall from the daily precipitation measurements in CMFD dataset. This approach equally divides the daily precipitation series into prescribed time periods, and from these blocks extracts the maximum values [22].

$$Mn = max\{P1, ..., Pn\} \tag{4.1}$$

where a sequence of n daily precipitation P variables were taken into consideration. The maximum values Mn obtained from the blocks of the equation above are then utilised to obtain a probability distribution function. Although annual maxima is typically considered for hydrological applications, studies demonstrate that monthly maxima can more precisely derive annual return levels [66, 67].

Gumbel Distribution Functions

The probability distribution function selected to obtain the annual return levels from the monthly maxima was the Gumbel distribution. An assessment of rainfall-induced complex landslides by Xiao *et al.* [21] adopted the Gumbel distribution to model the frequency distribution of extreme daily rainfall at 10-day intervals derived from 50-year rainfall records within Wanzhou County. The Gumbel distribution probability density function (PDF) $f(x)$, and cumulative density function (CFD) $F(x)$ are given in the following equations:

$$f(x) = (\frac{1}{\alpha})exp[-(\frac{x-\beta}{\alpha}) - exp(-(-(\frac{x-\beta}{\alpha}))] \tag{4.2}$$

$$F(x) = exp[-exp(-(\frac{x-\beta}{\alpha}))] \tag{4.3}$$

where α is the scale parameter and β is the location parameter . The relationship between the mean, μ, location and scale parameter is given:

$$\mu = \beta + 0.5772\alpha \tag{4.4}$$

The extreme rainfall rates RT in mm/day given the recurrence period of T years were determined using the equation:

$$R_T = \mu - \alpha[ln(ln(\frac{T}{T-1}))] \tag{4.5}$$

Gumbel Parameter Estimation

The parameters for the Gumbel distributions and were calculated by maximum likelihood estimation (MLE) where distribution parameters θ are by default estimated by maximizing the likelihood function give by:

$$L(\theta) = \prod_{i=1}^{n} f(x_i|\theta) \tag{4.6}$$

with x_i the n observations of variable x and $f(x_i|\theta)$ the density function of the parametric. The algorithm implementing the estimation methods utilised the fitdistrplus R package [68].

Goodness-of-Fit Tests

The goodness-of-fit of the estimated Gumbel distributions through the Anderson-Darling (AD) test, the Kolmogoro-Smirnov (KS) test, and the Cramer-von-Mises (CVM) criterion, evaluated at a confidence level of 95%.

Kolmogorov-Smirnov Test

The KS test statistic is the maximum vertical difference between CDF of the modeled and empirical distributions. This comparison of the empirical CDF ($Sn(x)$) and modeled CDF ($FX(x)$) with KS test statistic is performed on each X_n in a sample size of of n values, ordered in an increasing manner. The procedure for performing a KS test for an confidence interval of 95% is shown in the following Equations:

$$Sn(x) = 0;\ if\ X < X_1$$

$$= 1;\ if\ X > X_n$$

$$= k/n;\ if\ X_k < X < X_{k+1} \tag{4.7}$$

$$D_n = max|F_X(x) - S_n(x)| \tag{4.8}$$

$$P(D_n < D_n^{\alpha}) = 1 - \alpha \tag{4.9}$$

where D_n is the KS statistic, D_n^{α} is the critical value, is the significance level = 0.95, and k is the rank order of the value in the sample. Although commonly used, it has been observed that the KS test is weaker in power when compared to other goodness-of-fit tests [69].

Anderson-Darling Test

The AD test puts more weight on the performance on the tails of the cumulative distribution function, and is dependent on the distribution function taken into consideration as given as:

$$A^2 = -\sum_{i=1}^{n}(2i-1)ln[F_x(X_i)] + ln[1 - F_x(X_{n+1-i})]/n - n \tag{4.10}$$

where $x_i < ... < x_n$. A modified AD statistic for the two parameter Gumbel distribution is given by Equation 7.

$$A_n^2 = A^2(1 + \frac{0.2}{\sqrt{n}}) \tag{4.11}$$

The AD test was implemented through the 'goftest' R package, following the scheme originally proposed by Marsaglia & Marsaglia [70]. The AD test is also observed to perform slightly better than the CVM test [69].

Cramer-von-Mises Criterion

The CVM statistic measures the man squared difference between the empirical CDF and a fitted CDF. The statistic is given by:

$$W^2 = \frac{1}{12n} + \sum_{i=1}^{n}(F_i - \frac{2i-1}{2n})^2 \tag{4.12}$$

The CVM test together with the AD test are estimated in practice to measure the goodness-of-fit with a weighted emphasis on the tails of the distribution Laio [69]. The CVM tests were implemented by the 'goftest' R package.

4.5 Climate Change Analysis

This section presents the methodology developed to perform bias correction on the climate change models, assess the correction's performance through cross-validation, and derive a climate change factor based on projections for extreme daily rainfall and mean seasonal rainfall independently. Two climate change factors are derived from the bias-corrected data to represent the climate signal from the projections applicable to extreme, and seasonal rainfall.

The climate change analysis aimed to produce multi-model ensemble projections under RCP 8.5 conditions for mean seasonal rainfall and extreme daily rainfall. The scenarios are defined by the future periods in the Mid 21st Century from 2021-2060 and Late 21st Century from 2061 2100. The mean ensemble projections were reported as Climate Change Factors (CCF) relative to the reference period of 1979 to 2018.

4.5.1 Bias Correction Methodology

This section details the procedure implemented to separate the climate model outputs before bias-correction for extreme daily rainfall, to represent triggering event rainfall, and mean seasonal rainfall, that will represent antecedent rainfall.

The different bias corrections through empirical and parametric quantile delta mapping transfer functions were implemented. This resulted in a climate change factor applied to obtain the mean ensemble projections that represented extreme daily rainfall and mean seasonal rainfall. An overview of the framework for the bias correction methodology is presented in Figure 4.4.

The bias correction proposed utilized was the Quantile Delta Mapping (QDM) method. Two separate QDM procedures were shown in Figure 4.4 to correct the outputs and extract the climate signals for extreme events and antecedent events as independent variables.

The bias correction framework enabled the correction of systematic errors in the climate model outputs. The results yielded bias-corrected results for the Mid-21st Century and Late 21st Century scenarios, corrected against the reference period of 1979 to 2018.

The dataset of the reference period consisted of simulations from the historical model results between 1980 to 2005, and the RCP 8.5 projections from 2006 to 2018. The definitions of the climate change scenarios are summarized in Table 4.2.

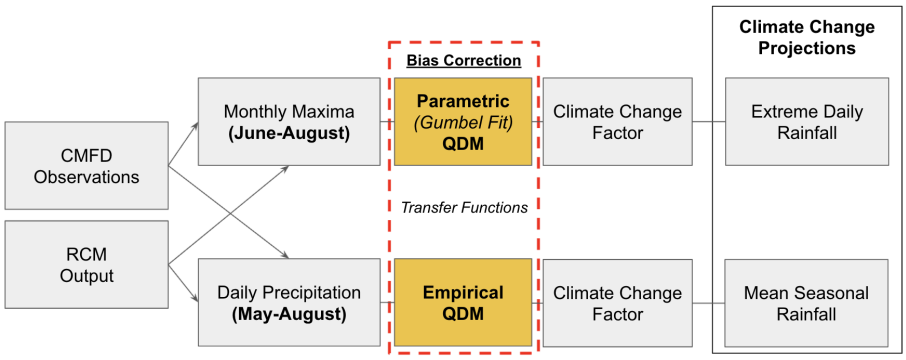

Figure 4.4: Flowchart of data required and bias correction methods and workflows to derive climate change projections for extreme daily rainfall and antecedent rainfall.

Table 4.2: Definitions of climate change scenarios.

Scenario	Period (Years)	RCM Experiment Outputs
Reference	1979-2018	Historical + RCP 8.5
Mid 21st Century	2021-2060	RCP 8.5
Late 21st Century	2061-2100	RCM 8.5

The reference period consisted of simulations from the historical model results between 1980-2005, and the RCP 8.5 projections from 2006 to 2018. The underlying assumption in the decision to combine the projection and historical model results to establish a combined reference period dataset was that the RCP 8.5 scenario is representative of the conditions under which the CMFD observations were recorded.

This may not necessarily be the case, but the essence of this methodological framework is to capture the trend in the bias-corrected precipitation in between time periods from the reference to future climate scenarios. Thus, supplementing the historical simulation results with future projection results to establish a reference distribution for bias correction will account for potential systematic bias and uncertainty in early periods of the RCP 8.5 projections.

4.5.2 Quantile Delta Mapping

Bias correction is performed on climate modes to address the systematic distributional biases in precipitation outputs. The assessment of present day climate by Gao *et al.* [40] indicated that high resolution RCM simulations critically outperform GCM results in reproducing the climate over China, with a specific advantage in assessing the development of the East Asian monsoon.

Research on the necessity and advancements of different bias correction methods on impact assessments and climate change projections for the YRB and over the entire China are widely studied in contemporary literature [37–39, 71].

A common approach to perform this task is through Quantile Mapping (QM). This method for bias correction utilizes a transfer function derived from precipitation observations to correct the frequency distribution in the climate model's historical outputs. The transfer function can be derived empirical from the CDF of the observations or with parameters of a fitted a frequency distribution model. The bias correction of a variable through QM is given by the Equation:

$$\hat{x} = F_{o,c}^{-1}[F_{m,p}(x_{m,p})] \tag{4.13}$$

where x_{bc} is the bias corrected precipitation, $F_{o,c}^{-1}$ is the inverse CDF derived from the observations, $F_{m,p}$ is the CDF derived from the model projections, and $X_{m,p}$ is the projected precipitation to be corrected.

The limitation of the QM method is that the future model projections are corrected using the information derived from the historical period. Trends and information about the future model outputs are not considered and lost in the bias correction procedure.

In order to address this limitation Cannon *et al.* [72] proposed the use of a Quantile Delta Mapping (QDM) bias correction method to perform bias correction while preserving the changes in quantiles in the projected climate outputs. Tong *et al.* [37] described the methodology for QDM that was performed on RegCM4 model projections over China. The procedure for QDM follows the process of first detrending the simulated model projection through QM during a calibration period, given by Equation (4.13).

The relative changes in quantiles between the calibration period and the projected period of interest was then derived from the ratio between the distribution of precipitation. This ratio of change is derived from the Equation below:

$$\Delta(t) = \frac{x_{(m,p)}}{F_{m,c}^{-1}[F_{m,p}^{(t)}(x_{m,p}(t)]} \tag{4.14}$$

where $\Delta(t)$ is the factor of relevant change in precipitation for the period of interest t, $F_{m,c}^{-1}(t)$ is the inverse CDF derived from the model projections over the reference period, $F_{m,p}^{(t)}$ is the CDF derived from the model projections over the period of interest t, and $(x_{m,p}(t)$ is the precipitation model projections over the period of interest t.

The bias corrected precipitation is derived from the product between the factor of relative change and the detrended variable $\hat{x}$ as shown in the Equation:

$$x_{bc}(t) = \hat{x}\Delta(t) \tag{4.15}$$

where $x_{bc}(t)$ is the bias corrected precipitation time series for the period of interest t.

The objective of performing bias correction on RCM outputs was to correct the substantial systematic error, partly inherited from the GCM on the boundary conditions, and obtain results to assess trends and climate signals. Specific applications of climate change studies require insight and analysis from specific climate signals. Bias correction was performed separately for daily precipitation and extreme daily rainfall.

Empirical Quantile Delta Mapping for Daily Rainfall

Assessments of trends in the mean climatology will require climate signals covering seasonal and annual measurements. If not corrected separately, the rectification of systematic error that might distort the distribution of daily, monthly or annual projections. The QDM bias correction method presented in this section adequately enhanced the insight from the climate models to attain more certainty in the projections.

Previous studies have established that a non-parametric transfer function to perform quantile mapping bias correction has the advantage of not requiring an assumption of the distribution of the observed and modeled rainfall [37]. This was deemed appropriate to obtain results of the influence of climate change on antecedent rainfall found in the climate projection models.

The application of a transfer function derived from the empirical cumulative distribution function would directly account for the distribution of daily rainfall without adding uncertainty derived from a fitted distribution function.

The bias-corrected seasonal precipitation would result in a more realistic representation of the distribution observed, and retain the relative change in precipitation from the model, without distorting the output frequency distributions. Therefore, the bias correction of daily precipitation was conducted for the months of May to August to assess the summer season projections and meet the research project objectives.

Parametric Quantile Delta Mapping for Extreme Daily Rainfall

The bias-correction of results to capture precipitation extremes required the application of QDM to involve considerations of the limitation of the climate models to simulate the frequency and magnitude of such events on regional and local scales [73]. The necessity to conduct a bias correction on the simulated climate date using annual maxima instead of the conventional daily precipitation was established in a study by Kim *et al.* [74]. Their study found that the conventional bias-correction method using daily data was limited in ability to capture extreme rainfall quantiles, and required a bias correction for the application of extreme rainfall frequency analysis.

Though RCMs were found to over predict the probability of extreme daily precipitation, it was found that results could be corrected to adequately represent the upper-tail distributions in observations Durman *et al.* [75]. While this provided promising reassur-

ance of the present conditions, it was also found that RCM models have been found to be unable to represent the relationship between extreme rainfall and temperature [76].

Research indicates that the distribution and magnitude of extreme rainfall in the future projections would be subject to more uncertainty, and be less likely to represent reality. Thus, given the limitations of GCM and RCM models to capture extreme precipitation events, it cannot be assumed that an empirically-derived extreme precipitation distribution will adequately represent reality.

The alternative to assess the trend in extreme daily rainfall was to capture the trend in extreme precipitation through a parametric QDM approach. Kim *et al.* [77] fitted General Extreme Value (GEV) distribution models to the annual maxima datasets to perform the QDM. The selection of GEV distribution models was based on the 2019 flood estimation recommendations of the South Korean Ministry of Environment.

The demonstration of the application of parametric QDM to bias correct extreme daily rainfall inspired the direction for bias correcting results of the ensemble members in this research project.

The approach to establishing the transfer function for bias correction for extreme daily rainfall is outlined in the methodology for the extreme rainfall analysis in the present, shown in Section 4.4. The Gumbel fit was selected for this area due to the suggested performance in capturing extreme events by Xiao *et al.* [21]. Similarly, the selection of the GEV distribution by Kim *et al.* [26] was based on the suggestion flood estimation guidelines for South Korea, issued by the Ministry of Environment in 2019.

The extraction of monthly maxima in the simulation outputs for June to August for the scenarios defined by the years listed in Table 4.2 was considered in the application of the QDM bias correction. The magnitude of extreme daily rainfall were then determined for different return periods with Equation (4.5), using the bias-corrected Gumbel fit parameters.

The main limitation of the proposed QDM bias correction for extreme daily rainfall is the assumption that a Gumbel frequency distribution will remain adequate under future climate conditions. Huang *et al.* [38] finds that the application of a mixture of distribution to perform as a transfer function for bias correction outperforms a single distribution by allowing for spatial variation of rainfall distributions in different grid cells.

Although the implementation of the parametric QDM resulted in biased-corrected estimations of Gumbel frequency distributions to represent the extreme daily rainfall in the future scenarios. This potential improvement by applying a mixture of extreme value distributions was considered to bear potential in improving the results of this initial pilot study.

4.5.3 Cross-Validation for Bias-corrected Daily Rainfall

The objective of the daily rainfall bias correction was to enable the assessment of antecedent rainfall through the derivation of mean seasonal rainfall. Thus, it was important to assess the performance of the bias correction results in determining the temporal accuracy and magnitude of error in daily precipitation simulations.

In order to assess the performance of the bias corrected climate simulations, a 3-fold cross-validation scheme was implemented. The evaluation of bias correction methods on models through cross-validation was implemented in the previous studies with calculation of the Mean Absolute Error (MAE) and the Root-Mean-Squared Error (RMSE) to measure performance [77, 78].

This study adopted a cross-validation scheme particular to the bias correction approach for daily rainfall, as shown in Figure 4.5

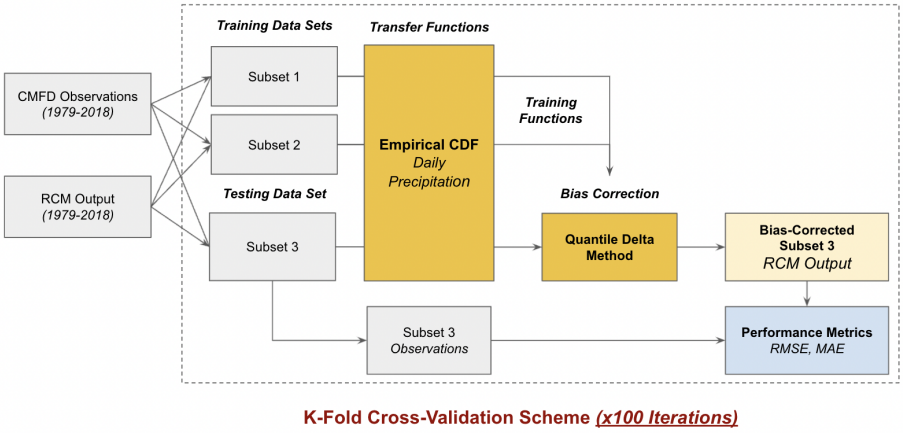

Figure 4.5: Flowchart of cross-validation procedure from splitting the data into training and testing to deriving performance metrics.

The approach was implemented by randomly sub-dividing CMFD observations and RCM outputs by 2/3 for training and 1/3 for testing. The empirical QDM bias correction method for daily rainfall was then performed. The training datasets from the CMFD observations and the RCM outputs would be references to establish the transfer functions, and correct the sub-divided testing dataset from the RCM output. The performance was assessed through testing the accuracy and magnitude of the bias-corrected RCM testing dataset versus the CMFD observation testing dataset. The performance was measured by MAE and RMSE, respectively. This procedure was performed for random subdivisions of data sets over 100 iterations to adequately assess the performance of the empirical QDM method in correcting daily rainfall data.

The strength of the k-fold cross-validation procedure is in its robustness to assess the uncertainty and deviation of climate models outputs from observations. Though critics of this method cite that long-term trends and oscillations in dynamic climate systems may lead to random realization of long-term climate variability. This would render the results of cross-validation versus observations a result of internal variability, and be unable to provide sensible insight of the bias correction [79].

The downstream dynamics of the Hengduan Mountains, and the influence from interaction of the Indian and East Asian Monsoons are internal factors of variability present that affect Wanzhou. The insight derived from the cross-validation procedure, presented in Figure 4.5, was a measure of the uncertainty and variability of the bias-corrected results.

An expanded analysis incorporating spatial aspects and statistical significance of the bias-corrected results could lead to more certain measures of performance for the QDM bias correction method.

4.5.4 Validation for Bias-corrected Extreme Daily Rainfall

The objective of the parametric QDM method for extreme rainfall was to perform a model bias correction through the comparison fitted Gumbel frequency distribution models. The evolution in magnitude and the distribution of the Gumbel fitted representation extreme daily rainfall is the intended outcome of this bias correction methodology.

The validation procedure for the extreme daily rainfall was performed through the resulting ordered maximum monthly precipitation from the bias-corrected dataset with the counterpart dataset from the CMFD observations for the months of July to August in the reference period of 1979 to 2018.

The performance for the bias correction of extreme daily rainfall was measured by Mean Absolute Error (MAE) and the Root-mean-squared Error (RMSE) of the ordered values. The intention of these error measurements was to capture the accuracy and magnitude of the bias-corrected results. Additionally, a Pearson Correlation Coefficient

was derived to assess the ability of the RCM simulation results to capture the extreme daily rainfall in the CMFD observations.

Finally, a KS test was performed to assess the ability of the bias correction method to correct the simulation results. This was performed to test if frequency distribution of extreme daily rainfall belonged to the same distribution as the observations within a confidence interval of 95%. The KS test performed followed the description in Section 4.4.

4.5.5 Climate Change Factors

In order to incorporate the trend of climate signals for extreme daily rainfall and mean seasonal rainfall, a Climate Change Factor was derived, following the relationship given the Equation (4.16).

$$CCF_i = \frac{P_{Future,Model}}{P_{Historical,Model}} \tag{4.16}$$

where CCF_i is the the effective climate change factor of or either the value of the mean seasonal rainfall, CCF_{MSR}, or extreme daily rainfall, $CCF_{EDR,T}$, for a return period, T.

The derivation of the $CCF_{EDR,T}$ for extreme daily rainfall considers, $P_{Future,Model}$, as the magnitude of rainfall on the return period curve derived from the future scenario simulations corresponding to a return period T, and $P_{Historical,Model}$, as the magnitude of rainfall on the return period curve derived from the historical simulations corresponding to return period return period T.

The derivation of the climate change factor, CCF_{MSR}, for antecedent seasonal precipitation is computed through considering the mean seasonal antecedent precipitation, taking $P_{Future,Model}$ as the mean seasonal rainfall from future scenario simulations and $P_{Historical,Model}$ as the mean seasonal rainfall derived from historical scenario simulation. A CCF_{MSR} value was was derived for future scenario simulations defined by Table 4.2.

5 Results and Discussion

This chapter presents the results and discusses the findings of this research project. The results are divided into three parts, following the presentation of the methodological framework in Figure 4.1. The first main section in the results discuss the findings from the reconstruction of historical triggering rainfall conditions. An analysis of the present mean seasonal rainfall patterns and the Gumbel distribution model of extreme daily rainfall then discussed. Finally, results of the bias correction of RCM outputs, and the climate change analysis derived from the ensemble projections are assessed.

5.1 Part 1: The Reconstruction of Triggering Rainfall Conditions

This first part of this research project was the reconstruction of event rainfall and antecedent rainfall conditions corresponding to the shallow landslides recorded in the inventory for the period of 1995-2005. The rainfall was extracted from the CMFD gridded precipitation observation and recharge estimates were applied to attain the effective antecedent recharge conditions.

An analysis of the reconstructed rainfall conditions during the summer seasons of 1995 to 2005 and an assessment of their reliability was then carried out. Temporal uncertainty in the recorded landslide date was detected for landslides occurring during periods with no estimated effective antecedent recharge that showed a magnitude of zero event rainfall.

The analysis of the sensitivity of the inventory dates to a time-shifting algorithm implemented to search for maximum triggering event rainfall within a period prior was conducted to address the lack of any rainfall in the reconstruction based on the original recording dates.

Through the exploration of uncertainty in the landslide recording dates, it was determined that significant uncertainty until 7 days prior to the original record dates would be a hindrance to the reconstruction of triggering rainfall conditions. Furthermore, an analysis of the sensitivity of antecedent rainfall conditions to this temporal uncertainty was conducted.

5.1.1 Triggering Rainfall Conditions in Summer

The coordinate-based extraction algorithm, as described in Section 4.3, was implemented to extract the rainfall information corresponding to the dates and locations found in the shallow landslide inventory. The initial results of this reconstruction for summer season rainfall conditions corresponding to shallow landslides are discussed in this section.

A density plot of the reconstructed triggering event rainfalls that occurred on the day of the landslide event and the 30-day antecedent rainfall conditions for each recorded landslide event are depicted in Figure 5.1.

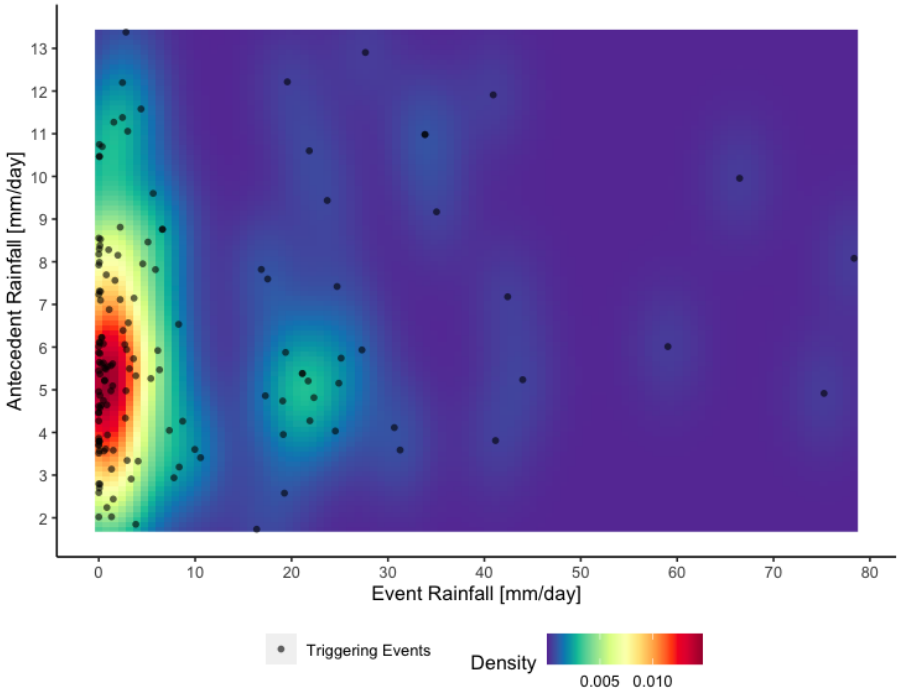

Figure 5.1: A 2D density distribution of event rainfall versus the 30-day antecedent rainfall for the reconstructed rainfall conditions for June-August 1995 to 2005.

Two prominent clusters of landslides can be observed in Figure 5.1. The first cluster shows a majority of the landslides clustered within the range of average 30-day antecedent rainfall conditions of 3 mm/day to 7 mm/day, and less than 5 mm of event rainfall.

The first cluster described indicated a group of landslides that were triggered by

significant antecedent rainfall conditions affecting stability of the soil through raising groundwater levels by subsurface lateral flow influenced by infiltrated rainfall that turns into effective antecedent recharge. This identifies possible landslides that experienced greater influence from significant antecedent rainfall and recharge conditions on soil stability rather than a large amount of event rainfall that could trigger a shallow landslide by instability while facilitating vertical flow through the soil column.

The second prevalent group is observed in Figure 5.1 is clustered around 20 mm of event rainfall with antecedent rainfall conditions between 3 mm/day and 6 mm/day. Although the event rainfall of the few landslides within this cluster is 4 times significantly larger than the first cluster discussed. A group of landslides can be found within a similar range of magnitude for antecedent rainfall. The interpretation of the 2D density plot visualization of the reconstructed rainfall conditions reveals a similarity in the two clusters triggering conditions.

The qualitative observations of this plot are indicative of the influence of antecedent rainfall conditions, but the consideration of infiltration to the groundwater table through an analysis of effective antecedent recharge is essential to determine interaction between the event rainfall and the antecedent rainfall in triggering shallow landslides.

The event rainfall and the antecedent rainfall conditions are assumed to be independent events. Thus, the distributions of the two potential triggering rainfall conditions are separately analyzed in Figure 5.2. The frequency distribution is depicted through a histogram, while an estimated density distribution curve is utilized to understand the probability distribution of the independent triggering rainfall conditions.

The frequency distribution analysis of the reconstructed event rainfall reveals that 120 out of 146 of the landslides in the inventory occurred with less than 20 mm of rainfall. These results reveal that 82% of event rainfall in this right-skewed distribution occurs with less than 20 mm of single day rainfall. Thus, supporting the earlier observation that a range of antecedent rainfall conditions in Figure 5.1 could be the dominant triggering mechanism. In contrast to the distribution of event rainfall, the distribution of 30-day averaged rainfall, representing antecedent rainfall revealed a positive skewed distribution to a lesser degree. Based on the reconstruction of rainfall conditions, a significant number of shallow landslide events occurred with antecedent rainfall conditions of 5 mm/day over a 30-day period prior.

Empirical Recharge Parameters

A more detailed estimate of the actual recharge through hydrological models was considered necessary to successfully reconstruct the antecedent conditions that triggered landslides. The calculation of the factor of rainfall converted into recharge was estimated through the EasyBal hydrological model [64]. This model utilized time series

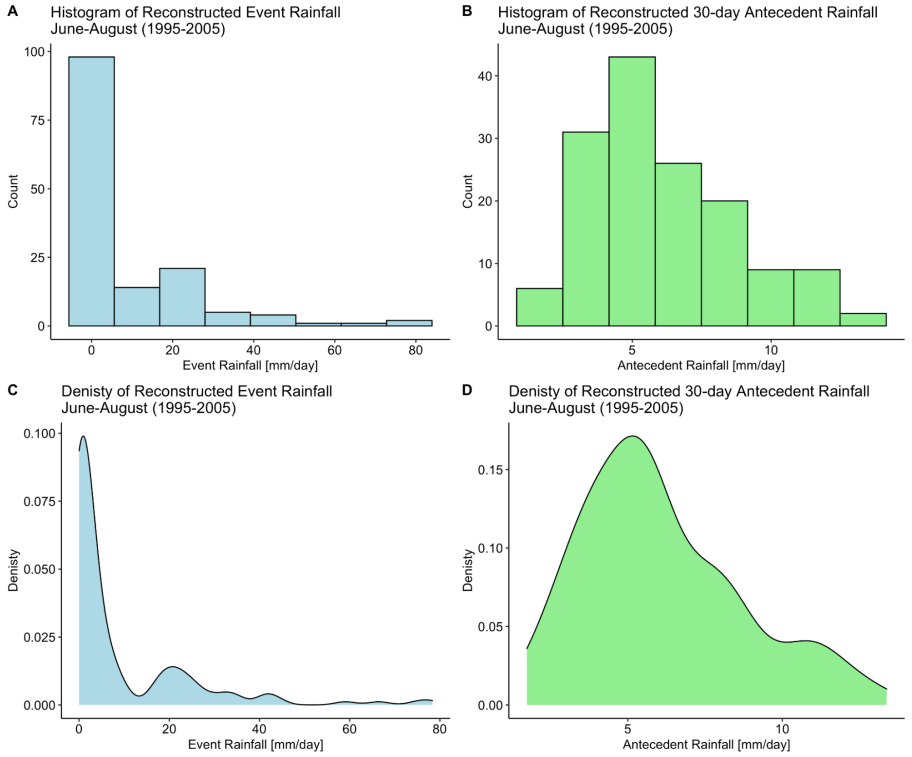

Figure 5.2: Histograms and density distributions of seasonal rainfall reconstructions for event rainfall (in blue along the left column panes), and the antecedent rainfall (in green along the right column panes.

data of temperature, precipitation and evaporation from observations at the rain gauge located at the coordinates of 30.77 N and 108.40 E.

The resulting recharge parameters were calculated to provide average monthly recharge parameters C_r that can be applied to the 30-day antecedent rainfall Pa, shown in equation Equation (2.1), to calculate the effective antecedent recharge conditions qa for the decade of interest that coincides with the shallow landslide inventory. The EasyBal calculations for 1994-2005 provide the interannual and monthly temporal variation that was used to estimate the effective antecedent recharge over the entire study area [65].

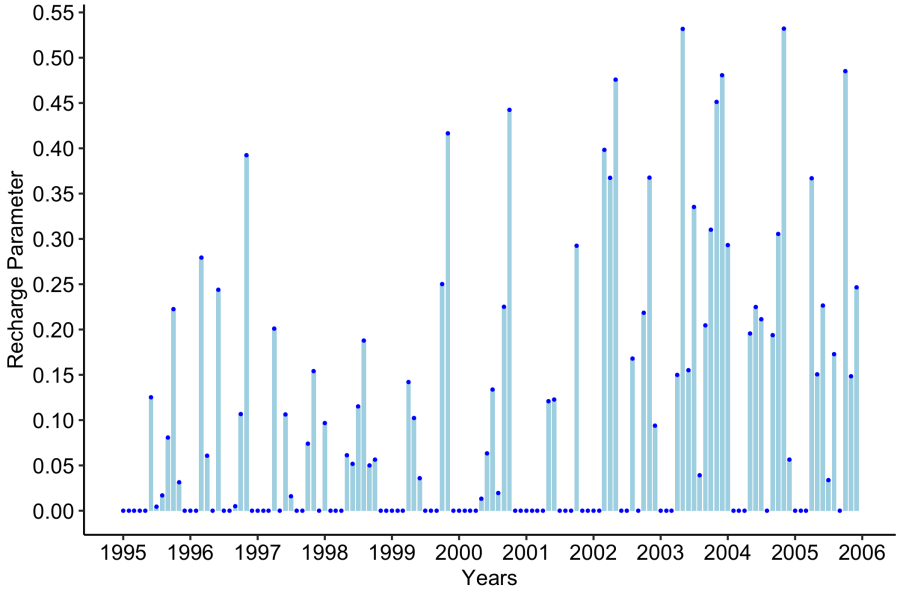

Figure 5.3: Time series of average monthly recharge parameters (C_r) over the study area for the period of 1995-2005. *Data from: [65].*

The simulation results for the average monthly recharge factor estimates from the EasyBal calculations are shown in Figure 5.3 from 1995 to 2006. Months with a recharge factor of 0 are observed to occur on an annual basis throughout the simulation with an apparent trend of increasing recharge from 2002 onward. Between 2002 and 2004, a significant increase in average monthly recharge parameters. This prompted an inter-annual and intra-seasonal analysis of the EasyBal simulation results and the resulting recharge estimates utilized in the reconstruction of triggering rainfall conditions.

Figure 5.4 presents the average recharge parameters for the period of calculation derived from the months of May to July. The seasonal recharge characteristics provide a range of 0.11 to 0.14 to characterize the effective antecedent recharge in summer

(June-August) that can be estimated using the recharge parameters from May to July. Although a majority of the shallow landslides in the study area occurred during summer, the highest recharge parameters were in the months of November and December.

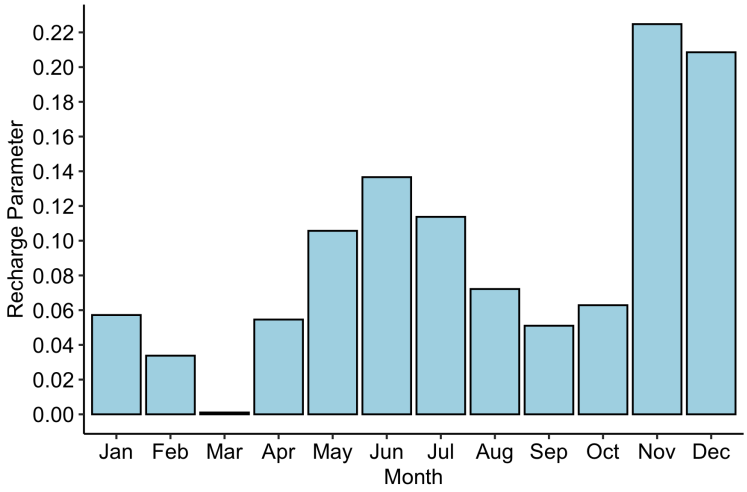

Figure 5.4: Monthly average recharge parameters (C_r) from 1995 to 2005. *Data from: [65].*

Figure 5.5 presents the interannual variation of recharge parameters for May-July for the years 1995-2005. Based on the seasonal estimates, the recharge parameters for the antecedent conditions of the summers of 2002, 2003, and 2005 were the highest in the decade with 0.28, 0.26 and 0.25 of antecedent precipitation estimated to infiltrate into recharge, respectively. It can be observed that prior to 2002, an alternating estimation of the recharge factor between 0.04 and 0.10 were calculated.

The overview of the recharge factor calculations suggests that significant changes affecting the hydrological cycle yielded higher than normal recharge estimations. In effect, this indicates that the contribution of recharge to the instability of soil was a significant trigger for shallow landslides from 2002-2005.

Effective Antecedent Recharge

The effective antecedent recharge was calculated following Equation (2.1) for all shallow landslide occurrences in the inventory. Figure 5.6 presents a histogram of the frequency distribution and a density estimate of the probability distribution for the estimated effective antecedent recharge conditions.

In contrast to the antecedent rainfall distributions, the distribution of effective antecedent recharge showd distinct similarities to the positively skewed event rainfall shown in Figure 5.2. Based on the recharge estimates, 110 out of 146 shallow landslides

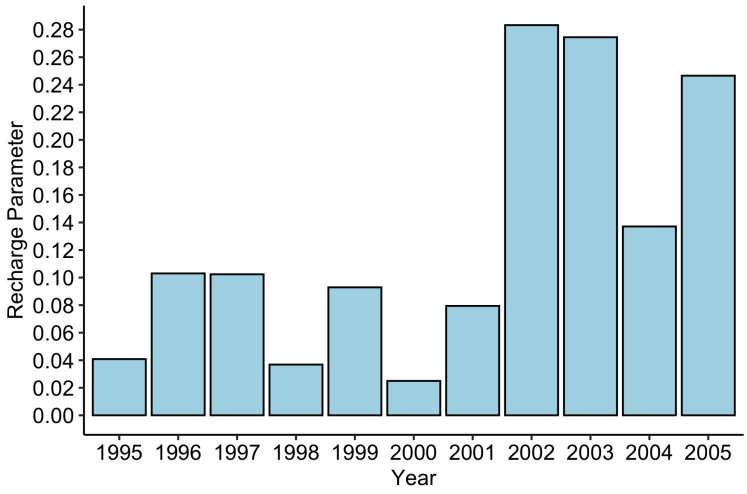

Figure 5.5: Yearly average recharge parameters (C_r) from May to July of 1995 to 2005. *Data from: [65].*

occurring between June to August were triggered with 30-day effective antecedent recharge conditions of less than 1 mm/day.

The results of the effective antecedent recharge estimates indicated that 75% of the shallow landslides occurred with less than 1 mm/day recharge over a 30-day period, while the earlier analysis of reconstructed event rainfall revealed that 82% of the landslides depicted in Figure 5.2 occurred with less than 20 mm of rainfall. Further analysis of the event rainfall reveals that 66% of landslides occurred with less than 5 mm of event rainfall and 42% of landslides occurred with 0 mm of event rainfall.

The implications of the observations point to a lack of significant event rainfall based on the reconstruction performed. This raised concerns surrounding possible spatial and temporal uncertainties in the landslide inventory, and the inability for the CMFD gridded observation data set to capture local scale convective rainfall patterns that could have triggered the shallow landslides.

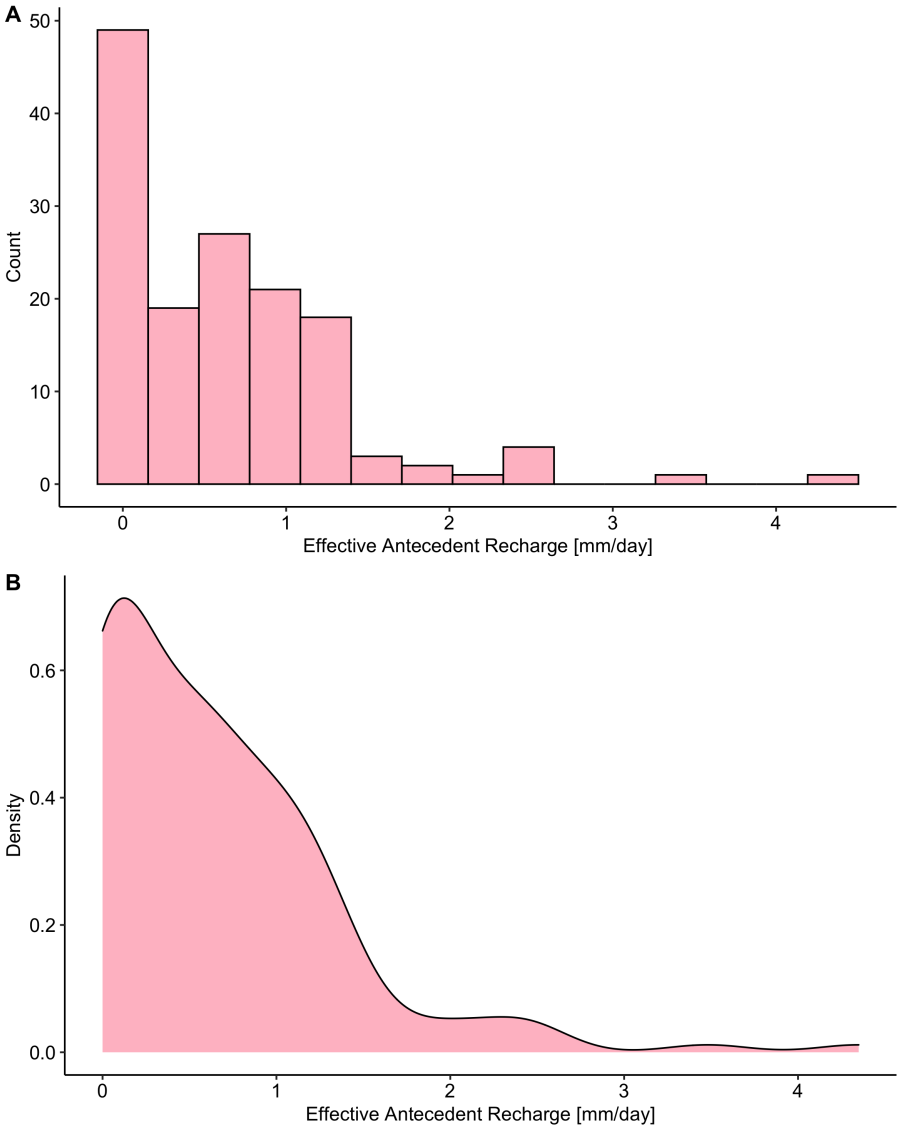

Figure 5.6: Histogram (A) and density distribution (B) of the reconstructed 30-day mean effective antecedent recharge for landslides occurring between June to August 1995 to 2005.

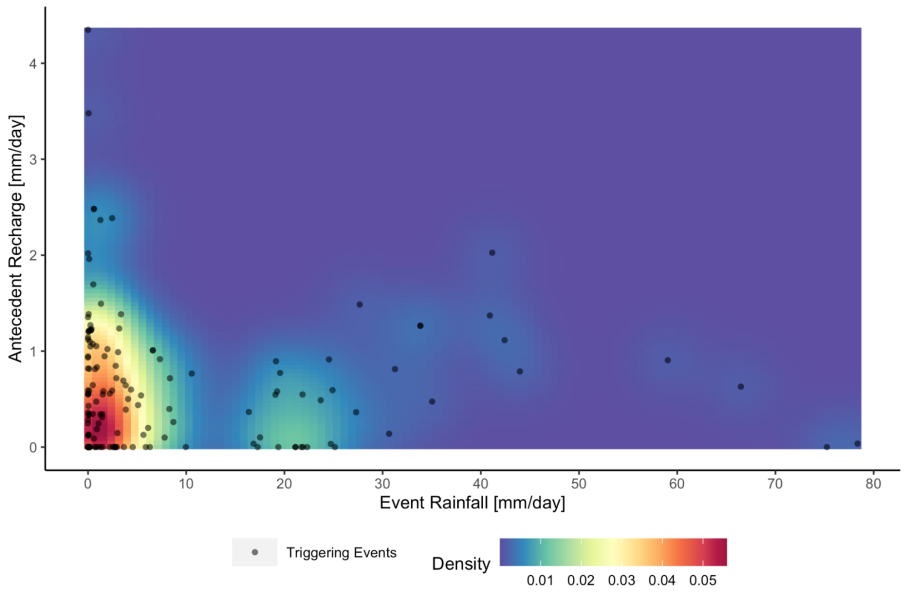

Figure 5.7: A 2D density distribution of Event Rainfall versus the 30-day Effective Antecedent Recharge from June to August 1995 to 2005.

Figure 5.7 depicts the 2D density distribution of the reconstructed effective antecedent recharge and event rainfall. The concerns over uncertainties in the data and the ability to reconstruct triggering rainfall conditions are highlighted in the cluster of landslide occurrence seen with a range of effective antecedent recharge of 0 mm/day to 1 mm/day, and event rainfall between 0 mm/day to 10 mm/day.

This cluster of occurrences highlights the uncertainties in the data sets used to reconstruct the shallow landslide triggering rainfall conditions. The observation of this cluster prompted a deeper analysis in the potential temporal uncertainty in record date as a feasible initial correction step to be able to utilize the inventory and proceed with reconstructing the hydro-meteorological conditions for shallow landslide triggering in the study area.

Although a large cluster of landslides Figure 5.7 occur with no apparent hydro-meteorological forcing acting as the triggering mechanism, a cluster of landslides occurs with a range of effective antecedent recharge of 0 mm/day to 1 mm/day and event rainfall between 15 mm/day to 25 mm/day. This cluster of landslides represent reasonably reconstructed triggering rainfall conditions that can be utilized in the calibration of models for a susceptibility analysis.

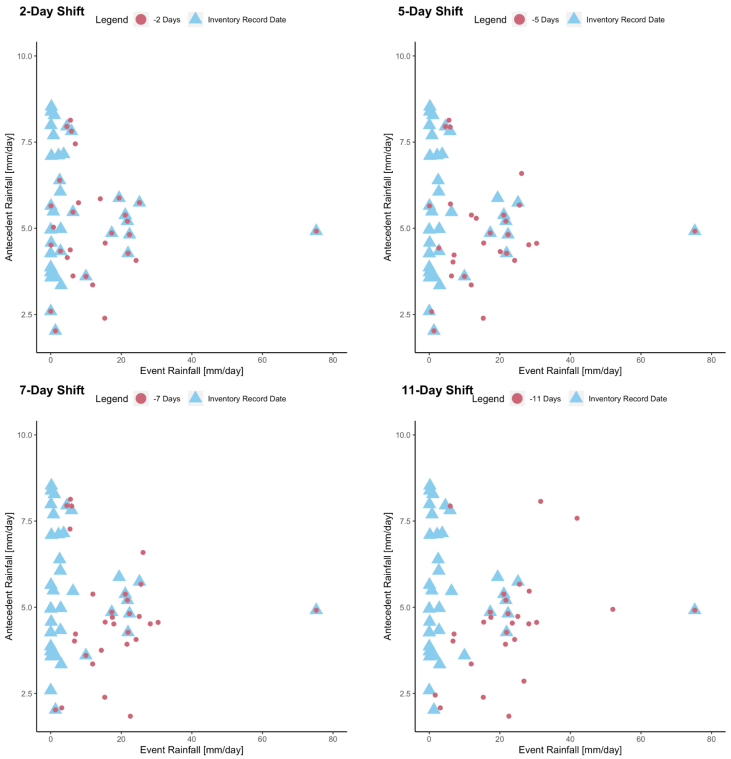

Figure 5.8: A comparison of the effect of the time-shifting algorithm (in red circles) for 2 to 11 day periods (left to right, top to bottom) and the difference between the original record dates (in blue triangles) with focus on reconstructed rainfall conditions occurring during summer season months from 1995-2005 with no estimated recharge.

5.1.2 An Assessment of Temporal Uncertainty in the Inventory

The potential for uncertainties to exist in shallow landslide inventories is common and problematic for the assessment of shallow landslide susceptibility. This is especially problematic since landslide inventories and known landslide occurrences are utilized to calibrate models used to generate triggering thresholds and spatial predictions.

The resulting clusters of landslides with no significant triggering hydro-meteorological conditions in the initial reconstruction of triggering rainfall conditions, it was determined that the most feasible solution for this study to address the general uncertainty in the inventory would be to assess the temporal uncertainty in the record dates.

Other uncertainties in the data sets used to reconstruct the triggering rainfall conditions such as the spatial uncertainty of the locations of the landslides and the uncertainty in the ability for the CMFD gridded precipitation reanalysis to capture intense local-scale rainfall after the spatial interpolation and processing were identified as limitations that require further time and resources to address.

As identified in Figure 5.7, the cluster of landslides showing no effective antecedent recharge and no event rainfall was selected and put in focus for the assessment of temporal uncertainty in the inventory. The approach assumed that due to operational constraints, and procedure for recording sighted shallow landslides by the personnel recording the occurrences, it is possible that the record dates stated in the inventory were the dates in which these personnel sighted the landslide, and not the actual dates of failure. Therefore, this temporal uncertainty in recording dates was assessed using a time-shifting approach that searched for the maximum event rainfall in the CMFD precipitation observations of the pixel representing the rainfall conditions of the landslide location within a period of 1 to 11 days prior to the record date found in the inventory.

The implementation of this time-shifting solution to address temporal uncertainty was assessed through the examination of critical 0 mm/day effective antecedent recharge that represented 37 landslides, or 25% of the reconstructed inventory. The results of the time-shift algorithm's search for a maximum event rainfall compared to the original inventory date is shown Figure 5.8.

The shift in the magnitude of event rainfall observed after a 2-Day and 5-Day shifting window was applied. This revealed shifts in position from 0 mm/day of event rainfall towards 20 mm/day of event rainfall for 10 occurrences. There was no shift in record date of landslides around the 20 mm/day threshold observed. The change in position of dates resulting in event rainfall placed in the 20 mm/day region was also observed in a 7-day period.

These results suggest that the presence of the temporal uncertainty in the originally reconstructed rainfall data set that was based on the initial recording date in the inventory. Although an agglomeration of event rainfall shifted to a range within the 20

mm/day threshold is observed consistently from a 2-Day to 7-Day shift, the expansion of the time shifting period to 11 days reveals expanded uncertainty with larger magnitudes of shifts surfacing. This indicates the possibility of an even longer period of uncertainty and more significant and higher magnitudes of event rainfall during months estimated to have zero effective antecedent recharge.

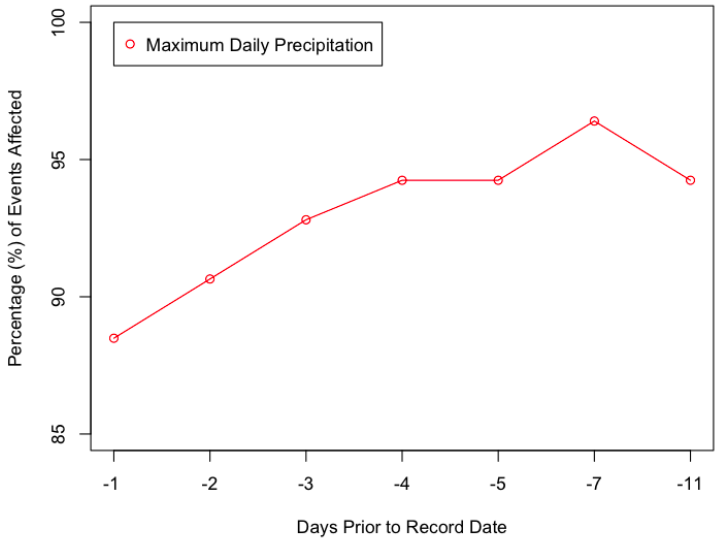

Figure 5.9: A comparison of the percentage of the inventory affected by the detection of a maximum event rainfall for different periods of days prior to the record date

The assessment of the time-shifting solution was expanded from its focus on landslide occurrences with no effective antecedent recharge to all the occurrences in the inventory. The percentage of data points shifted from their original record dates based on maximum event rainfall found in the CMFD data set is presented in Figure 5.9 for the time-shifting windows of 1 to 11 days prior to the record date.

The results that a shift to find a maximum event rainfall of one day changes 88% of the event rainfall based on the original recording dates. There is a noticeable increase in the number of landslides affected in the application of a maximum event rainfall search algorithm in the data set from a 1-Day search period to a 7-Day period, increasing from 88% to 96% of the data set changing. Between 7 and 11 days, there is a difference of 2%, from 96% of the data set changing after a 7-day search period is applied to 94% with an 11-day period.

It can be observed that a period of relative stability between a 4-Day and a 5-Day

search period suggests that no significant change in data points when searching for the maximum triggering event rainfall. The results of this assessment of the sensitivity of the reconstructed event rainfall indicates large uncertainty in the record date and its representation of the day the recorded shallow landslides were triggered.

Based on the results of this assessment, the implementation of a 7-Day window to represent maximum uncertainty in the event rainfall and best represent the reconstruction of landslide triggering hydro-meteorological conditions was further assessed.

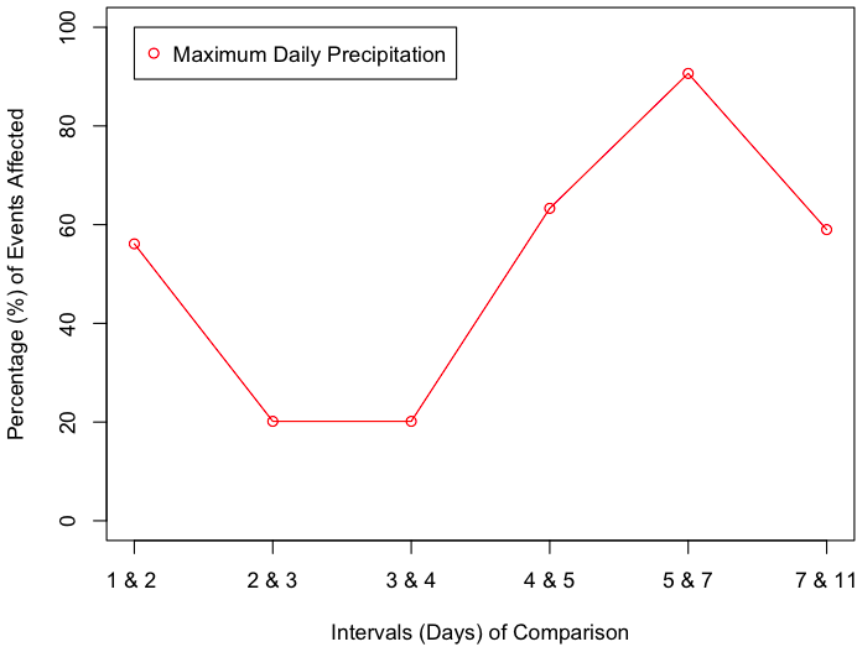

Figure 5.10: An inter-comparison between the percentage of the inventory affected by the detection of maximum event rainfall between paired intervals of consecutive days prior to the record date.

In order to support the adequacy of a 7-Day period prior to the original record date in the inventory to reasonably represent the uncertainty at the maximum and adequately allow insight from the reconstruction of rainfall conditions, the difference between time periods of shifted data sets was assessed. This was intended to examine the number of landslide occurrences affected between time-shifting periods to understand

the movement of data points towards a maximum event rainfall and the stability of each period of search.

The intercomparison of inventory data points affected between each time-shifting period previously analyzed is presented in Figure 5.10. In contrast to Figure 5.9, this analysis of the movement of data points and the search for a probably triggering event rainfall reveals a point of relative stability between the time-shifted periods of 2-3 days and 3-4 days. In these 3 periods, 20% of data points changed when an algorithm to search for the maximum event rainfall was applied. When compared to the original record dates, this period sees 91% to 94% of data points increase.

In contrast to the observed stability of the 4 to 5 day search period in the Figure 5.9, the intercomparison of data points in Figure 5.10 indicates that between the 4-5 day search period reveals that 63% of the data points were shifted. This relative stability is not consistent in Figure 5.9 and Figure 5.10.

The 7-Day search window emerged as the period of maximum uncertainty, where a comparison to the 5-Day window yielded 91% of data points changing in the search for a maximum event rainfall. While the change between a 7 and 11-day search period was less prominent, with 59% of data points finding a new maximum event rainfall, the uncertainty is still significant.

The first assessments implemented in this section aimed to understand the sensitivity of the rainfall conditions reconstructed around the original record dates to a time-shifting solution to search for the maximum daily rainfall. The second assessment established the relative stability of the data sets created by the maximum daily rainfall search algorithm for different periods of uncertainty, in days prior to the original record date.

These assessments were utilized to assess the temporal uncertainty and the adequacy of a time-shifting solution to address the temporal uncertainty in the inventory. The sensitivity analysis presented indicates that the 7-Day period represented conditions of maximum uncertainty. Therefore, this maximum period of uncertainty was taken into account and used to further analyze the reconstructed triggering rainfall conditions that this part of the research project aimed to achieve.

Incorporating a 7-Day Period of Uncertainty

The resulting assessment of temporal uncertainty in the inventory resulted in the selection of a 7-day period to reconstruct the triggering rainfall conditions This period represents the maximum uncertainty when considering a period of 1 to 11 days prior to the originally recorded inventory dates. The critical assessment of uncertainty began with shallow landslide events that occurred during periods with no estimated recharge.

The reconstructed data set reveals groups of data that, despite the time-shifting solution, show negligible event rainfall as the triggering mechanism. Consistently

observed with the reconstruction around the original record dates is an apparent gravitation of landslides around the 20 mm/day threshold of triggering event rainfall.

A group of landslide events occurring from July to August 2002 suggest that operational constraints in identifying and recording landslides manifested in the delay of recording to the inventory. The study area covers 3,457 km and identifying and monitoring shallow landslides in this region is a challenging task.

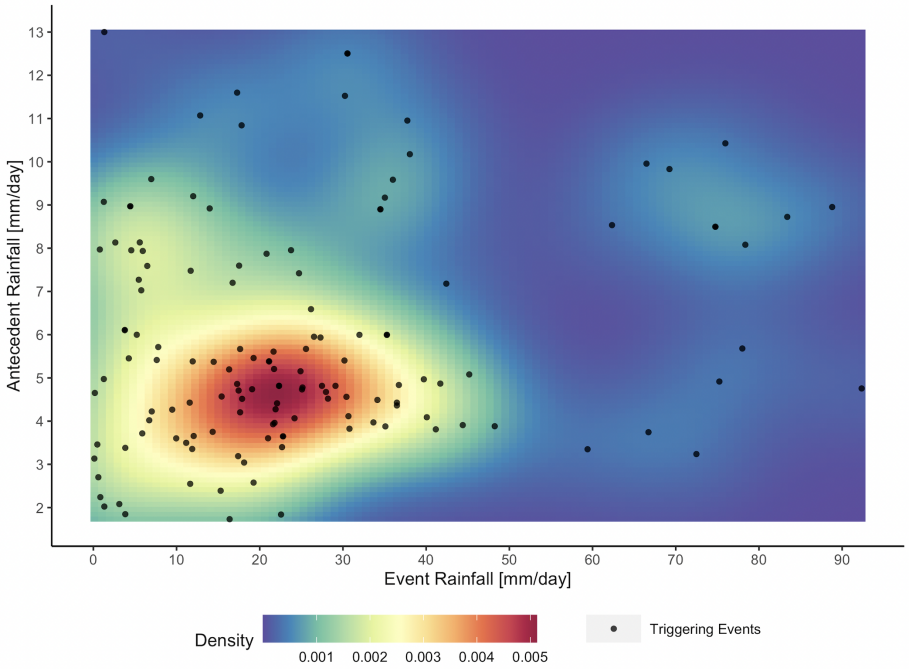

Figure 5.11: A 2D density plot of the event rainfall and the antecedent rainfall with a 7-day uncertainty period applied occurring from June-August 1995-2005.

The implementation of the 7-Day time-shift solution to account for the temporal uncertainty in record dates was applied to the entire data set. The 2D density plot of the reconstructed antecedent rainfall and event rainfall magnitudes incorporating the record date uncertainty is presented in the Figure 5.11.

Similar to 2D density plot of the reconstructed triggering rainfall conditions, based on the original recording dates in Figure 5.1, the antecedent rainfall estimates in the main cluster of landslides in Figure 5.11. This suggests that the occurrence of shallow landslides correspond to a range of antecedent rainfall from 3 mm/day to 6 mm/day.

While the shift in rainfall conditions suggest a concurrent occurrence with the event rainfall of 10 mm/day and 30 mm/day. In contrast to the results of the reconstructed rainfall conditions without the incorporation of record date uncertainty, a cluster of

event rainfall and antecedent rainfall conditions is more clearly depicted with event rainfall from 60 mm/day to 90 mm/day and antecedent rainfall between 8 mm/day and 11 mm/day.

The graphical interpretation of the relationship between antecedent rainfall and event rainfall conducted in this section may add insight to establishing thresholds of occurrence and suggest ranges of rainfall by which shallow landslide susceptibility modelers can begin their risk assessments of the study area.

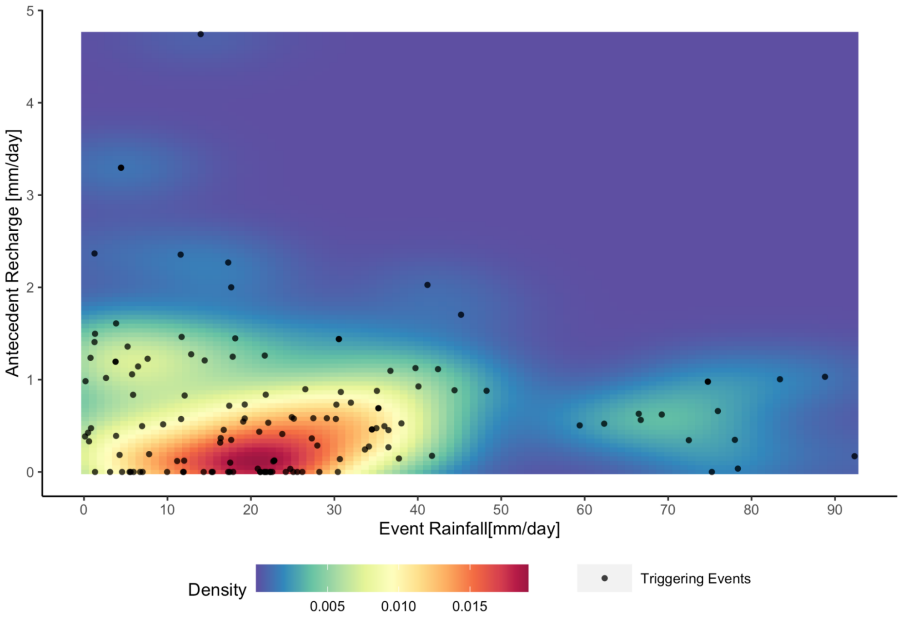

Figure 5.12: A 2D density plot of the event rainfall and the effective antecedent recharge resulting 7-Day uncertainty period occurring from June-August 1995-2005.

The analysis of the reconstructed rainfall conditions incorporating temporal uncertainty in the record dates was extended to the estimated antecedent rainfall. The 2D density plot of the reconstructed data set is shown in Figure 5.12.

The dominant cluster of landslides assessed in Figure 5.11 shifted downward towards the x-axis, reflecting that a significant number of shallow landslides occurred during months estimated to have no effective antecedent recharge. This cluster suggests a majority of landslides occur with effective antecedent recharge conditions between 0 mm/day and 1 mm/day and accompanied by a wide spread of event rainfall between 5 mm/day and 30 mm/day.

Two clusters of landslide occurrences also formed in the visualisation of density in the

data set, indicate potential combinations of rainfall conditions that can be considered as higher magnitude event rainfall. The first cluster is located with a range of effective antecedent recharge between 0 mm/day and 1 mm/day, and event rainfall between 60 mm/day and 90 mm/day suggests a group of landslides that were triggered by failure of the soil column through the vertical flow process.

The second group of clustered landslides suggests that significant effective antecedent recharge more than event rainfall triggered the shallow landslides. This cluster is located with effective antecedent recharge of 1 mm/day to 1.5 mm/day and event rainfall of 0 mm/day to 10 mm/day. This group of landslides suggests this combination of antecedent rainfall and a minute amount of event rainfall enabled the triggering mechanism through a raised groundwater head by the process of lateral subsurface flow paired with vertical flow through the soil column.

Although these results can be insightful in approaches incorporating soil mechanics and physics-based triggering mechanisms, from a standpoint of threshold determination and data-driven insight the uncertainty and the wide range of the clustered landslide occurrences does not give clear insight into the triggering mechanisms and scenarios for shallow landslides in the study area. The results of this section suggest that based on the cluster of event rainfall with large values, an assessment and analysis of extreme daily rainfall distributions across the study area could provide valuable insight into the modeling shallow landslide susceptibility under extreme conditions.

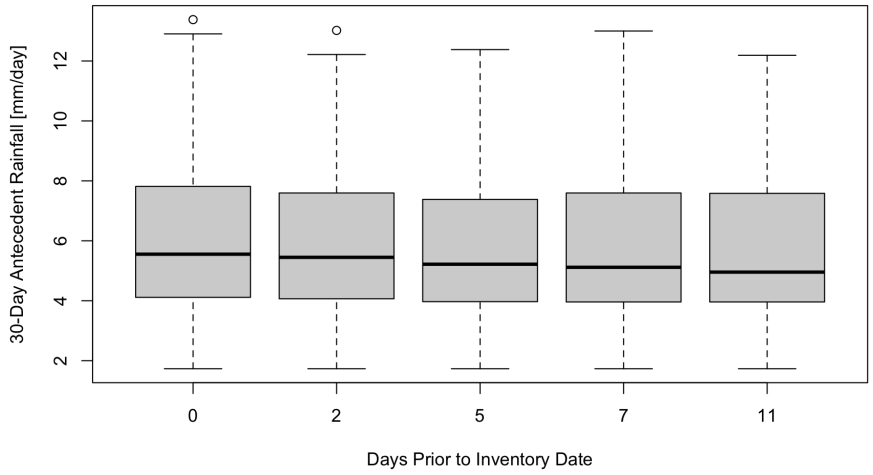

Figure 5.13: Box Plot comparison of the 30-day mean antecedent rainfall for landslides occurring in June-August with the consideration of temporal uncertainty under different intervals of days prior to the inventory record date.

The Influence of Uncertainty on Antecedent Rainfall

The assessment of the impact of the time-shifting on temporal uncertainty on the triggering rainfall conditions has been the focus of the discussion of results in the reconstruction of the triggering rainfall conditions and antecedent conditions until this point.

This section analyzes the antecedent conditions with the objective of quantifying the influence of the time-shifting solution on the 30-day mean rainfall, the distribution of rainfall magnitudes and the sensitivity of different antecedent periods of consideration to the time-shifting. Through the results of these two assessments, the characteristics of the distribution of landslide-triggering antecedent rainfall conditions is compared to the distribution of observed antecedent rainfall.

The reconstructed summer rainfall conditions were selected as the period of consideration, given the frequent occurrences of shallow landslides seen in the inventory from June to August over the decade of 1995-2005. It was also established that a period of 30-day prior to a landslide event would be an adequate representation of triggering antecedent conditions. Therefore antecedent conditions for the landslide assessment in summer is derived from the rainfall and recharge conditions occurring from May to July.

Figure 5.13 presented the comparison of reconstructed triggering antecedent rainfall for June-August from 1995 to 2005. The box plot visualization reveals that the antecedent rainfall is not as volatile and sensitive to the time-shifting solution as compared to the event rainfall. The mean triggering antecedent rainfall conditions in the summer fluctuates around 5 mm/day.

Furthermore, the interquartile ranges presented in Figure 5.13 show no visible differences between 2 to 11 days nor the antecedent rainfall reconstructed based on the original recording date, represented by '0' days prior in Figure 5.13. Thus, the selection of a 7-day time-shifting period in incorporating temporal uncertainty in the reconstruction of triggering rainfall conditions based on event rainfall sensitivity is supported by this analysis.

The second analysis in this section revolves around the assessment of the robustness of the selection of 30-day averaged rainfall to represent the antecedent rainfall conditions in the reconstruction of triggering rainfall conditions. This notion is tested through the comparison of the sensitivity of three antecedent periods to the temporal uncertainty of the inventory record date.

The periods for antecedent rainfall conditions taken into consideration for this analysis were the 30, 15 and 10-day periods to calculate mean rainfall. The antecedent rainfall was then reconstructed and assessed using results from the time-shifting algorithm to search maximum event rainfall discussed in Section 4.3. The assessment of the robustness in this analysis revolved around the comparison of the distribution of antecedent rainfalls, considering a comparison with the reconstructed antecedent rainfall from the time-shifting period of 2, 5, 7 and 11 days prior to the inventory record. Figure 5.14 is a visual representation of the distributions for this analysis.

The distribution of 30-day averaged daily rainfall when subjected to periods of time-shifting reveal a retention of a similar shape, where the density within the range of 5 mm/day shifts gradually across the different periods of uncertainty. Although there is an evident change in shape in the initial distribution of antecedent rainfall reconstructed around the original inventory dates, the stability of the shape around the tails across the implemented periods of uncertainty was observed.

The 15-day averaged rainfall follows a similar pattern of distribution of accumulated density around 5 mm/day observed between the periods of uncertainty considered in the time-shifting analysis and the reconstruction around the original record dates. A deviation in the tails is observed in the distributions of the 15-day antecedent rainfall in the tail sections showing variation in the measurement of larger average rainfall magnitudes over the 15 days. The deviation from the original inventory date distribution to the 2-day time-shifting period shows the most evident variation in the distribution of antecedent rainfall at the tails. There is an observed convergence of 15-day antecedent rainfall estimates at the tails for the time-shifting period of 5 to 11 days.

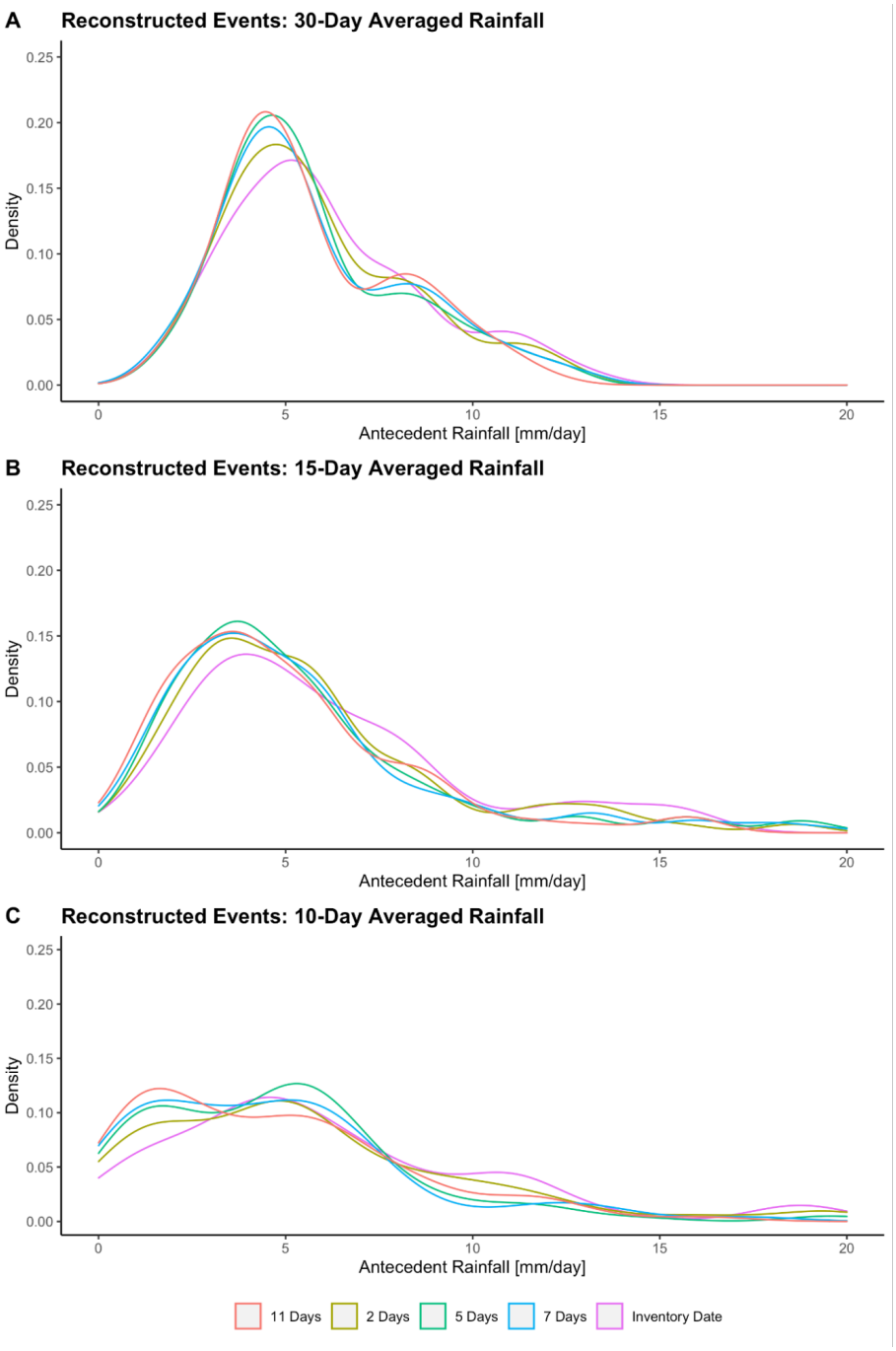

Figure 5.14: Density distributions of 30, 15 and 10-day mean antecedent rainfall (top to bottom) reconstructed around the original inventory record date and results of the time-shifted results of 2 to 11 days.

The distributions observed under the consideration of the 10-day average rainfall subjected to the time-shifting uncertainty periods reveal uncertainty and relative instability of the estimations on both tails across the range of reconstructed antecedent rainfall. Compared to the initial distribution of antecedent rainfall based on the reconstruction around the original record dates, an observed variation in distributions towards the tail for low magnitude antecedent rainfall ranges from 0 mm/day to 5 mm/day. The tails of higher magnitude antecedent rainfall show significant deviation of distributions between all periods of time-shifting uncertainty considered around 10 mm/day, with an apparent convergence at the 15 mm/day mark.

The graphical analysis of the 10-day average rainfall estimations when subjected to the temporal uncertainty shows variation and divergence of the estimations across different periods of uncertainty. Thus, these observations indicate that it is not as robust as the 15-day and 30-day average rainfall estimates when subjected to temporal uncertainty in the record date.

The assessment of the influence of temporal uncertainty presented in the discussion of Section 5.1.2 resulted in the determination of a 7-day period of uncertainty to perform a time-shifting algorithm. Thus, an assessment of the influence of the 7-day consideration of uncertainty on the antecedent rainfall was further analyzed through a comparison of the empirically-derived cumulative distribution functions and the measurement of maximum vertical deviation between the 7-day time-shift derived distributions from the original inventory dates. The objective of this analysis is to quantify the sensitivity of antecedent rainfall conditions to the time-shifting solution applied to assess the temporal uncertainty of the inventory dates.

Figure 5.15 depicts the plots of the empirically derived CDFs of the antecedent rainfall constructed based on the unaltered inventory dates, and the CDFs for rainfall derived from a 7-day time-shift in considering periods of antecedent rainfall of 30, 15 and 10 days. A visual assessment of the three plots in Figure Figure 5.15 shows larger deviations between the inventory-date derived CDF and the 7-day window CDFs for the antecedent periods of 15 and 10 days.

A Kolmogorov-Smirnov (KS) Test was implemented to quantify the deviation of the CDFs of different antecedent rainfall durations subjected to a 7-day uncertainty window from that of the original inventory date. This assessment performs a KS test between the antecedent rainfall data sets subjected to a 7-day time-shift and those reconstructed based on the original record dates to assess the sensitivity of different rainfall durations to the uncertainty and determine the robustness of the assumption. The results of the test are presented in Table 5.1.

The test results indicate that the antecedent rainfall durations of 30 and 15 days when subjected to an uncertainty time-shift are statistically similar and belong to the same distribution as the unaltered inventory record date's antecedent rainfall.

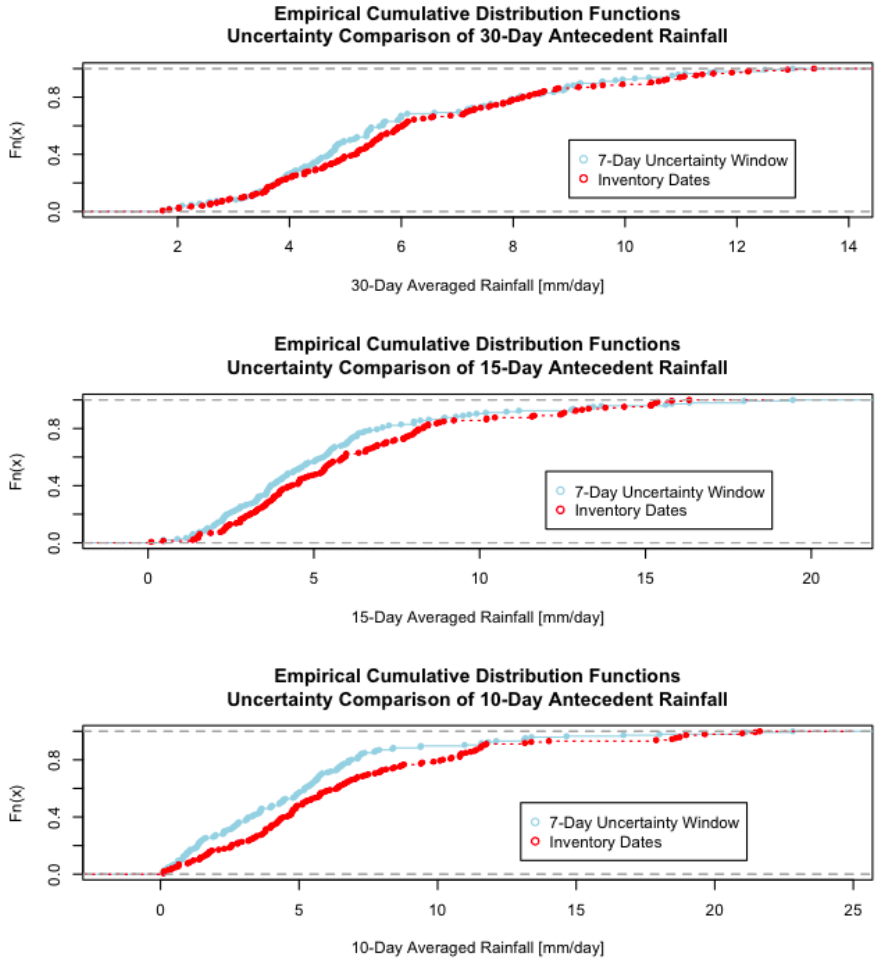

Figure 5.15: Comparison of the empirical cumulative distribution functions ($F(x)$) derived from the original record date and the results of a 7-day period of uncertainty for 30, 15 and 10 day periods of antecedent rainfall (top to bottom).

The p-values from the KS Test, shown in Table 5.1 for durations of 30 and 15 days indicate the distribution of rainfall is within the 95% confidence interval with p-values of 0.22 and 0.10, respectively. Meanwhile, KS Test results for the 10-day antecedent rainfall duration indicate that once the 7-day time-shifting window is applied, there is a statistically significant deviation from the initial distribution from record date-derived reconstruction.

Table 5.1: Summary of the Kolmogorov-Smirnov (KS) Test results between CDFs of the original record date data and the 7-day time-shifted data for different antecedent durations.

	30 Days	**15 Days**	**10 Days**
KS Test Statistic	0.12	0.14	0.18
P-Value	0.22	0.10	0.01

A graphical analysis of the interaction between antecedent rainfall distributions and time-shifting windows of uncertainty and a qualitative assessment comparison of empirically-derived cumulative distributions by KS test was performed in this section. The results presented in this section indicate that the assumption 30-day period to reconstruct antecedent conditions is a robust and reasonable estimate given the temporal uncertainty in the inventory's recording date.

The qualitative and graphical analysis of different antecedent rainfall periods when subjected to different time-shifting periods to address the temporary uncertainty indicate that the robustness of assessing antecedent triggering conditions over a longer period of time is intuitively more robust than a shorter period of consideration. The averaged value of antecedent rainfall over a longer temporal duration will be less likely to be influenced by uncertainty in daily rainfall periods for durations of consideration between 1-10 days.

5.1.3 An Analysis of the Reconstructed Antecedent Rainfall

The results presented throughout this chapter have established that the temporal uncertainty in the record dates of the inventory can be reasonably addressed by incorporating a time-shift solution to incorporate maximum uncertainty within a 7-day window to reconstruct triggering rainfall conditions. An analysis of the influence of the incorporation of a 7-day window of uncertainty on antecedent rainfall conditions was also assessed, and the results suggest that a 30-day antecedent rainfall duration can provide a reasonable and robust estimation of antecedent conditions with the incorporation of uncertainty from the inventory. The final section of results in this chapter analyzes the distribution of triggering rainfall conditions for summer season shallow landslides based on the precipitation observations derived from the spatially distributed CMFD data set.

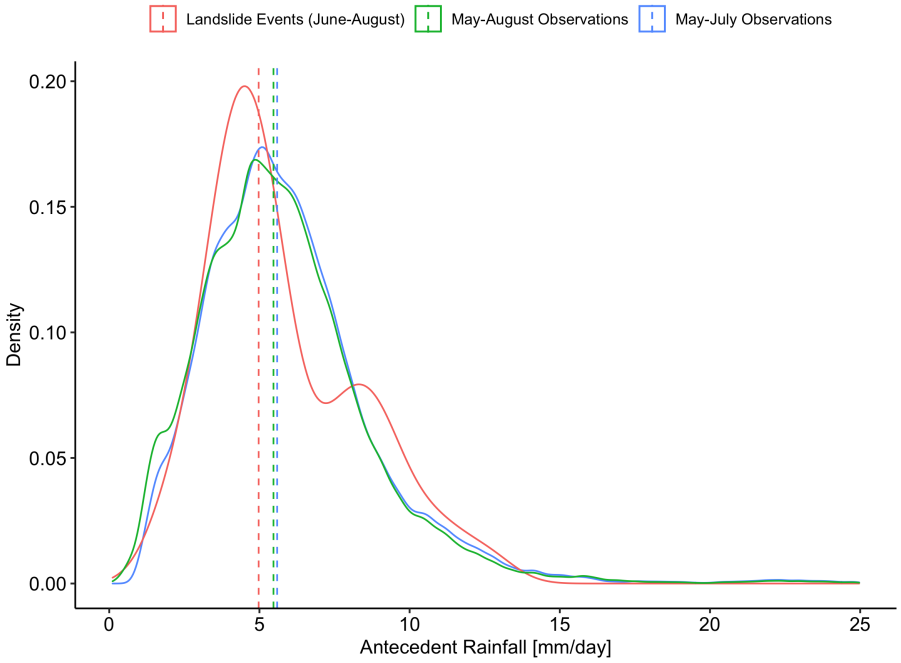

Figure 5.16: Comparison of the density distributions of antecedent rainfall of the reconstructed inventory with a 7-day window of uncertainty and the distribution antecedent rainfall in CMFD observations from 1995 to 2005.

Figure 5.16 compares the distribution of antecedent rainfall of the reconstructed summer season triggering rainfall conditions with the antecedent rainfall observations from all CMFD pixels within the study area. The 30-day average rainfall is derived from CMFD observations across the study area for the months of May-July to represent all possible antecedent rainfall conditions from 1995-2005. The distribution of 30-day antecedent rainfall derived from a 7-day time-shift solution is also visualized in Figure 5.16.

There is an apparent similarity between the distributions of the two data sets described in the plot of Figure 5.16, with the medians of each distribution, depicted by vertical dashed lines appearing to be apart by a small difference. A Wilcoxon Rank Sum Test was performed to assess if the difference between the medians of both distributions bore statistically significant similarities.

The test statistic comparing both 30-day antecedent rainfall data sets returned a p-value of 0.428, indicating strong statistical significance within a 95% confidence interval that the location of the medians of both distributions can be considered similar. Furthermore, a comparison of the distribution of the 30-day antecedent rainfall from May-July and May-August identical distributions, and similar medians, shown in Figure 5.16. This indicates that mean seasonal rainfall from May to August can adequately represent the average antecedent rainfall conditions that were likely to have triggered shallow landslides from 1995-2005.

The analysis on Figure 5.16 suggests that shallow landslides occurring during the summer season across Wanzhou from 1995 to 2005 were triggered by a range of antecedent rainfall amounts distributed similarly rainfall that fell over the entire study area. The distribution of reconstructed 30-day antecedent rainfall conditions that triggered landslides in the inventory show statistical similarity in mean of that distributed in the observation data of rainfall between May to August. Hence, indicating that in the assessment of shallow landslide susceptibility, the mean seasonal rainfall conditions can adequately represent conditions for shallow landslide triggering, as revealed by the reconstruction of the inventory data set. An important implication of this finding is that mean seasonal rainfall can be applied as an antecedent condition when modeling shallow landslide susceptibility in the future.

5.2 Part 2: An Analysis of the Present Summer Season Rainfall

The second part of this research project fulfills the objective of analyzing the present extreme daily rainfall and the mean seasonal rainfall during the summer in Wanzhou County, China. The objective of the results of this process is the establishment of a reference scenario in the present by which climate change signals from climate projections can be applied to.

The period of analysis of this section is between 1979 and 2018, corresponding to the duration by which the CMFD gridded precipitation observations are available for. Using these gridded precipitations, the mean seasonal rainfall from May to August, is analyzed. After which, extreme daily rainfall (EDR) events during this season are extracted using a block maxima approach. Using the extracted EDR within the season, the frequency distribution is modeled through fitting a Gumbel distribution. The extreme frequency distribution fits are implemented for all CMFD pixels within the study area and validated against three goodness-of-fit tests, namely the Kolmogorov-Smirnov (KS) Test, the Anderson-Darling (AD) Test, and the Cramer-von-Mises (CVM) Criterion Test.

The spatial distribution of the extreme daily rainfall and an analysis of the return period curves within the study were then analyzed. The resulting spatially distributed information on mean seasonal rainfall and extreme daily rainfall distributions were therefore established as the reference rainfall scenarios for the assessment of future climate change projections.

5.2.1 A Spatio-Temporal Analysis of Mean Monthly Rainfall

The landslide season in this study area identified June to August as high occurrence months based on the inventory. It was established that antecedent rainfall conditions play an important role in the determination of the groundwater head, and thus the susceptibility of the soil column against shallow landslide failure. In this section an analysis of the seasonal mean seasonal rainfall (MSR) over Wanzhou is conducted over the 40-year period of spatially distributed data from the CMFD gridded observation dataset.

Although the landslide season is defined as June to August, the months of May to August were considered in the definition of seasonal rainfall for this section. The observations in Section 5.1.3 finds that mean seasonal rainfall conditions were found to represent triggering rainfall conditions, shown in Figure 5.16. This temporal perspective was adapted to assess the antecedent rainfall conditions that influence the lateral subsurface flow in June, while including the potential influence of rainfall conditions in August to the subsurface flow.

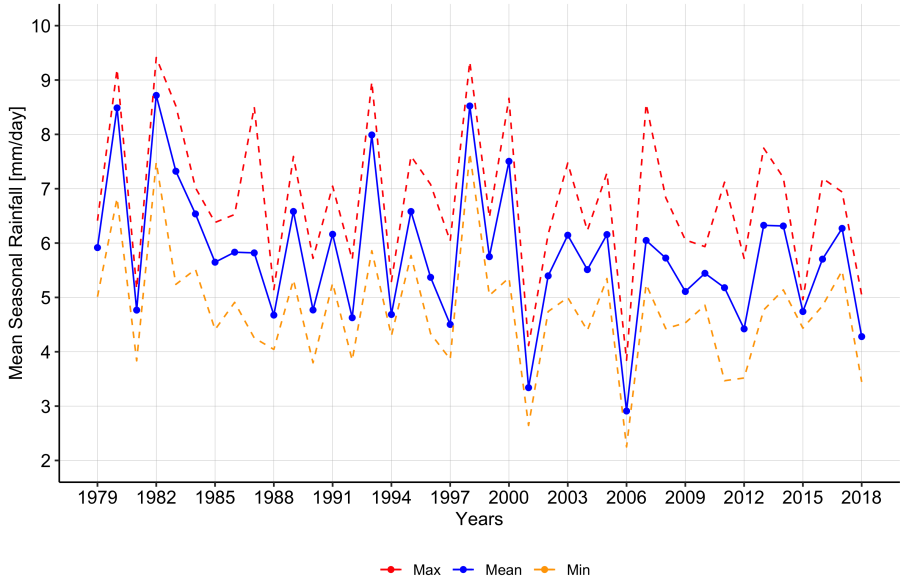

Figure 5.17: Average seasonal mean rainfall (MSR) over the study area from May to August 1979 to 2018 over Wanzhou (blue solid line), with maximum MSR in the study area (red dashed line), and the minimum MSR (yellow dashed line)

Figure 5.17 depicts the temporal variation of the MSR over the study area. The spatial mean is depicted in blue, while the red and yellow dashed lines represent the spatial maximum and minimum. A significant spatial variation of MSR can be observed for certain periods within the study area, based on the deviation based on the temporal trend of the envelope. An expanded width of the envelope from the spatial mean is observed between the years 1985 and 1987, 2002 and 2004 and consistently from 2007 until 2013.

While Figure 5.18 presents the spatial variation between minima and maxima on a temporal scale, it depicts the variation between extremes while essentially comparing the spatial mean with two other points found within the study area. Thus, limiting the general observations of the trend in spatial variability in MSR. Therefore, Figure 5.18 depicts standard deviation as error bars for MSR across the study area to obtain more succinct observations on the spatial variability during this period of observation.

Observations derived from Figure 5.17 suggested increased spatial variability during observation visualized with significant width between the minimum and maximum envelope. The information from Figure Figure 5.18 reveals that in the period identified between 1985 to 1987 in Figure 5.17, the spatial variation in 1987 showed significant spatial standard deviation. In the period 2002 to 2004, 2003 and 2004 were years of

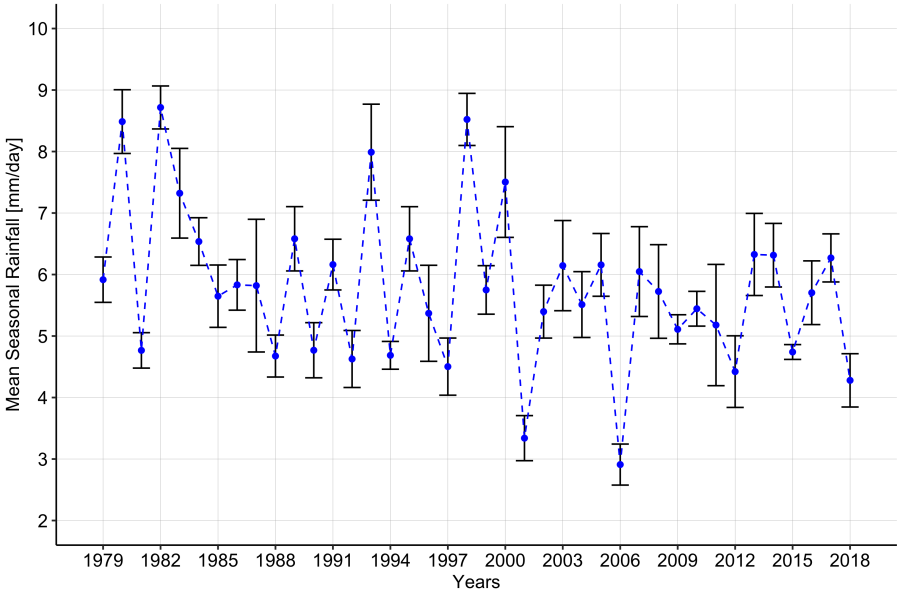

Figure 5.18: Average seasonal mean rainfall (MSR) from May to August 1979 to 2018 over Wanzhou (blue dashed line), with the standard deviation (in error bars).

significant spatial variation. Finally, in the period of 2007 to 2013, a more significant spatial variation of MSR was measured across this observation period when compared to the other periods taken into consideration. During this period, a significant spatial variability is suggested in the year 2011. Additionally, the years 1993 and 2000 with higher spatial means, depicted in Figure 5.17 which means drawing nearer to the maximum MSR lines also are periods with higher spatial variability, as suggested by the standard deviation measurement.

This analysis suggests that changing conditions in the catchment and the interactions with the atmospheric system have increased the variation in mean seasonal rainfall between May to August. Therefore, providing strong evidence against establishing a one reference scenario MSR value to represent the entire study area. The results of this analysis suggest that establishing a MSR value for each pixel, can better account for the spatial variability observed over the 40-year duration of the CMFD dataset.

The MSR values presented in this section were derived from the mean monthly rainfall for the months of May-August. Thus, in order to understand and derive a spatially varying MSR value to represent a reference scenario and account for the variability in rainfall that was observed in across the study area, the spatial distribution of the mean monthly rainfall within the seasonal period as well as the coefficient of variation of each month was analyzed.

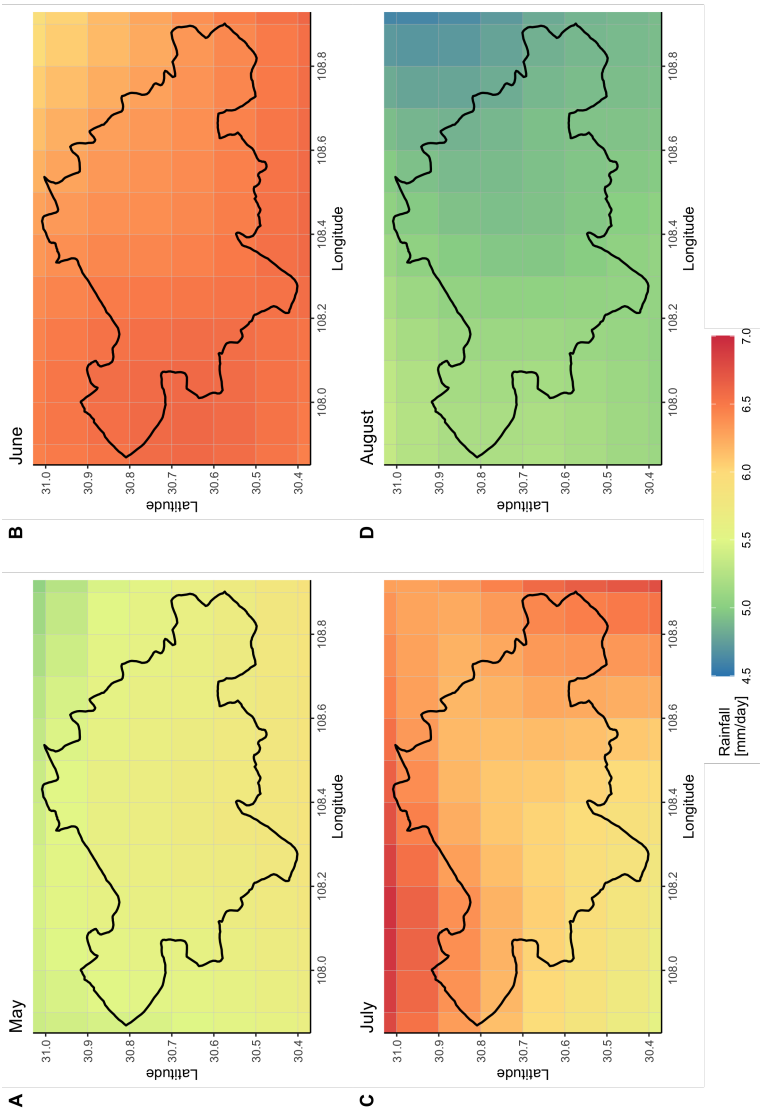

Figure 5.19: Mean monthly rainfall (MMR) showing the average MMR value derived from the period of 1979-2018 for the months of May (A), June (B), July (C), and August (D).

The MMR for May to August are individually presented in Figure Figure 5.19. The MMR for each month was computed by taking the monthly MMR from 1979-2018. Thus, the MMR in Figure 5.19 represents the average daily rainfall for the month considered within this 40-year observation period.

The MMR in May is between 5-6 mm/day, no apparent spatial variation especially within the study area. June shows a range of MMR values between 5.5 mm/day and 6.5 mm/day with a mild decreasing pattern of rainfall diagonally from the northwest to the southwest. The range of daily rainfall values in July are between 5.5 and 7.0 mm/day. The concentration of the highest daily rainfall values in July are observed in the northeast corner of the plots, and outside of the study area.

Within the study area, a diagonally increasing pattern of MMR is observed from the southwest to the northeast corners. There is more spatial variability in July, as compared to June and May with the larger magnitude rainfall areas observed in the northwest and southeast corners. The MMR in August appears to have the lowest range of values being between 4.5 mm/day to 5.5 mm/day. There is a similar pattern of increase in rainfall magnitude with that observed in June, daily rainfall increasing from northeast to southwest, except for an observable area of increased magnitude in the northwest corner of the study area. Based on Figure 5.19, June was observed to have the highest distribution of daily rainfall values across all 4 months within the study area.

The analysis ofFigure 5.19 depicts the spatial patterns of MMR in each month. A further analysis into the temporal variation of the monthly means was conducted through the calculation of a coefficient of variation for each pixel. The temporal insight derived from the coefficient of variation for the MMR of each month is spatially presented in Figure 5.20.

The observed temporal variation in the monthly means presented in Figure 5.20, reveals that significant variation can be expected from the means derived for July and August, compared to those derived from May and June. The highest variation is expected for July, where the southwest corner of the area of interest shows a coefficient of variation between 0.7 and 0.8. This indicates that deviation from the mean monthly rainfall within the 40-year observation period can be 70-80% higher for some years.

The relatively low coefficient of variation in May and June is 0.4, and the visualization in Figure 5.20 indicates that no significant spatial variation is observed. The spatio-temporal analysis of magnitude, pattern and variation of each individual month provides insight on the rainfall characteristics of each month and the potential uncertainty of monthly components when representing MMR on a seasonal time scale.

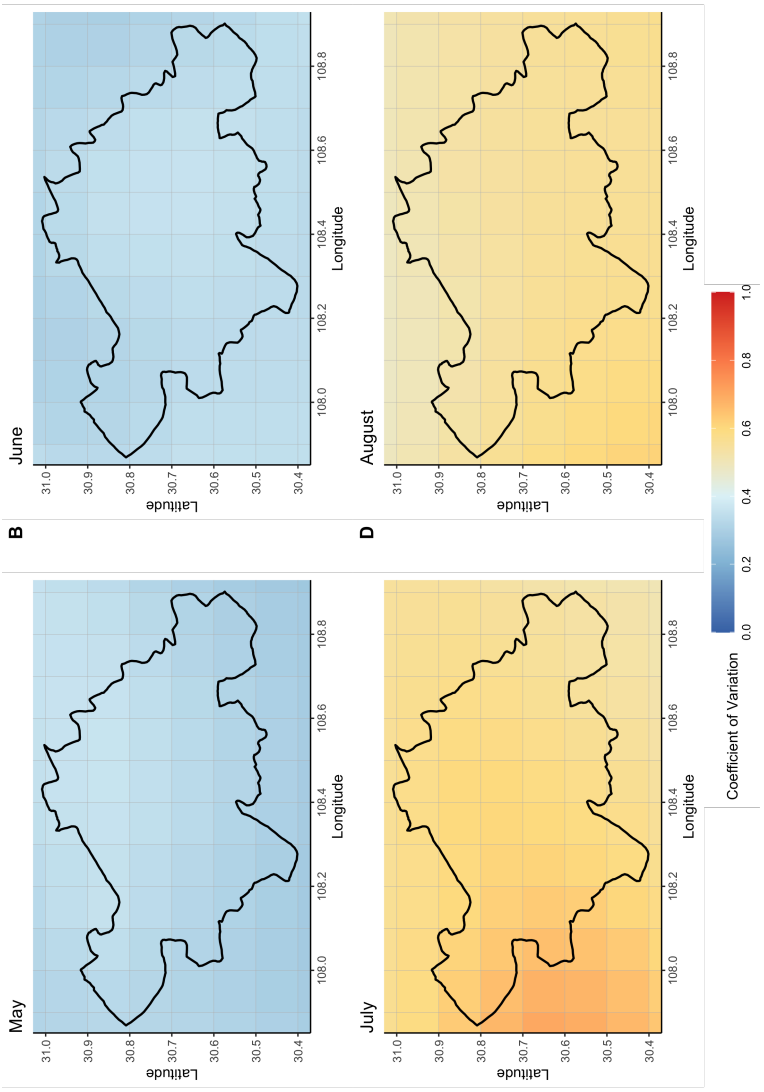

Figure 5.20: Coefficients of variation in mean monthly rainfall derived over the period of 1979 to 2018 for the months of May (A), June (B), July (C), and August (D).

5.2.2 Analysis of the Mean Seasonal Rainfall Reference Scenario

In order to meet the objective of establishing a reference scenario to describe the antecedent rainfall for the landslide season of June to August, the MSR was computed by taking the MMR for the months of May to August for the years 1979 to 2018. Figure 5.21 presents the MSR that represents the reference scenario for antecedent rainfall. The range of MMR magnitudes are between 5.4 mm/day and 6.0 mm/day in the area of interest, with the study area having a range of 5.6 mm/day to 5.9 mm/day. The spatial pattern of rainfall follows a combination of spatial patterns observed in the analysis of the individual month's MMR.

The comparison between the MSR and the monthly derived daily rainfall reveal that on the northeast to southwest diagonal of the area of interest there is an evident increase towards the center of the study area. Meanwhile, the northwest to southeast diagonal of the study area showed an increase in MSR magnitude away from the center. Similar to the spatial pattern of increase observed for July in Figure 5.19, the northwest and southeast corners of the study area contain the magnitudes in the higher range of MSR values. The northeast and southeast corners on the other hand follow the spatial patterns of increase observed in May and August, where the magnitude of MSR values increase diagonally towards the center of the study area.

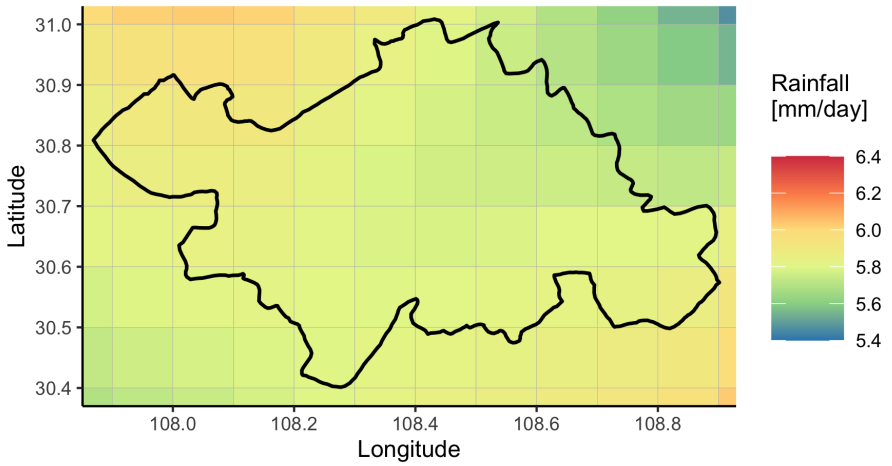

Figure 5.21: Reference scenario derived from mean seasonal rainfall derived from May to August over the period of 1979 to 2018.

The calculation of a coefficient of variation was employed in the analysis of MSR to account for the temporal uncertainty in deriving this value over the time period of 1979-2018. Figure 5.22 presents the spatial characteristics of the temporal variation in MMR derived on a seasonal time scale. The range of variation is between 0.2 and 0.3, suggesting lower temporal variability in MSR as compared to that of monthly derived daily rainfall, with coefficients extending until 0.8 for the months of July and August. Furthermore, the variation along the northwest to southeast diagonal within the study area was observed to increase towards the center. An increase in variation was observed along the southwest to northeast diagonal.

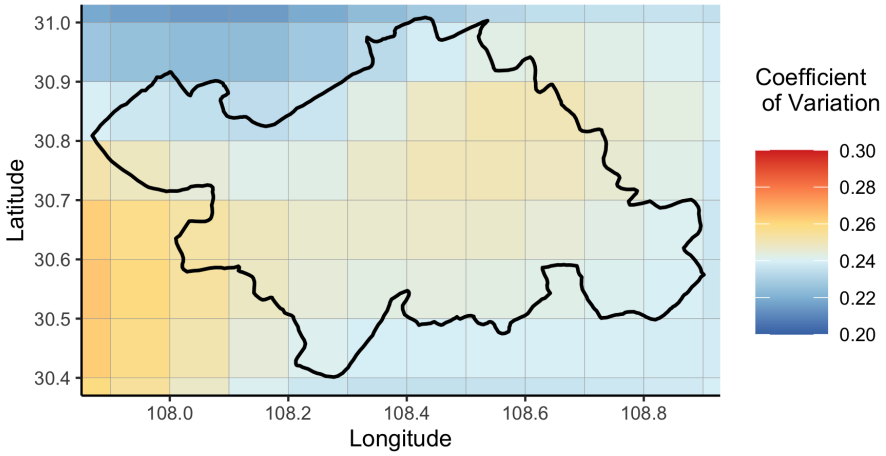

Figure 5.22: Coefficient of variation measuring the temporal variation in mean seasonal rainfall from 1979 to 2018.

An analysis of the relative deviation between the seasonal mean and each monthly mean was conducted to quantify the ability of the MSR as the reference scenario to represent each monthly MMR over the 40-year period of observation. The relative deviation of the was taken by the difference between the monthly MMR and the MSR over the MSR and is reported in percentage. The spatial distribution of this analysis for each month is depicted in Figure 5.23. The range of relative deviation of the MSR is between -20% and +20%. The most significant deviations within the study area are observed in June and August. The MSR underestimates the MMR in June by 5% to 15%, while overestimating the mean of August by 5% to 20%. The spatial characteristics of the relative deviation for these two months show mild difference, with August showing

a homogeneous spatial pattern associated with taking the mean over higher value MMR months. The spatial pattern of deviation in June showed an increased overestimation from northeast to southwest of the area of interest. The MSR manages to better represent the monthly MMR of May and July. A spatial pattern of underestimation is observed to increase from the southwest corner of the study area in July. An overestimation is observed in May with a relative decrease from the northwest study area corner.

Until this point, the analysis of the ability of the reference scenario derived from the MSR has focused on spatial-temporal characteristics to understand uncertainty in representing monthly characteristics through a seasonal summary statistic. A final criterion to investigate if the MSR reference scenario was able to capture the spatial distribution of MMR was performed to strengthen the insight on the varying rainfall behavior from observed spatial patterns.

The empirical cumulative distribution function (CDF) was estimated for the MSR and the MMR of each month included in the season. The results of the comparison of CDFs compared through scaled daily rainfall values on the x-axis is shown in Figure 5.24. This figure depicts the spatial distribution of MMR values, and depicts the deviation of MSR from that of June. This indicates that towards the tail of the distribution, there are higher MMR values across the area of interest in June that are not captured by the MSR. Although this is the case for June, the CDF of the MSR closely follows those of the other months.

A follow through analysis of the spatial distribution of MMR values between the MSR and each individual month was conducted through the comparison of density distribution, shown in Figure 5.24. A comparison of the estimated density distributions and the estimated mean values on a scaled MMR x-axis reveals that the distributions of May, June and August show more left skew than the MSR and that of July. Although the distributions show a variation in skew, when compared to the MSR, the spatial means of all May, June and August show close resemblance in location on the scaled axis, when compared to the MSR. These results suggest the distributions may be skewed the left-side tail is heavier for the aforementioned months, and reflects on limited ability of the MSR to capture higher magnitude MMR values, but supports its ability to capture lower magnitude MMR values spatially distributed across the area of interest. There is a noticeable difference in mean between the MSR and the month of July, this reflects the limitations of the MSR reflected in the underestimation of July MMR values across the area of interest. The density distribution and mean location analysis of the monthly MMR values versus the MSR values elaborates on the limitation of the MSR to spatially capture the MMR conditions of each month, as shown in the analysis of the variation illustrated in Figure 5.22.

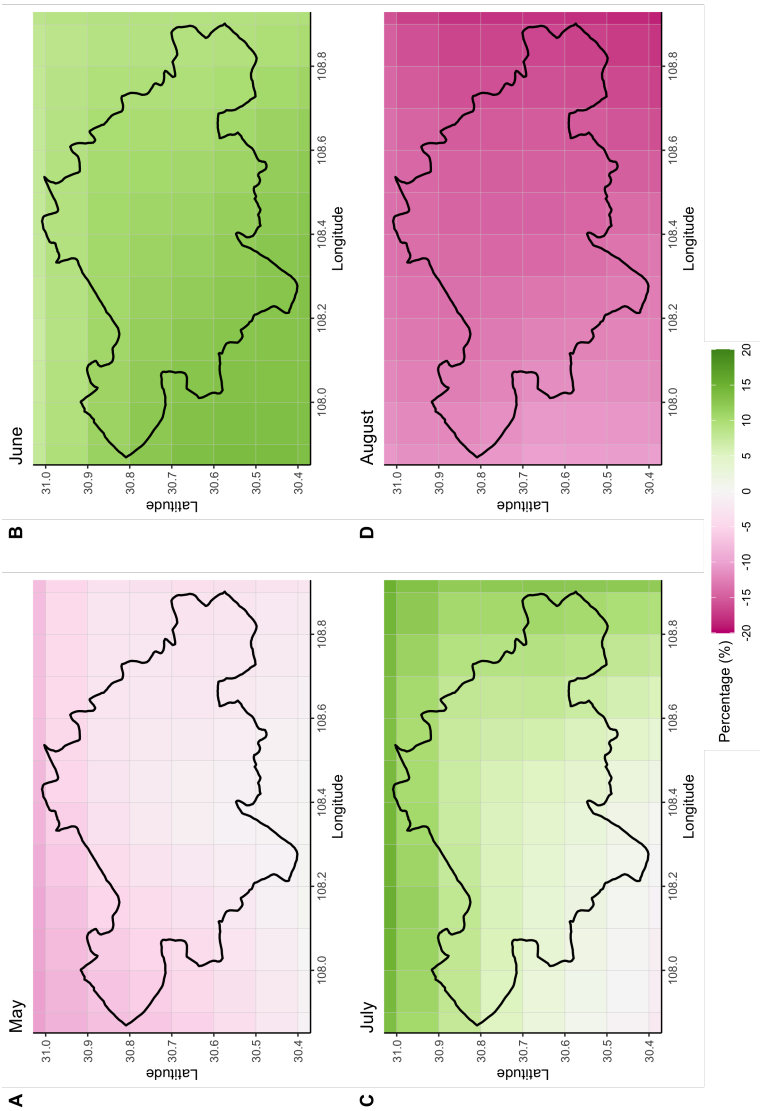

Figure 5.23: Relative deviation of the reference scenario mean seasonal rainfall from the mean monthly rainfall for the months of May (A), June (B), July (C), and August (D).

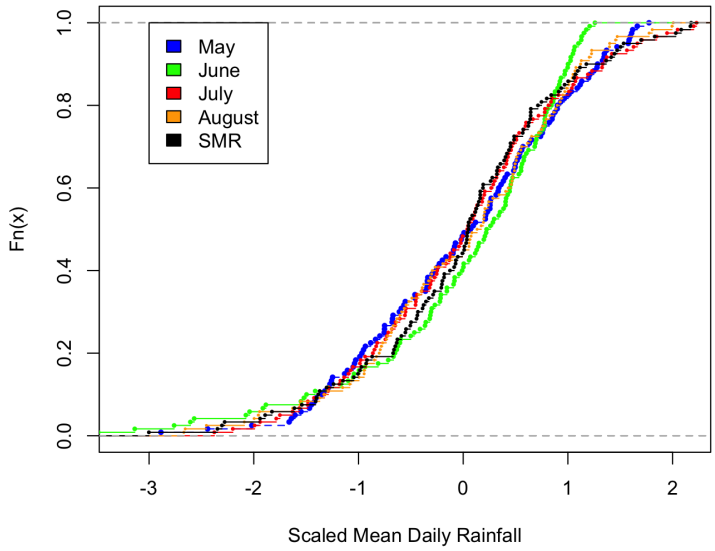

Figure 5.24: Cumulative distribution functions ($F(x)$)derived from mean monthly rainfall values from 1979 to 2018 for May (blue), June (green), July (pink), August (orange), and the mean seasonal rainfall (black).

5.2.3 An Analysis of Extreme Daily Rainfall over Wanzhou

The second rainfall triggering mechanism of shallow landslides that was considered in this study is the extreme daily rainfall (EDR). The EDR is defined by the accumulated single-day rainfall that affects shallow landslide susceptibility by introducing significant vertical flow through the soil column, and effectively decreasing the stabilizing forces. It is therefore necessary to account for the destabilizing source of this process on the extreme distribution of precipitation in the study area in order to understand the imminent risks extreme daily rainfall may have on shallow landslide susceptibility.

This section focuses on defining the extreme daily rainfall over the study area, based on the CMFD data set from 1979 to 2018, and understanding the characteristics distribution of extreme daily rainfall in order to assess an applicable frequency distribution model. The results for this section was to and provide a set of extreme daily rainfall value to fit a frequency distribution model to calculate rainfall value corresponding to return periods that will serve as the reference scenario for event rainfall.

The definition of extreme daily rainfall in this research project followed the Block Maxima Approach, taking the monthly maxima for the summer season during the

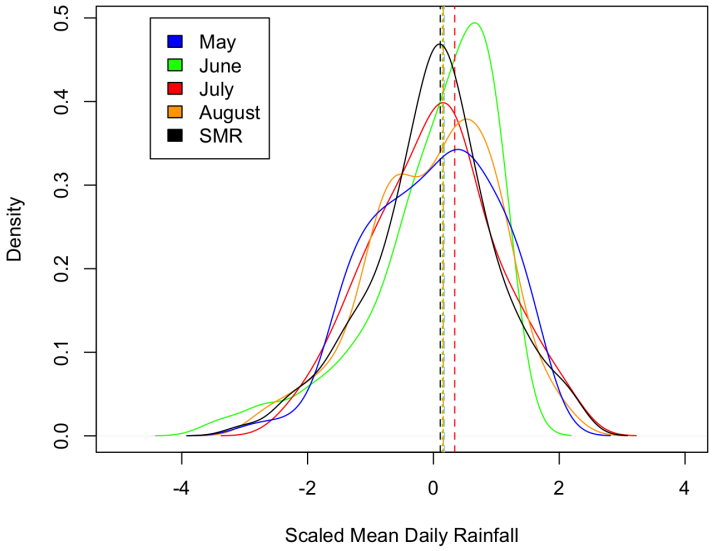

Figure 5.25: Density distribution curves derived from mean monthly rainfall values from 1979 to 2018 for May (blue), June (green), July (pink), August (orange), and the MSR (black).

period of June to August. The results of this was a time series of the EDR for each CMFD pixel in the area of interest. A map of the maximum EDR extracted from each pixel in the area of interest based on the monthly maxima approach is presented in Figure 5.26. The spatial distribution of the maximum extreme daily rainfall across the study area for the summer season reveals that from the center to north of the study area, the EDR values are between 180 mm/day to 210 mm/day. In order to quantify the significance of these values, the relative deviation to the mean maximum EDR across the area of interest was calculated and presented in Figure 5.26. The calculation of relative deviation from the spatial mean reveals that the concentration of extreme daily rainfall in center to north areas is 10% to 30% higher than the maximum EDR values spatially distributed across the area of interest.

The minimum EDR values were plotted in Figure 5.27 to assess the range of EDR values based on monthly maxima. The range of values are between 2 and 14 mm/day indicating that there were summer season months with significantly low amounts of precipitation between 1979-2018. This is possible due to the low amount of precipitation experienced in the years 2001 and 2006 with seasonal MMR was barely above 3 mm/day, as depicted in Figure 5.17. The spatial distribution of minimum EDR values show no

distinct spatial pattern within the study area, apart from the influence of higher values across the northern boundaries of the area of interest. Furthermore, the calculation of relative deviation from the spatial was conducted to highlight the range of minimum EDR values. The range relative deviation from the spatial mean of minimum EDR values is 100% on both ends of the spectrum. This is significantly larger than the 30% relative deviation range observed in the maximum EDR values.

The contrast in relative deviation between maximum and minimum EDR values over the 40-year data period indicates significant spatial variability arises from the change in atmospheric dynamics between wet years with significantly large magnitudes of extreme daily rainfall, and dry years with significantly low magnitudes of rainfall. The analysis of maximum and minimum EDR values gave insight on the contrasting dynamics between wet years and dry years from the perspective of monthly maxima in defining extreme daily rainfall.

The distribution of the EDR was also assessed using a skewness coefficient to understand the characteristics of the extreme values extracted, and to give insight in determining if an extreme value frequency distribution function was appropriate. The summary spatial distribution of skewness coefficients is presented as a box plot in Figure 5.28 The minimum skewness coefficient in the area of interest is 1.03 and the maximum is 2.31, with a spatial mean of 1.65. The range of skewness coefficients suggest that the data is highly skewed. The results of this analysis suggest that utilizing extreme value frequency distribution models is appropriate to modeling the statistical distribution of EDR values across the area of interest.

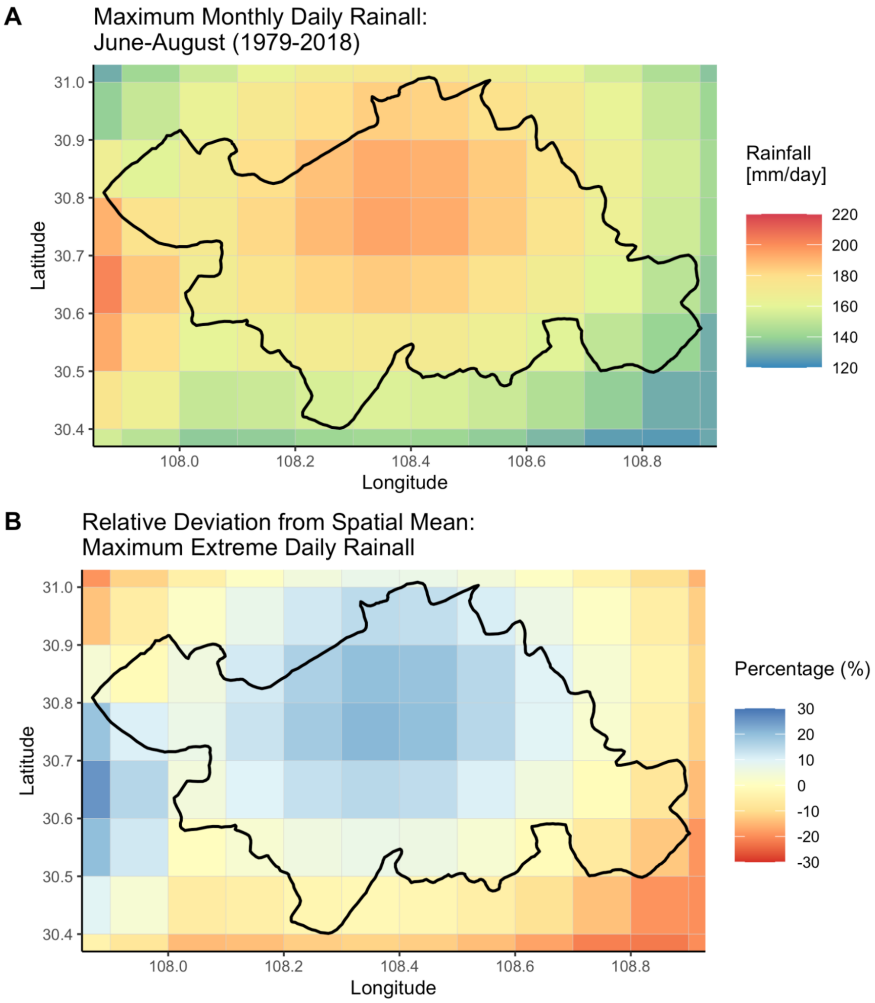

Figure 5.26: Maximum extreme daily rainfall (A) derived from the monthly block maxima approach, and the relative deviation of the maxima in each grid cell from the spatial mean of maximum daily rainfall (B) from the period of June to August 1979 to 2018.

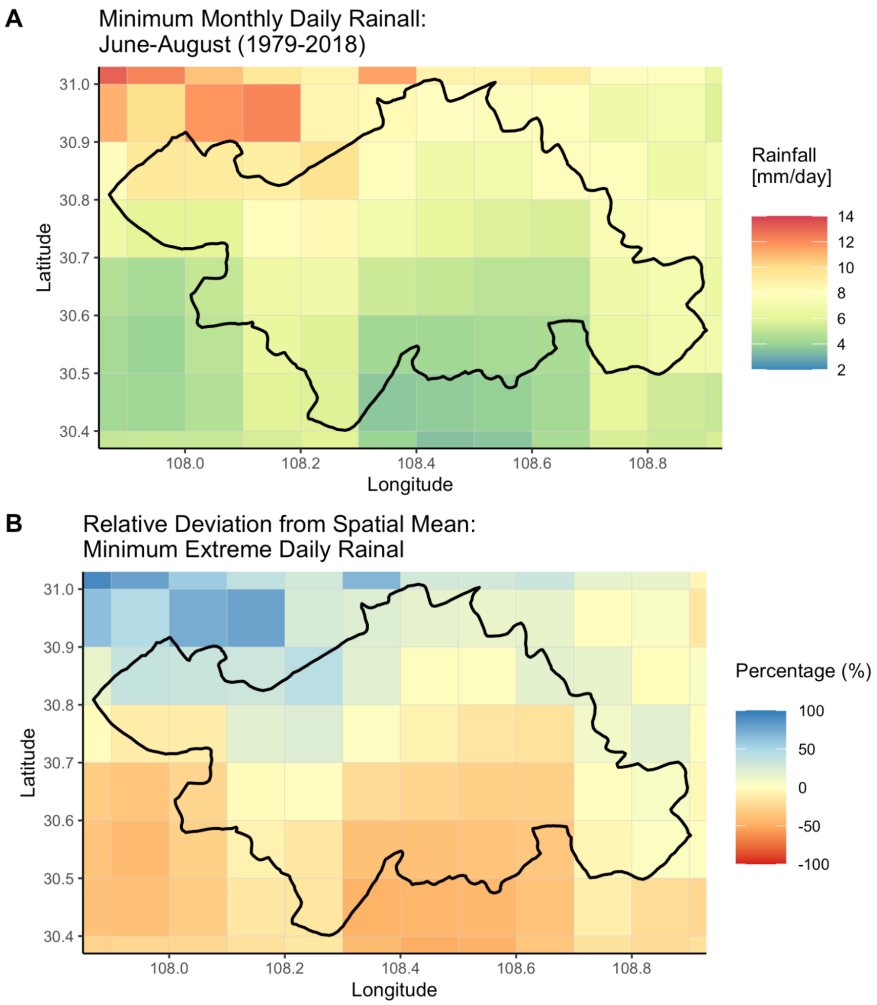

Figure 5.27: Minimum extreme daily rainfall (A) derived from the monthly block maxima approach, and the relative deviation of the minima each grid cell from the spatial mean of extreme daily rainfall representing relatively dry years (B) from the period of June to August 1979-2018.

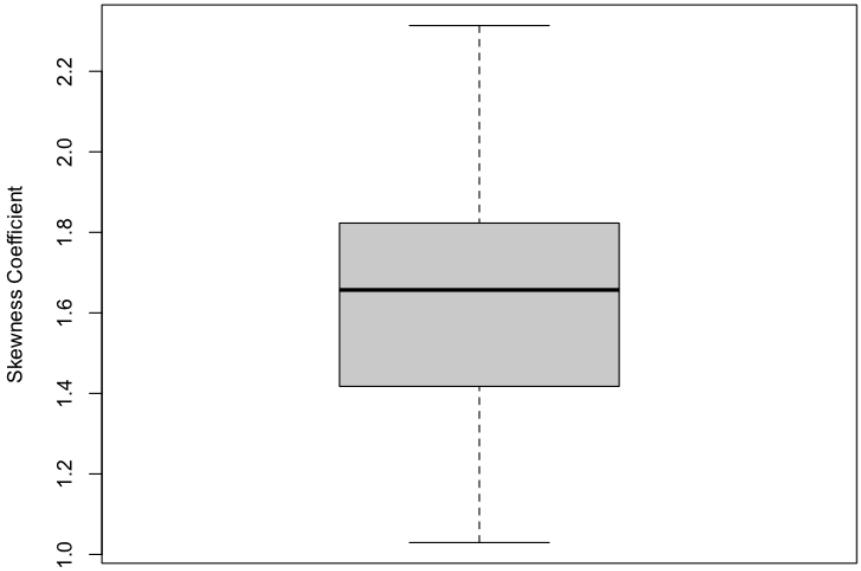

Figure 5.28: Skewness coefficient of the extreme daily rainfall of each grid cell within the study area for 1979 to 2018.

Frequency Distribution Modeling of Extreme Daily Rainfall

The methodology for modeling the frequency distribution of extreme daily rainfall was described in Section 4.4. The Gumbel distribution model was selected for this research project in order to build on previous knowledge and application of this frequency distribution model in the Wanzhou County area by Xiao *et al.* [21]. The summary of Gumbel Fit parameters is presented in Table 5.2. A Gumbel fit was estimated for each CMFD pixel within the area of interest, resulting in 120 frequency distribution models. The specifications of the minimum, mean and maximum Gumbel fit parameters are also presented in Table 5.2. The spatial variability observed in the analysis of EDR extracted by block maxima approach and the spatial variability of the minimum and maximum EDR results are reflected in the variability of the tabulated Gumbel Fit parameters.

The Goodness-of-fit statistical tests were performed to validate the results of the Gumbel frequency distribution models. Each test is discussed in Section 4.4. The

Table 5.2: Summary of minimum, mean and maximum Gumbel fit parameters.

Gumbel Fit Parameters	Minimum	Mean	Maximum
Scale α	14.6	17.3	21.7
Beta β	29.4	32.9	36.9
Mean μ	30.3	33.9	38.1
Standard Deviation σ	18.8	22.2	27.8

confidence interval applied in this test was 95%. Therefore, the condition of the P-value for each test statistic for each test run was that it would be greater than or equal to 0.05. Also tabulated in Table 5.3 are the results of each test, the correspondent statistic and the p-value, showing the minimum, maximum and mean. The results of the Gumbel distribution fitting to the EDR data across the area of interest provided an adequate model of the frequency distribution.

Table 5.3: Summary Goodness-of-fit test statistics with p-values (in parenthesis).

Goodness-of-fit Test	Minimum	Mean	Maximum
KS Test	0.029 (0.39)	0.052 (0.86)	0.082 (1.00)
AD Test	0.145 (0.53)	0.318 (0.91)	0.730 (1.00)
CVM Test	0.015 (0.44)	0.046 (0.89)	0.136 (1.00)

The resulting parameters of the validated Gumbel distributions were then utilized to estimate daily rainfall corresponding to different return periods, given by Section 4.4. The return period curve was then plotted for each distribution for rainfall corresponding to EDR with return periods between 2 years and 200 years. The return period curves for all the distributions fit within the area of influence are plotted in Figure 5.29. The return period curve returning the maximum EDR is plotted in green, while the curve describing the minimum EDR is plotted in red. The individual curves modeled after data from individual time series across the area are plotted in grey.

The spatial variability of EDR for different return periods is observed by the density of the grey plotted Gumbel fit lines between the red lower limit and the green upper limit. The divergence of estimation of rainfall as the return period increases also exponentially increases. The spatial variability observed in the return period estimated rainfall reflects the variability of extreme rainfall in the observations based on the monthly maxima.

These results highlight a significant application of gridded precipitation datasets with high spatial resolution to address the characteristics of spatial variability in extreme rainfall. The extreme daily rainfall at higher return periods in Figure 5.29 have a significantly lower values than the maximum extreme daily rainfalls presented in

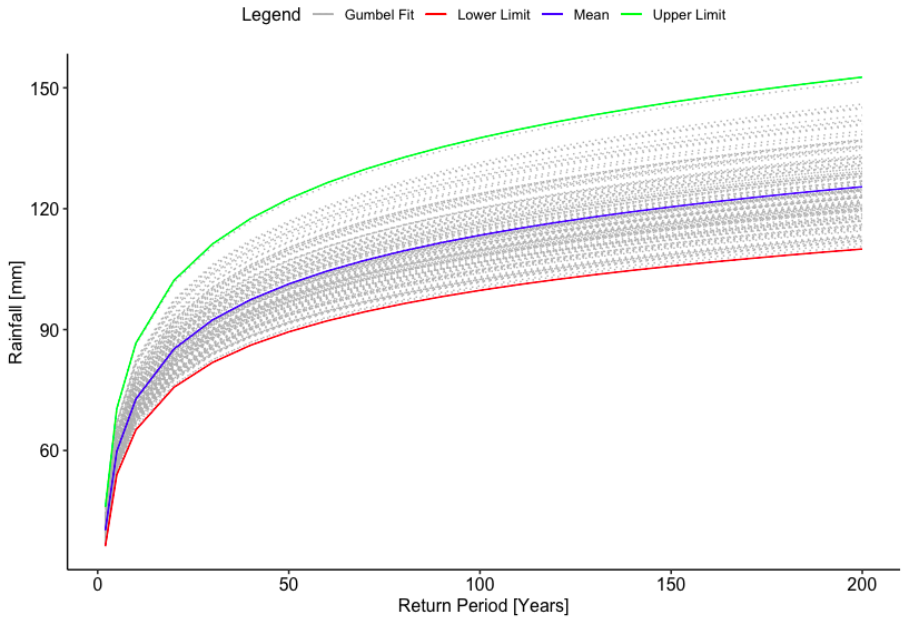

Figure 5.29: Return period curves derived from Gumbel fittings in all pixels across the study area (grey lines) with the relationship curves for the mean extreme daily rainfall (blue), the maximum (green), and the minimum (red).

Figure 5.26. This is derived from the tendency of the Gumbel distribution to yield the the smallest possible rainfall value in comparison to other extreme value distributions [80].

5.2.4 An Analysis of the Extreme Daily Rainfall Reference Scenario

The objective of modeling extreme daily rainfall in this research project was to establish a spatially varying reference scenario for extreme daily rainfall at different return periods. The significant results of this methodology are presented in this section. The reference scenarios to assess the future of shallow landslide susceptibility was created to give spatial representation to the rainfall corresponding to return periods of 10, 20, 50 and 100 years.

The spatial distribution of EDR corresponding to different return periods using the Gumbel distribution parameters was utilized to assess the spatial characteristics of EDR corresponding to different probabilities of occurrence across the area of interest. The spatial distribution of EDR for different return periods of 10, 20 , 50 and 100 years are mapped in Figure 5.30.

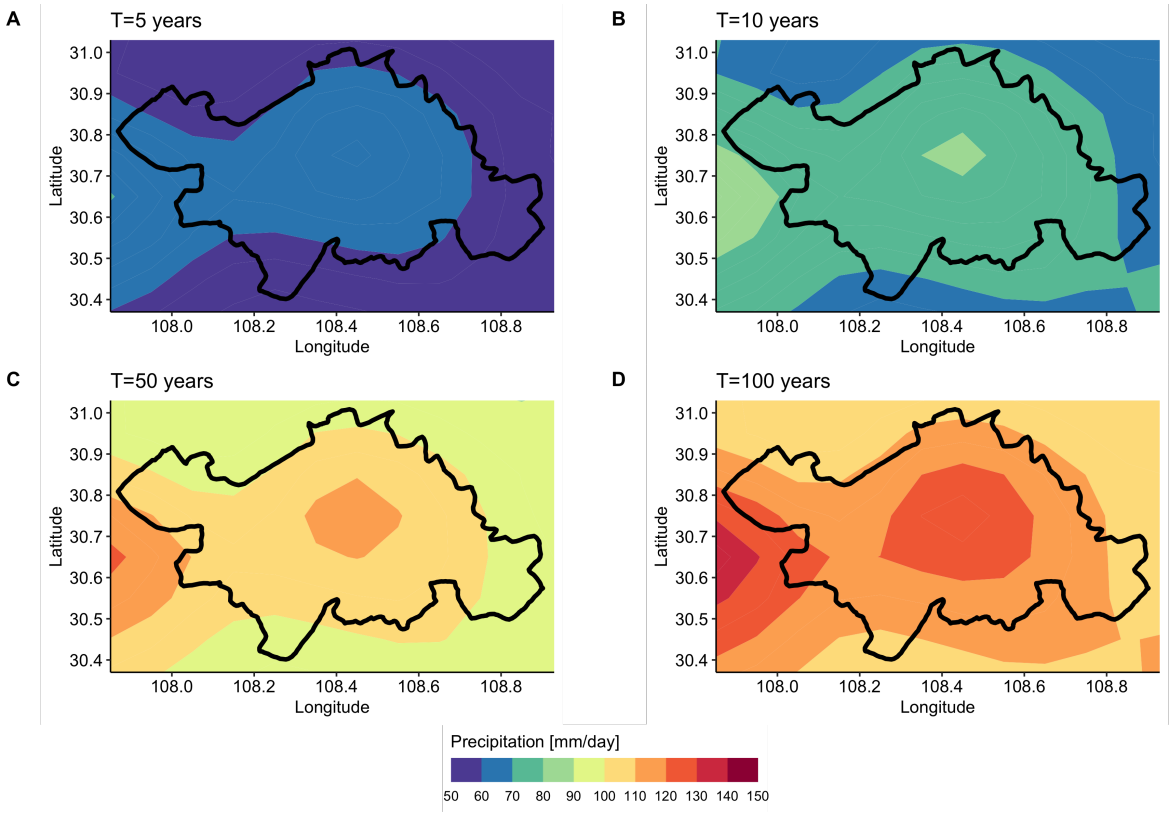

Figure 5.30: Comparison of the spatial distribution in extreme daily rainfall corresponding to return periods of 10, 20, 50 and 100 years (left to right, top to bottom) calculated through the Gumbel fittings.

A significant observation of the rainfall return levels in Figure 5.30 an increasing side of the large magnitude EDR at the center of the catchment. This clustering of EDR from the center of the catchment grows in an area for EDR between 10-year to 20-year return periods. The differences in magnitude between the areas visualized in Figure 5.30 are defined by differences of 10 mm/day. This area of clustered EDR proceeds to decrease from 20-year to 50-year EDR estimates, and alternatively increasing to an area even larger than the 20-year return level cluster area for 100-year return levels. The area in the center of the study area is of concern, suggesting with a 100-year return period, a growing area exposed to risk of 120 mm to 130 mm rainfall magnitudes emerges. The spatial pattern for this cluster of EDR was observed in the analysis of the maximum EDR values Figure 5.30, this area was concentrated in the center to northeast of the study area.

Although Figure 5.30 identifies a growing area of risk in the center of the study area, the west border of the area of interest also reveals a significant trend of increasing EDR with return levels greater than those modeled within the study area. The magnitudes of these EDR values are between 130 mm to 150 mm and can represent significant triggering-rainfall conditions that could induce shallow landslides.

This risk area lies within a valley between mountain ranges reaching peak heights of 1640 m on both sides, shown in Figure 1.1. The location of increased precipitation suggests an orographic enhancement of precipitation could be driving increased EDR magnitudes during the summer season.

These estimates are outside of the boundaries of the study area, and the spatial uncertainty that accompanies the the CMFD dataset spatial interpolation, integration of satellite estimates and reanalysis results prompts the recommendation of the possibility that the EDR on the western border potentially influences to instability stability of the western region of the study area.

5.3 Part 3: Projected Summer Rainfall Under Climate Change

This section of the results presents the implementation of Section 4.5 to derive projections and conduct a climate change analysis. A model bias correction of the Regional climate model outputs through the Quantile Delta Mapping (QDM) method was conducted. The climate signals of the daily rainfall and extreme daily rainfall were separately corrected with transfer functions derived through an empirical CDF, and a parametric Gumbel fit CDF, respectively. A multi-model ensemble of 4 climate model outputs was considered. This combination comprised of the HadGEM-ES and MPI-ESM Global climate models (GCM) providing the boundary layer conditions for dynamic downscaling by the RegCM4 and REMO Regional climate models (RCM). The

spatio-temporal projections and uncertainties derived from the mean ensemble were analyzed for the scenarios defined by Table 4.2.

5.3.1 Validation of Bias Correction by Quantile Delta Methods

Bias correction was applied to the climate model outputs to address the systematic errors present in the results. A bias correction on all ensemble member outputs were performed separately for daily precipitation and extreme daily rainfall, as described in Section 4.5.2. The cross-validation procedure was performed to assess the performance of the empirical QDM on daily rainfall results within the reference period of 1979-2018, as described in Section 4.5.3. A validation procedure for the bias-corrected extreme daily rainfall (EDR) was performed, following Section 4.5.4, and compared the observed EDR over the reference period.

Cross-Validation of Bias-corrected Daily Rainfall

The results of the bias correction methodology for daily rainfall, described in Section 4.5.2, was applied to the historical model results from 1979-2005 combined with the model projections from 2005-2018 of each ensemble member. The bias-corrected results over this combined period representing the historical and projection outputs were then compared to the CMFD observations through a cross-validation procedure. This section presents the results of the cross-validation for bias-corrected RCM outputs for daily rainfall, following the methodology in Section 4.5.3. Figure 4.5 provides an illustrative box plot comparison between the cross-validation performance of the bias-correction for daily rainfall as measured by the mean average error (MAE). This measure for cross-validation was employed to measure the accuracy of the bias-correction.

The MAE performance of the bias-corrected ensemble members across the study area ranges between 8.6 mm/day to 8.8 mm/day. The interquartile ranges of the MAE for all four ensemble members showed little variation with ranges between 8.5 mm/day to 8.9 mm/day.

Furthermore, the cross-validation performance measured by root-mean squared error (RMSE) was also calculated and is shown in Figure 5.32. The RMSE gives insight into the average magnitude of error and penalizes larger deviations with relatively higher weight The range of mean RMSE across all ensemble members is from 15.5 mm/day to 16 mm/day. The interquartile ranges are from 15 mm/day to 16.5 mm/day. The minimum box plot whiskers are equivalent across the ensemble with values below 14.5 mm/day, the maximum whiskers for the REMO RCM results are observably larger than the RegCM4 maxima. Although this may indicate better performance of the RegCM4 members on the extreme, the interquartile range of the REMO RCM models is evidently smaller. The analysis of MAE and RMSE performance in the cross-validation

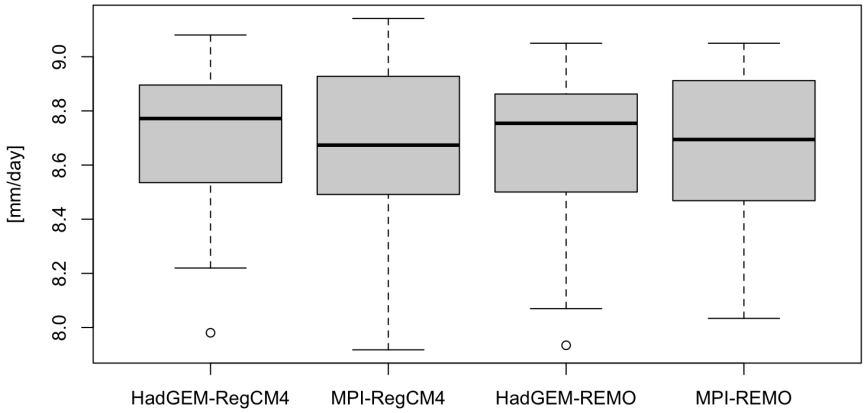

Figure 5.31: Box plot comparison of cross-validation performance of the daily rainfall bias correction measured by mean average error (MAE) for each grid point results of the four GCM-RCM ensemble member combinations.

presented in Figure 5.31 and Figure 5.32 provided to no conclusive evidence suggesting one GCM-RCM combination outperforms the other.

Validation of Bias-corrected Extreme Daily Rainfall

Extreme daily rainfall bias correction, described by the methodology in Section 4.5.2 was performed for all ensemble member outputs over a period incorporating the the historical model results from 1979-2005 combined with the model projections from 2005-2018 of each ensemble member. The parametric quantile mapping bias correction was performed with a Gumbel distribution fit, given in Section 4.4 to the data to yield each ensemble member's output for extreme rainfall. The reference period observations from the CMFD dataset from 1979-2018 ordered and used to validate the ordered and bias-corrected extreme rainfall results of each ensemble member, as described in Section 4.5.4.

The ordered statistics of the datasets were utilized to measure the performance of the bias-corrected historical ensemble member results during reference period. The performance was first measured using the Mean Absolute Error (MAE) to give insight into the uncertainty in the corrected accuracy. The comparison of the MAE performance is presented in Figure 5.33. The range MAE for the EDR bias correction varies from 4

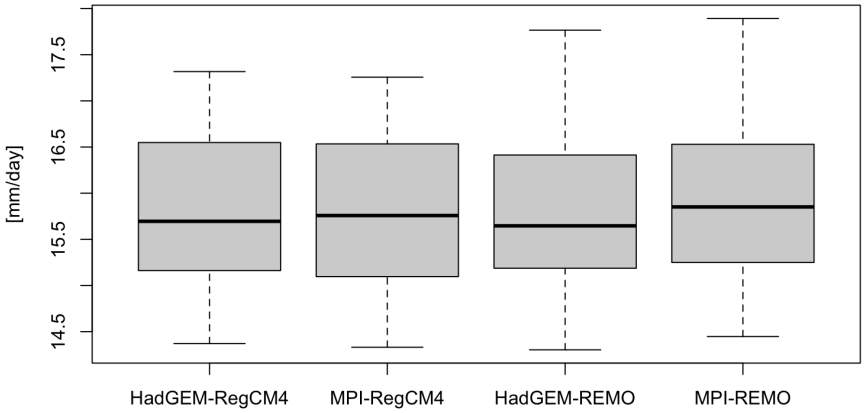

Figure 5.32: Box plot comparison of cross-validation performance of the daily rainfall bias correction measured by root-mean squared error (RMSE) for each grid point results of the four GCM-RCM ensemble member combinations.

mm/day to 5.5 mm/day. The performance of the MPI RCM results is evidently better than the HadGEM RCM outputs in Figure 5.33. The interquartile range of MPI-driven outputs are between 2 mm/day and 4 mm/day with maximum error measured reaching 5 mm/day. The performance of the HadGEM bias-corrected outputs are between 4 mm/day to 6 mm/day with a maximum 7.5 mm/day. This comparison of MAE performance validated against the reference period observations suggest that the boundary conditions provided by the MPI GCM provide a more accurate perspective on the extreme daily rainfall.

Similar to the analysis of performance in the daily rainfall bias correction results, the bias-corrected EDR performance was also measured through root-mean squared error (RMSE). The results of the performance validation of the bias-corrected results versus the observations during the reference period are presented in Figure 5.34. The results of the comparison of RMSE on the ordered statistics suggest that the MPI-driven bias corrections outperform the HadGEM-driven outputs. This is supported by the interquartile range of the MPI models being between 4 mm/ day to 8 mm/day, compared to the HadGEM outputs having a range of 5 mm/day to 10 mm/day. Furthermore, the outliers beyond the maximum whiskers are significantly less and lower in RMSE magnitude for MPI-driven models as compared to HadGEM-driven models. The analysis of RMSE in Figure 5.33 and Figure 5.34 give reasonable evidence to suggest that the

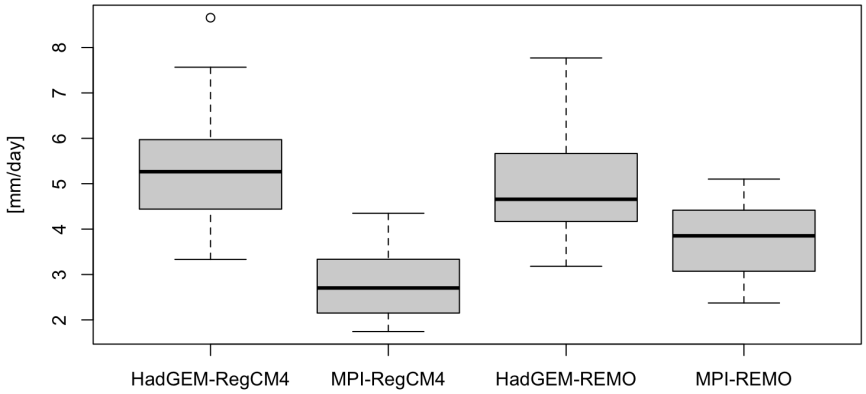

Figure 5.33: Comparison of validation performance of the extreme daily rainfall bias correction measured by mean average error (MAE) for each grid point results of the four GCM-RCM ensemble member combinations.

bias-corrected MPI-driven RCM models perform better than the HadGEM-driven RCM models in capturing extreme daily rainfall.

The performance of the ensemble was initially measured with MAE and RMSE to initially assess the accuracy and magnitude of deviation in capturing EDR observed over the reference period. It was further determined that since the bias-correction for EDR was parametric and performed through quantile mapping correction of fitted Gumbel distribution models on the historical and observed data sets, an assessment of the performance using the Pearson correlation coefficient between the magnitude of the EDR observed and the modeled EDR was necessary to further understand the reliability of each ensemble member. The comparison of the box plots capturing the distribution of Pearson correlation coefficients for each ensemble member across the study area is presented in Figure 5.35 The interquartile ranges of the MPI-driven results are between 0.96 and 0.99, indicating very high correlation between the magnitude of EDR modeled and those observed. The interquartile ranges of the HadGEM-driven models are between 0.93 and 0.98, also indicating good performance in capturing EDR. Although the MPI driven results generally perform better than the HadGEM results, as observed in Figure 5.33 and Figure 5.34, the analysis of Pearson correlation coefficients support the notion that the ensemble member combinations perform adequately in capturing EDR.

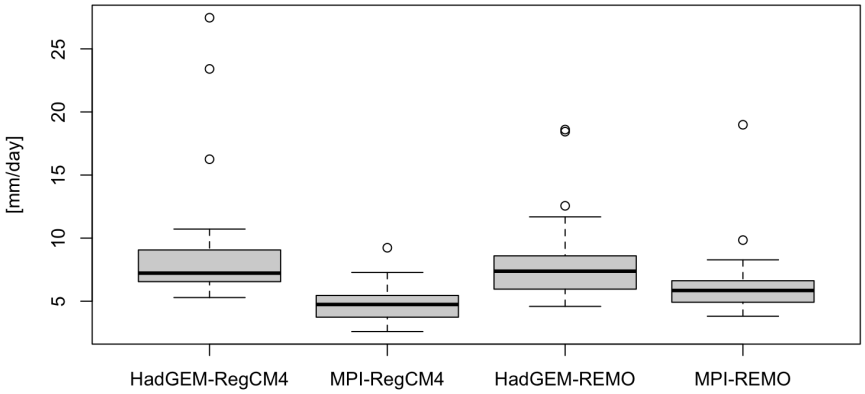

Figure 5.34: Comparison of validation performance of the extreme daily rainfall bias correction measured by root-mean squared error (RMSE) for each grid point results of the four GCM-RCM ensemble member combinations.

The final measure of performance for the Gumbel parametric quantile mapping bias correction methodology of the was performed using a Kolmogorov-Smirnov (KS) Test between the observations and the bias-corrected extreme rainfall outputs. This test is performed to understand if the bias-corrected extreme rainfall distributions could statistically belong to the distribution of the observations over the reference period. The KS Test measures the deviation of the cumulative distribution functions along the vertical, to which a statistical threshold using a confidence interval can be assessed. Similar to the analysis conducted using goodness-of-fit tests in this research project, the confidence interval determined to be acceptable was 95% or results with a p-value greater than 0.05.

Table 5.4: Summary of the Kolmogorov-Smirnov (KS) test between bias-corrected ensemble members with minimum, mean and maximum test statistics and p-values (in parenthesis).

Ensemble Member	Minimum	Mean	Maximum
HadGEM-RCM4	0.07 (0.007)	0.16 (0.142)	0.22 (0.952)
MPI-RegCM4	0.07 (0.024)	0.13 (0.363)	0.19 (0.952)
HadGEM-REMO	0.13 (.001)	0.19 (0.051)	0.25 (0.236)
MPI-REMO	0.05 (0.151)	0.09 (0.659)	0.15 (0.999)

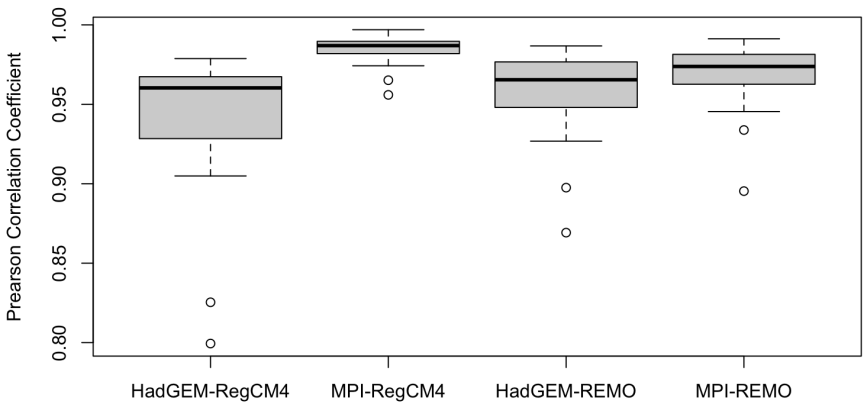

Figure 5.35: Comparison of validation performance of the extreme daily rainfall bias correction measured by Pearson correlation coefficient for each grid point results of the four GCM-RCM ensemble member combinations.

Table 5.4 presents the summary of the KS test conducted to validate the similarity in the cumulative distribution functions between the bias-corrected EDR of the ensemble members versus the CMFD observations. The results of the KS tests stipulate that the bias-corrected extreme rainfall results of the MPI-REMO RCM combination outperforms the other three ensemble members, and that the bias-corrected extreme rainfall can statistically be assumed to belong to the same distribution of the CMFD observations. The range of p-values for the MPI-REMO ensemble member is between 0.141 to 0.999 with all RCM cells passing the KS Test.

In contrast to these results, the HadGEM-REMO combination did not perform as well as the MPI-REMO results with only 10 cells passing the KS test, presented in Table 5.5. An analysis of the RegCM4 results indicate that the MPI-driven results perform better on the KS test with 27 out of 29 passing with a 95% confidence interval, compared to the HadGEM results of 22 out of 29. The results of the KS Test corroborates with analysis of the MAE, RMSE and Pearson correlation coefficient in this section to support the notion that the MPI-driven RCM results perform better than those driven by the HadGEM GCM in capturing EDR.

The performance of the HadGEM-REMO bias correction is derived from main limitation of the proposed QDM bias correction for EDR in the assumption that a Gumbel frequency distribution will remain adequate across the study area. Huang *et al.* [38]

Table 5.5: Summary of the bias-corrected RCM cells passing a Kolmogorov-Smirnov Test and the total number of cells corrected with a $p - value \geq 0.05$

Ensemble Member	Passing the KS Test	RCM Points Tested
HadGEM-RCM4	22	29
MPI-RegCM4	27	29
HadGEM-REMO	10	28
MPI-REMO	28	28

finds that the application of a mixture of distribution to perform as a transfer function for bias correction outperforms a single distribution by allowing for spatial variation of rainfall distributions in different grid cells. The limitation of the implementation of the parametric QDM resulted in biased-corrected estimations by Gumbel frequency distributions to represent the EDR is illustrated in Table 5.5.

5.3.2 Climate Change Projections for Mean Seasonal Rainfall

This section analyzes the influence of climate change based on scenarios of mean seasonal daily rainfall (MSR) projections in the Mid 21st Century (2021-2060) and the Late 21st Century (2061-2100).

The mean ensemble climate change factors (CCF) were derived based on the prescription of Section 4.5.5, and bilinearly interpolated into the CMFD grid. The spatial distribution of the bilinearly interpolated CCF_{MSR} and $CCF_{EDR,T}$ are depicted for both future climate change scenarios taken into consideration in this research project in Figure 5.36. The CCF_{MSR} for the project MSR in the Mid 21st century are between 1 and 1.4. There are two distinct regions identified over the study area, with the western region projecting values for a CCF_{MSR} between 1.0 and 1.2, and values in the eastern region between 1.2 and 1.4.

In the projections for the Late 21st Century, the CCF_{MSR} see an expanded range from 1.2 to 1.8. The increase in values can be identified through three regions. The increase in CCF_{MSR} occurs from west to east, with a narrow band in the southeast of the study area showing values between 1.6 to 1.8.

The uncertainty in the ensemble mean CCF_{MSR} was measured through the coefficient of variation derived from standard deviation in CCF_{MSR} across the ensemble. The spatial distribution of the coefficient of variation for the projected scenarios in the future are presented in Figure 5.37.

The variation observed in the Mid 21st Century ranges between 5% to 35%, as seen in panel A of Figure 5.37. The regions formed show an increasing trend of variation in the study area from the southwest corner to the northeast. Variation between 20%

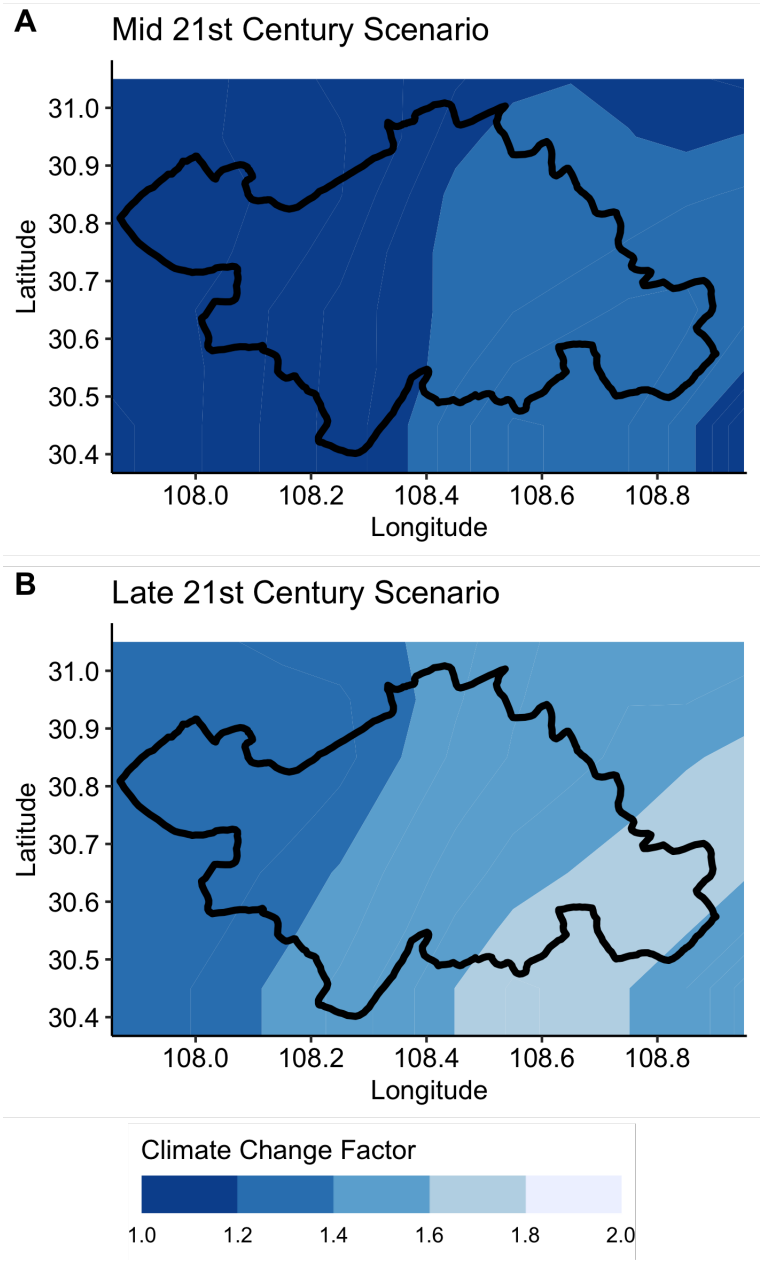

Figure 5.36: Mean seasonal rainfall climate change factors (CCF_{MSR}) derived from the ensemble mean for the months of May to August for the Mid 21st Century (A) and Late 21st Century (B) scenario projections.

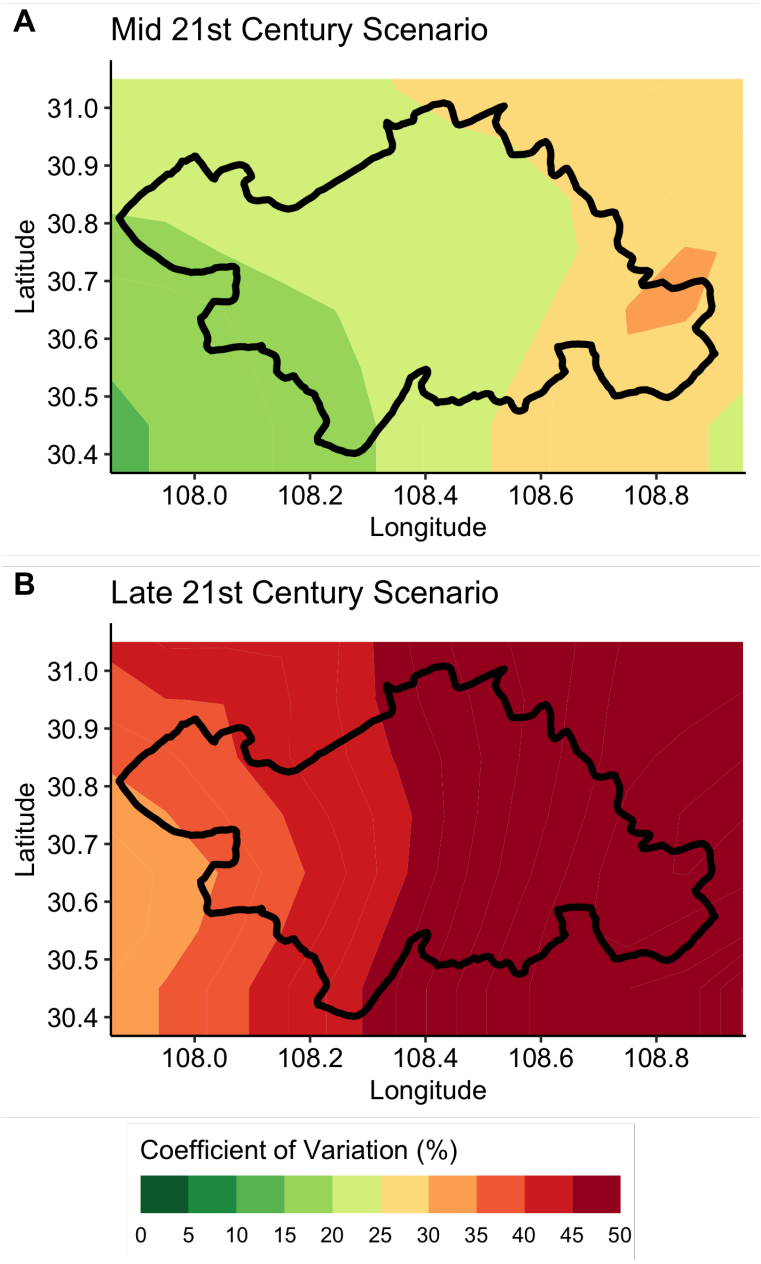

Figure 5.37: Coefficients of variation of the ensemble projections of climate change factors (CCF_{MSR}) derived from mean seasonal rainfall for May to August for the Mid 21st Century (A) and Late 21st Century (B) scenario projections.

to 25% was measured for the projected CCF_{MSR}, covering a majority of central areas within the Wanzhou County borders. The highest variation is observed in the southeast corner, ranging between 25% to 35%. The variation in CCF_{MSR} for the Late 21st Century ensemble projections is significantly larger than the Mid 21st Century, with a range of 30% to 50%, shown in panel B of Figure 5.37. The regional characteristics of the coefficient of variation in projected CCF_{MSR}shows a trend increasing from the west to east. The variation in a majority of the Wanzhou County area is between 45% to 50%, thus representing significant uncertainty in the projected CCF_{MSR}.

This large variation between ensemble members suggests a limitation in the building of the ensemble with equal weight, without a performance selection criteria. This also could be attributed to the influence of the QDM bias correction methods. Tong *et al.* [37] find that QDM tends to amplify the precipitation increases, and that this could substantially alter the magnitudes of the RCM outputs, and given the differences in the assembly of the ensemble, the climate signals for daily precipitation could have been greatly amplified. A further limitation revealed by the MSR in this section found in the limiting assumption that CDF-derived quantiles are stable throughout the future. Xu & Wang [71] find that climate variables in future projections change in higher-order moments, thus in applying daily precipitation bias correction that involve bias correction based on empirically derived CDFs, the amplified extreme rainfall under future projections create extreme deviation in the CDFs estimated. This can result in a distortion of the bias-corrected precipitation for the future projections, and lead to uncertainty in the ensemble projections for the Late 21st Century.

5.3.3 Climate Change Projections for Extreme Daily Rainfall

This section discusses the ensemble projections based on the $CCF_{EDR,T}$ derived from the bias-corrected extreme rainfall results. The analysis in this section considers the projected $CCF_{EDR,T}$ for corresponding to return periods (T) of 5, 10, 50 and 100 years. The results in this section presents the ensemble mean CCF for different return periods, derived from the results of the extreme even bias correction that were bilinearly interpolated into the CMFD grid. The uncertainty of the projected ensemble $CCF_{EDR,T}$ was analyzed with the spatial distribution of the coefficient of variation derived from the projected extreme daily rainfall $CCF_{EDR,T}$ of each individual ensemble member.

The spatial distribution of the ensemble $CCF_{EDR,T}$ derived from the mean is presented in Figure 5.38. A decrease below a $CCF_{EDR,T}$ value of 1 was observed western region of Wanzhou County across all return periods for the projections in the Mid 21st Century. The range of ensemble mean $CCF_{EDR,T}$ values are between 0.9 to 1.2. Three predominant regions emerging in the process.

The first region covers a band in the western region of the study area and the extreme daily rainfall is expected to decrease, as measured by the range of $CCF_{EDR,T}$ being

between 0.9 to 1.0. Within the western region of increase is a pocket area with an increase in $CCF_{EDR,T}$ for this scenario ranging from 1.0 to 1.2. The eastern region of the study areas shows a consistent CCF between 1.0 and 1.2. Although a small area in the southeast region of Wanzhou is projected to have a range of CCFs below 1.0, this region reduces in area as the return period increases from 5 years to 50 years, and is not evident in the values for 100-year events, $CCF_{EDR,100}$.

The spatial distribution of $CCF_{EDR,T}$ in the Mid 21st Century indicates that more areas will be subject to a decrease in magnitude when considering extreme daily rainfall with a return period of 5 to 10 years. Though, once higher return period T in $CCF_{EDR,T}$ are considered, more areas will experience a mild increase in magnitude. This is evident in the projections $CCF_{EDR,50}$ and $CCF_{EDR,100}$ year extreme daily rainfall.

The spatial distribution of the projected values of $CCF_{EDR,T}$ in the Late 21st Century projections, were presented in Figure 5.38. The ensemble mean projections for extreme daily rainfall corresponding to return periods of 5, 10, 50 and 100 years were illustrated.

Two characteristic regions, categorized by magnitude of ensemble $CCF_{EDR,T}$ are visible across return periods in Figure 5.38. The first region represents areas with projected $CCF_{EDR,T}$ between 1.2 and 1.4, predominantly covering the extent of the Wanzhou County area. The second region projects higher magnitudes of extreme daily rainfall with $CCF_{EDR,T}$ between 1.4 and 1.6 located around the study area and at the borders. The areas projecting higher extreme daily rainfall $CCF_{EDR,T}$ are evident in the southwest region for 5-year return period values, $CCF_{EDR,5}$, and increase to encircle the study area at the borers as the spatial distribution of return periods increase from 10, 50 to 100 years. The central region of the Wanzhou County area and the north east sees a consistent pattern of ensemble $CCF_{EDR,T}$ projections ranging between 1.2 to 1.4 for EDR, while the southeastern region sees an increase in projected CCF for EDR of 1.4 to 1.6.

The potential influence of orography in enhancing extreme daily rainfall under is evident in the Late 21st Century scenario projections. The risk area identified in Figure 5.30 has shifted northwest towards the northern mountain range at the boundary of Wanzhou County, illustrated in Figure 1.1. Several factors under climate change conditions can be attributed to the orogaphically enhanced extreme daily rainfall. Sandvik *et al.* [81] find that a change in precipitation phases result in significant increases in rainfall with increasing temperature and elevation in a study on historical orographically enhanced extreme precipitation events in Norway. Napoli *et al.* [82] see a historical difference between lowland and highland distributions of annual precipitation from the mid 20th century to the 1980's over the European Alpine region. The interdecadal increase was attributed to increased anthropogenic aerosol load, thus a causal link between antrhopogenic activity and the orographic enhancement of precipitation is suggested.

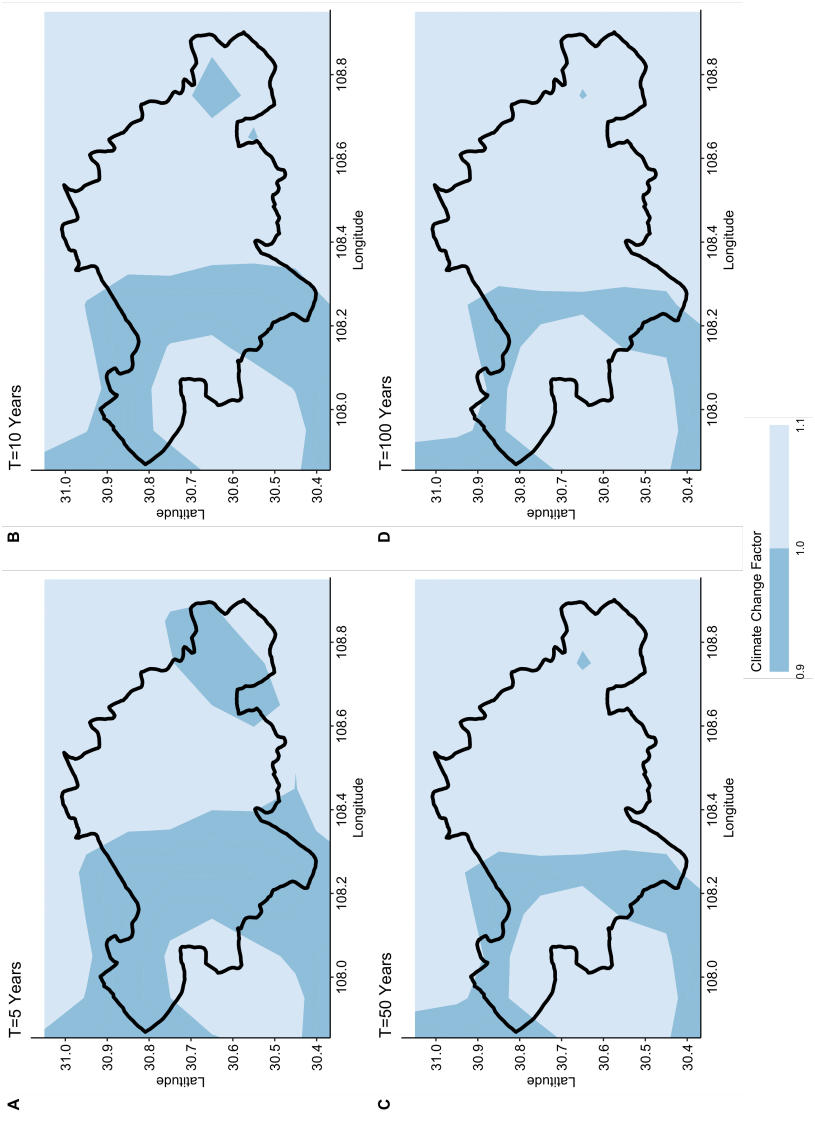

Figure 5.38: Mid 21st Century scenario projections of extreme daily rainfall climate change factors ($CCF_{EDR,T}$) for return periods (T) of 5, 10, 50 and 100 years derived from the ensemble mean projections covering the months of June to July.

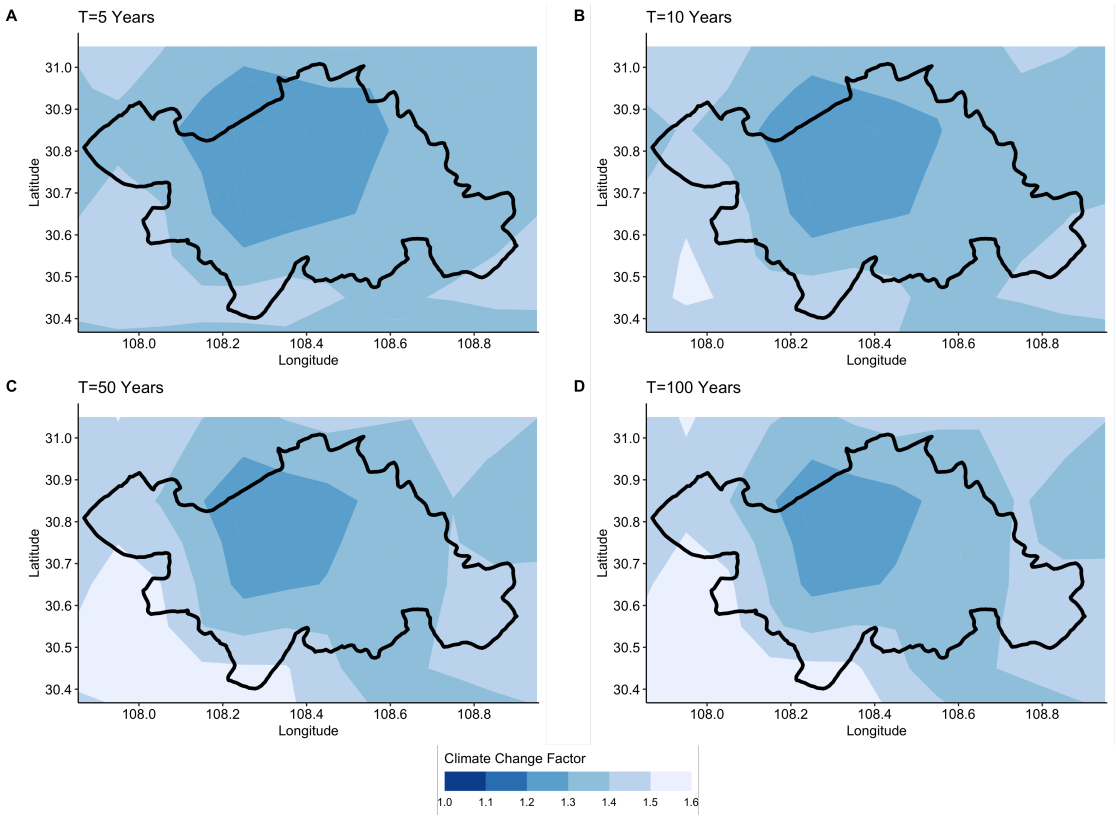

Figure 5.39: Late 21st Century scenario projections of extreme daily rainfall climate change factors ($CCF_{EDR,T}$) for return periods (T) of 5, 10, 50 and 100 years derived from the ensemble mean projections covering the months of June to July.

The uncertainty in the mean ensemble projections for the future climate change scenarios in the Mid and Late 21st Centuries were assessed and measured using the coefficient of variation in $CCF_{EDR,T}$ derived from the standard deviation of the ensemble. The coefficient of variation was calculated for each return period and the spatial distribution of this variation was analyzed. This assessment considers the uncertainty and variation in projected extreme daily rainfall with return periods of 5, 10, 50 and 100 year.

The spatial distribution for the coefficient of variation for the Mid 21st Century ensemble projections in Figure 5.40. The range of variation in ($CCF_{EDR,T}$ under the projections for this scenario is below 25% within the Wanzhou County area. There is an evident growth in uncertainty in the northern borders of the study area as the return period increases from 10 years to 100 years. Though the ensemble variation in this area is between 15% to 25%, a majority of the study area remains within the range of 10% to 15%. The least uncertainty in projections is found across the study area at lower return periods of 5 and 10 years.

The analysis of the spatial distribution in coefficients of variation in the Late 21st Century scenario is shown in Figure 5.41 The range of the variation of this scenario is between 0% and 30%. The variation is similar to the range observed in Mid 21st Century projections. The spatial distribution of the ensemble variation in the Late 21st Century differs from the Mid 21st Century as the return period increases.

A larger area of increased variation within the study area was observed in the Mid 21st Century as the return period increased from 10, 50 to 100 years, the variation for within the study area decreases in the Late 21st Century projections. This trend is particularly evident in the eastern region of the Wanzhou County area.

The coefficient of variation reduces from being within a range of 15% to 25%, corresponding to 10-year EDR, to a range of 10% to 20% in considering 50 and 100-year EDR. These results of this analysis indicates that there is less uncertainty in the projection of $CCF_{EDR,T}$ applicable to low frequency and high magnitude EDR in the Late 21st Century.

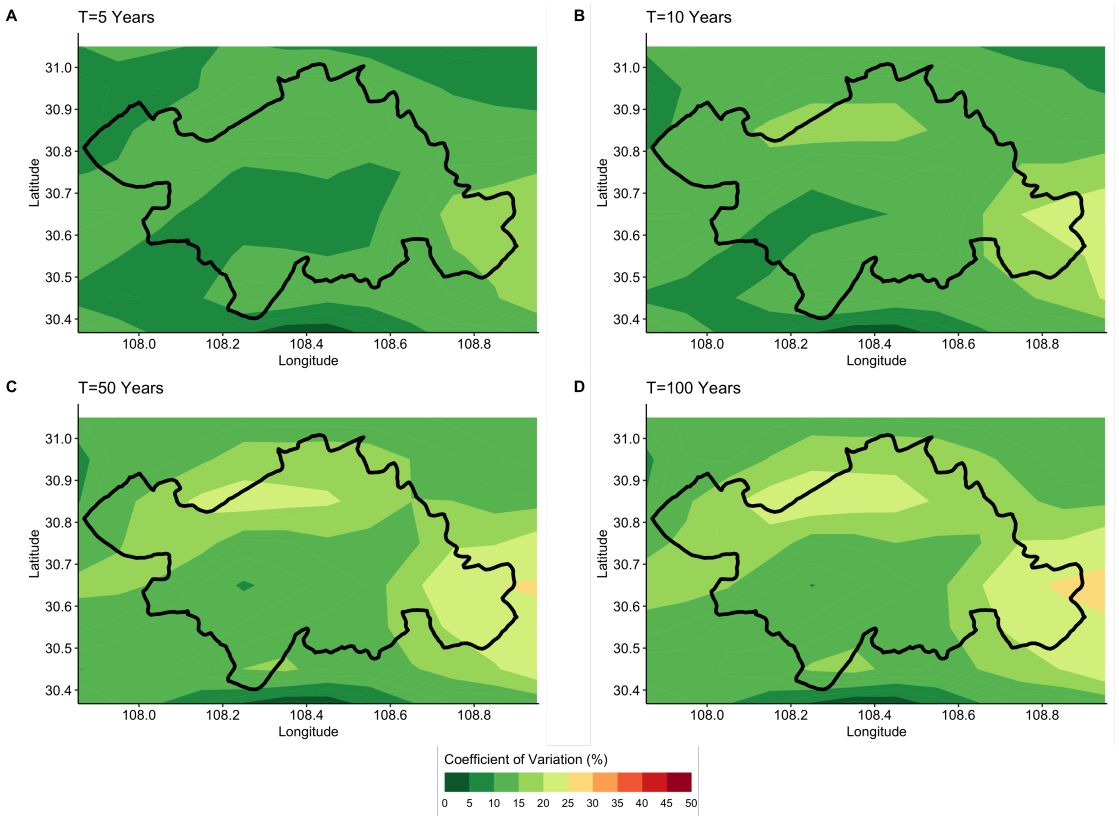

Figure 5.40: Coefficients of variation for Mid 21st Century scenario projection ensemble projections of climate change factors ($CCF_{EDR,T}$) with return periods (T)of 5, 10, 50 and 100 years derived from the ensemble mean projections covering the months of June to July.

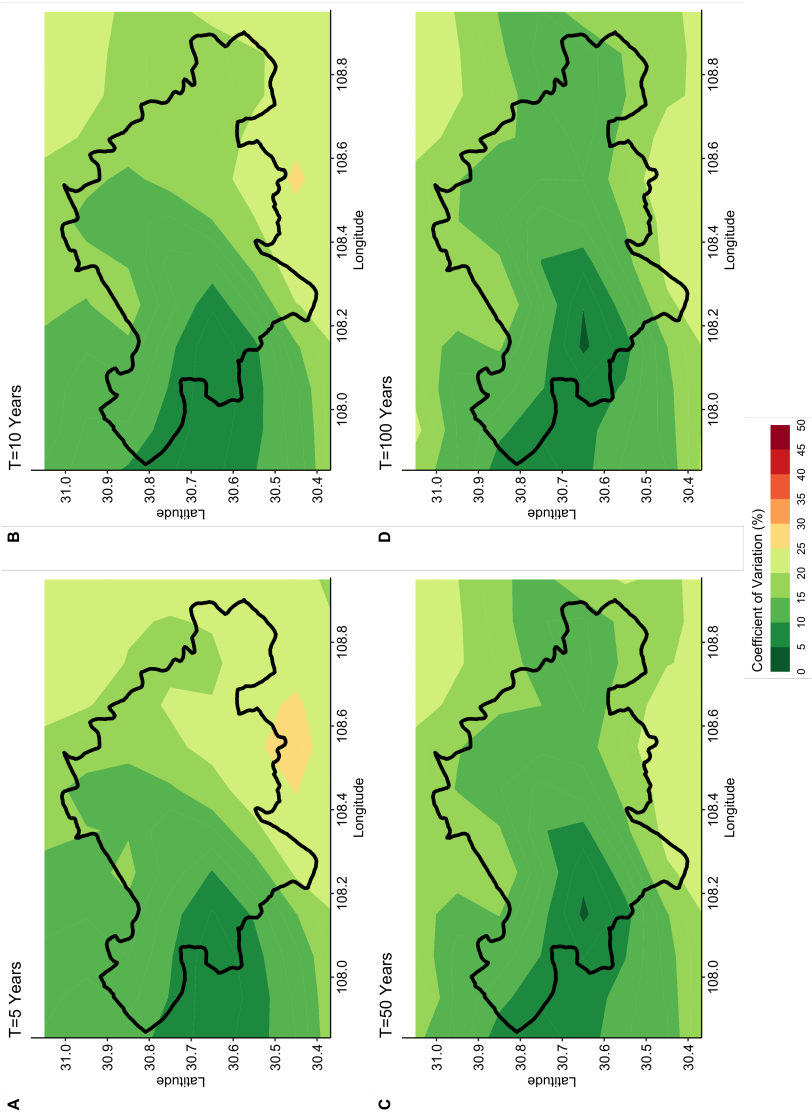

Figure 5.41: Coefficients of variation for Late 21st Century scenario projection ensemble projections of climate change factors ($CCF_{EDR,T}$) with return periods T of 5, 10, 50 and 100 years derived from the ensemble mean projections covering the months of June to July.

6 Conclusions and Recommendations

The final chapter of this study comprises of conclusions and recommendations derived from the limitations and results presented. This chapter aims to connect the conclusions and limitations in the methodology to provide recommendations in developing the methodological framework. The intention is to open insight for research lines that could result in the improvement of the framework with contemporary literature illustrating promising solutions for future lines of research.

The primary objective of this research project was to investigate the influence of climate change on rainfall conditions that could trigger shallow landslides. In order to investigate this primary research question, this study established a methodology to determine historical triggering rainfall conditions, assess the present rainfall conditions in the study area, and utilize climate model outputs to derive projections in the future.

This study presented a procedure to create scenarios from climate model outputs that could be integrated in slope stability model inputs. Through the presentation of results and the identification of sources of uncertainties, a viable methodology that can link climate change models as input in slope susceptibility assessment studies was presented.

The methodological framework developed in Figure 4.1 consisted of three main tasks to assess the influence of climate change on shallow landslide triggering rainfall conditions in Wanzhou County, China. The first task was to reconstruct the triggering rainfall conditions from 1995 to 2005. Second, to establish a reference scenario based on a present analysis of mean seasonal rainfall and extreme daily rainfall. Third, to analyze an ensemble of bias-corrected Regional Climate models (RCM) outputs to produce projections in the Mid 21st Century (2021-2060) and the Late 21st Century (2061-2100).

The Reconstruction of Triggering Rainfall Conditions

The first part of this research project was centered around reconstructing event rainfall and antecedent rainfall conditions for historical shallow landslides. The findings from the attempt to reconstruct the rainfall conditions in the inventory indicated that significant temporal uncertainty exists in the record dates of shallow landslide occurrences. This was primarily observed in the analysis of landslides from June to August that occurred during periods with zero antecedent recharge and no significant event rainfall.

The presence of significant temporal uncertainty was further assessed through a sensitivity analysis. The procedure involved the detection of maximum daily rainfall

prior to the record date that could possibly represent the event rainfall, and indicate the actual landslide date. The findings from this analysis revealed that 88% to 96% of the inventory could have occurred up to 7 days prior to the inventory record date. It was determined through this sensitivity analysis that a 7-day window prior to the record dates carried maximum uncertainty. The inventory record date is not the lone cause for uncertainty in this analysis. The CMFD gridded precipitation data set used to reconstruct the rainfall conditions is limited by its spatial resolution of 0.1^o or approximately 11 km^2. Another limitation of this analysis is the temporal resolution of daily precipitation selected in this study.

While uncertainties in the inventory and the limitations of the CMFD precipitation data set were identified in this portion of the research project, the reconstruction of the event rainfall at a daily time scale was not successfully performed. This was evident in an analysis of the 2D density plot representation of antecedent rainfall *Pa* and event rainfall *Pe*. While the clusters formed in the data suggested groups of landslides occurring with a range of *Pa* values between 3 and 6 mm/day and *Pe* with values between 10 and 30 mm/day, the uncertainty in the record date makes it difficult to establish conclusive insight from these ranges.

The temporal uncertainty had less influence over reconstructed antecedent rainfall over a 30-day period for the months of May to July. In an assessment of the reconstructed antecedent rainfall with a duration of 10, 15 and 30 days, it was found that reconstructing antecedent rainfall with a 15 and 30-day duration proved to be less sensitive to temporal uncertainty. A Kolmogorov-Smirnov test indicated statistical significance in the ability of antecedent rainfall with a 15 and 30-day duration to capture the frequency distribution of the triggering antecedent rainfall distributions with a 7-day window of uncertainty. Therefore, a reconstruction of 30-day antecedent rainfall based on inventory dates adjusted for a 7-day period of uncertainty in the maximum event rainfall was performed.

A comparison of the reconstructed 30-day antecedent rainfall versus the CMFD observations of daily rainfall across the study area was conducted in Figure 5.16. It was determined that the distribution of the reconstructed 30-day antecedent rainfall corresponding to shallow landslide occurrences in Wanzhou had a mean value that was statistically similar to that of the mean seasonal rainfall for May to August. Therefore it was concluded that the mean seasonal rainfall can adequately represent the antecedent rainfall that can trigger shallow landslides in Wanzhou County.

This study determined the approach of implementing a time-shifted window of uncertainty to detect significant volumes of daily rainfall on the date of the landslides would not address the temporal uncertainty in the record date, and increase the uncertainty in the data set. It is therefore proposed that an exploration of remote sensing techniques to incorporate satellite-derived data and aerial photographs. This can specifically be

applied to reconstruct the occurrence of shallow water during the landslide seasons of 1995-2005.

A study by Miura & Nagai [83] investigated landslide mapping of landslides in 2017 in the northern area of Kyushu, Japan using Advanced Himawari Imager (AHI)-derived normalized difference vegetation index (NDVI) time series data. Their results demonstrated that moderate and low spatial resolution data have the potential to successfully detect landslides.

While the scale of this research provides a regional overview on shallow landslide triggering rainfall occurrences, the adoption of this scale to the reconstruction of triggering event rainfall limits the level of spatial certainty of identifying event rainfall. Shallow landslides can occur due to intense local rainstorms on significantly smaller spatial scales. Therefore matching the spatial scale of the landslides with appropriate precipitation data is essential to reducing uncertainty in determining the magnitude of the triggering rainfall conditions. Tseng *et al.* [84] finds that high-resolution radar-derived quantitative precipitation estimates can be adopted to obtain better spatio-temporal precipitation patterns with a spatial resolution of 1 km, in contrast to the CMFD data resolution of approximately 11 km. Although the applicability of this suggestion is greatly limited by the quality and availability of radar-derived rainfall data, this study highlights the importance and potential of incorporating such data sets in the process of inventory reconstruction.

This study estimated the antecedent recharge over the entire catchment by the application of temporally-varying recharge parameters obtained from water balance calculations performed with the EasyBal hydrological model for one point in the study area [65]. The spatial variation of climate and hydrologic characteristics across the study area limits the insight from the estimation of antecedent recharge applied in this research. Kim *et al.* [26] recommend detailed regional scale hydrological model results integrated to capture more precise infiltration calculations, and gain a better understanding of soil moisture conditions.

This insight is critical in the reconstruction of triggering rainfall conditions, and in predicting the watershed response to under a changing climate. Huang *et al.* [38] uses a variable infiltration capacity (VIC) hydrology model and regional climate model (RCM) outputs to assess the hydrological responses of the Upper Yangtze River Basin to climate change from 2020 to 2050. The integration of hydrological results, and a thorough comparison of historical watershed responses to the future responses will add value to advancing methods in the reconstruction and projections of landslide triggering rainfall conditions. The integration of the impact of climate change on the hydrological cycle is crucial in incorporating the influence of temperature and precipitation on recharge and the groundwater table.

An Analysis of the Present Summer Season Rainfall

The second part of this research project focused on establishing magnitudes and spatial patterns of mean seasonal rainfall and extreme daily rainfall in the present to provide reference scenarios for potential triggering rainfall conditions. The findings on the ability for mean seasonal rainfall to adequately represent the triggering antecedent rainfall conditions was applied in to perform this research task. The mean seasonal rainfall over Wanzhou County was then derived from the months of May to August, over the period of 1979 to 2018. An assessment on the ability of mean seasonal rainfall derived for Wanzhou County to represent rainfall magnitudes and frequency distributions was conducted. It was determined that the reference scenario measures a relative deviation ranging from -20% to +20%, compared to mean monthly rainfall from May to August. An analysis of the frequency distribution of the seasonal mean across the 1979 to 2018 showed that the main deviation from the frequency distribution of the reference scenario was observed in July.

The reference scenario for extreme daily rainfall was derived from fitting Gumbel distributions to extreme daily rainfall. The extreme daily rainfall was derived by a monthly block maxima approach applied to daily precipitation observed over June to August from 1979 to 2018. The Gumbel fittings garnered positive goodness-of-fit evaluations using the Anderson-Darling, Kolmogorov-Smirnov and Cramer-von-Mises tests. It was concluded that the Gumbel frequency distribution was capable of capturing seasonal extremes, with a confidence interval of 95%. The tendency for the Gumbel distribution to yield the smallest possible rainfall, thus returning the highest possible risk in comparison to other extreme value distributions was a consideration in the application of these fitted results [80].

This research focuses on analyzing and projecting summer season rainfall conditions. In order to gain a broader understanding of the triggering rainfall conditions on an annual temporal scale, rather than a seasonal period, adjustments to the approach in extreme value frequency distribution modeling can be made. The Gumbel fit distribution was selected and determined to perform adequately in the results of this study, with a stationary assumption encompassing the periods of scenarios selected to be focused on. The seasonal approach to utilizing non-stationary generalized extreme value (GEV) distributions results in monthly resolved return levels, and more precise estimations of annual return levels [66, 67]. Furthermore, the application of GEV distributions will introduce a multi-distribution approach that will result in increasing the capability of the bias correction transfer functions to capture the extreme daily precipitation distribution at different locations across the study area [38].

A spatial analysis of extreme daily rainfall corresponding to 5, 10, 50 and 100-year return periods was conducted. It was observed that an area in the center of Wanzhou County, and downstream of the Yangtze River is exposed to high magnitude, low

frequency extreme daily rainfall. The results and insight can also provide beneficial insight to hazard assessments of urban and flash floods within Wanzhou County.

The potential orographic influence in enhancing extreme daily rainfall could be invested further to assess the physical process driving the precipitation that in the detected risk area. Kumar *et al.* [85] presented a framework to reduce uncertainties and assess isolated systematic interactions between Mediterranean cyclones and orographic barriers. Their study's finds indicate that the processes governing the distributions of extreme rainfall a vary with time scales taken into consideration. The maximum impact of orographic enhancement on precipitation was observed to occur at an hourly scale. In order to assess impact of orographic barriers on extremes on the present extreme events, sub-daily rainfall observations must be incorporated into the extreme daily rainfall analysis and frequency distribution modeling.

Projected Summer Rainfall Under Climate Change

The final task of this research was to analyze projections for the months of May to August described by the RCP 8.5 climate change scenario. The changes in mean seasonal rainfall and extreme daily rainfall were assessed for the future periods in the Mid-21st Century from 2021-2060 and Late 21st Century from 2061-2100. The projections utilized an ensemble consisting of the MPI-ESM and HadGEM2-ES Global climate models (GCM) driving REMO2015 and RegCM4 Regional climate model (RCM) outputs. The climate model outputs were bias-corrected, and the mean ensemble projections were taken into consideration. The mean ensemble projections were reported as Climate Change Factors (CCFs) capturing the relative change from the reference period of 1979 to 2018. The projections for mean seasonal rainfall were communicated through CCF_{MSR}, while the extreme daily rainfall projections for different return periods (T) were represented by $CCF_{EDR,T}$.

The mean seasonal rainfall projections over Wanzhou County increase in the Mid 21st Century, measured by a range of CCF_{MSR} between 1.0 and 1.4. The projected CCF_{MSR} in the Late 21st Century had of 1.2 and 1.8. The uncertainty in the mean ensemble projections were then assessed with a coefficient of variation. It was found that the variation in CCF_{MSR} in the Mid 21st Century projections was between 10% and 35%. There was greater uncertainty in the projections of the Late 21st Century, with a range of 30% to 50%.

The significant variation in the far Late 21st Century projections can be attributed to uncertainty derived from bias correction technique for daily precipitation. This attributed to limitations in the ability to address large magnitude rainfall events and correct systematic bias. Research indicates that bias correction by quantile delta method (QDM) results in the a tendency of amplification in magnitudes of precipitation. Furthermore, bias corrections based on transfer functions derived from empirical cumulative

density functions (CDFs) of the projections and the observations cannot provide a stable representation of the distributions in future climate projection [37, 71]. These factors could magnify systematic biases in extreme daily rainfall of the Late 21st Century climate model projections, as observed in the significant variation observed in the ensemble for this period.

The bias-corrected results also reflect the limitations inherent in the selection of GCM-RCM ensemble combinations. The variation in the ensemble CCFs suggests the 4-member ensemble is limited producing converging projections for the Late 21st Century. The results of Tong *et al.* [37] indicate the limitations of climate model output responses to bias correction methods can be countered with an expanded ensemble to decrease uncertainty and create robust projections.

The projections of the extreme daily rainfall indicate a decrease in magnitude of extreme precipitation in the Mid 21st Century. The range of $CCF_{EDR,T}$ for extreme daily rainfall was projected to be between 0.9 to 1.2. Extreme daily rainfall in the Late 21st Century projections showed an increase similar to that observed in the $CCF_{EDR,T}$ for mean seasonal daily rainfall. The range of $CCF_{EDR,T}$ in the Late 21st Century ranged between 1.2 to 1.8. The uncertainty in the ensemble projection for $CCF_{EDR,T}$ ranged between 5% to 25% in both the Mid 21st Century and Late 21st Century scenarios, as measured by a coefficient of variation.

The analysis of uncertainty indicates that the bias correction methodology applied to extreme daily rainfall was able to coherently remove the systematic bias in the ensemble. The range of variation is also an indication of the convergence of extreme daily rainfall signals across the projections of the ensemble members. The bias correction for these results was performed through QDM with a parametric transfer function through a Gumbel frequency distribution model. Huang *et al.* [38] indicates that the extreme daily rainfall across a region may be better represented with a mixture of distributions applied as transfer functions in the bias correction. Therefore, the assumption that the Gumbel fit could represent present and future frequency distributions of extreme daily rainfall across the rainfall is a limitation of these results.

The utilization of Regional climate model (RCM) outputs are relatively coarse in spatial resolution when compared to the gridded precipitation observations. The RCMs are run at resolutions of approximately 22 km^2, while the observations are available at approximately 10 km^2. While higher resolution RCM models in the CMIP6 outputs are not yet available at the daily resolution required for this research project, the application of a Bias Correction and Spatial Disaggregation (BCSD) algorithm [86] could improve the climate change projections. The spatial disaggregation aspect to BCSD involves using a scale factor derived from the difference of the detrended climate model output and the detrended gridded precipitation, in order to statistically downscale the coarse projections into the finer observation grid.

Yang *et al.* [39] assessed the performance of BCSD on Global climate models over China. Their findings were that BCSD outperformed other statistical downscaling methods in correcting frequency distributions of daily precipitation, and extreme precipitation indices. Xu & Wang [71] applied the BCSD method to daily maximum temperatures from a multi-model of CMIP5 GCM results. Their findings indicate that BCSD is capable of yielding significant improvement of raw model results through the reduction of inter-model spread of temperature values, and reduction of temporal variability across indices.

The ability of an RCM to produce seasonal climate and the extreme daily rainfall is dependent on the performance of the boundary conditions provided by the Global climate model (GCM) [41]. Employing an ensemble of climate model combinations is one approach to obtaining projections and reducing uncertainty due to biases and systematic errors in different GCMs. While Giorgi & Coppola [58] recommend a minimum of 4 to 5 models in an ensemble, Yang *et al.* [52] find that the optimal multi-model ensemble to represent the climatology of China requires 9 GCM. Therefore, involving more climate model outputs may be one way to increase the certainty of climate projections over Wanzhou County.

Another approach to improving the ensemble climate change projections could involve a better selection of ensemble members. Although Christensen *et al.* [59] finds that equal averaging of ensemble members yields sufficient results, the application of reliable ensemble averaging (REA) method by Olmos Giménez *et al.* [60] finds a reduction in uncertainty from systematic climate model bias, and a decrease in cumulative errors for rainfall. The performance of the REA method in establishing better ensemble projections is highlighted by an application of improved inputs to hydrological models. Therefore, it is recommended that a wider ensemble of RCMs and a better selection procedure to assess the reliability of the ensemble be performed to improve climate change projections in this study.

In conclusion, this research project delivered proof-of-concept for a methodological framework to derive shallow landslide triggering rainfall scenarios from climate model outputs. The resulting Climate Change Factors (CCFs) provide rainfall scenarios to incorporate future event rainfall and antecedent rainfall in susceptibility assessments using the Fast Shallow Landslide Assessment Model (FSLAM). The application of extreme daily rainfall and mean seasonal rainfall CCFs for the Mid 21st Century and Late 2st Century is simply through multiplication to spatially distributed reference rainfall values in present rainfall conditions.

Bibliography

1. Wallemacq, P. & House, R. *Economic losses, poverty & disasters: 1998-2017* 2018. https://www.preventionweb.net/files/61119_credeconomiclosses.pdf (2021) (cit. on p. 1).
2. Froude, M. J. & Petley, D. N. Global fatal landslide occurrence from 2004 to 2016. *Natural Hazards and Earth System Sciences* **18.** Publisher: Copernicus GmbH, 2161–2181. ISSN: 1561-8633. https://nhess.copernicus.org/articles/18/2161/2018/ (2021) (Aug. 23, 2018) (cit. on pp. 1, 6).
3. Gariano, S. L. & Guzzetti, F. Landslides in a changing climate. *Earth-Science Reviews* **162,** 227–252. ISSN: 0012-8252. https://www.sciencedirect.com/science/article/pii/S0012825216302458 (2021) (Nov. 1, 2016) (cit. on pp. 1, 2, 5, 8, 16, 17, 30).
4. Hartmann, D. L. in *Global Physical Climatology (Second Edition)* (ed Hartmann, D. L.) 397–425 (Elsevier, Boston, Jan. 1, 2016). ISBN: 978-0-12-328531-7. https://www.sciencedirect.com/science/article/pii/B978012328531700013X (2021) (cit. on pp. 1, 4).
5. Keenan, R. *et al.* Dynamics of global forest area: Results from the FAO Global Forest Resources Assessment 2015. *Forest Ecology and Management* **352,** 9–20 (2015) (cit. on p. 1).
6. Groisman, P. Y. *et al.* Trends in Intense Precipitation in the Climate Record. *Journal of Climate* **18.** Publisher: American Meteorological Society Section: Journal of Climate, 1326–1350. ISSN: 0894-8755, 1520-0442. https://journals.ametsoc.org/view/journals/clim/18/9/jcli3339.1.xml (2021) (May 1, 2005) (cit. on p. 1).
7. Alexander, L. V. *et al.* Global observed changes in daily climate extremes of temperature and precipitation. *Journal of Geophysical Research: Atmospheres* **111.** ISSN: 2156-2202. https://agupubs.onlinelibrary.wiley.com/doi/abs/10.1029/2005JD006290 (2021) (D5 2006) (cit. on pp. 1, 4).
8. Peres, D. J. & Cancelliere, A. Modeling impacts of climate change on return period of landslide triggering. *Journal of Hydrology* **567,** 420–434. ISSN: 0022-1694. https://www.sciencedirect.com/science/article/pii/S0022169418307984 (2021) (Dec. 1, 2018) (cit. on pp. 2, 5, 16, 17, 30).
9. Li, Y. & Mo, P. A unified landslide classification system for loess slopes: A critical review. *Geomorphology* **340,** 67–83. ISSN: 0169-555X. https://www.sciencedirect.com/science/article/pii/S0169555X19301758 (2021) (Sept. 1, 2019) (cit. on p. 2).
10. Nedumpallile Vasu, N. *et al.* A new approach to temporal modelling for landslide hazard assessment using an extreme rainfall induced-landslide index. *Engineering Geology* **215,** 36–49. ISSN: 0013-7952. https://www.sciencedirect.com/science/article/pii/S0013795216305026 (2021) (Dec. 19, 2016) (cit. on pp. 2, 3).

11. Medina, V., Hürlimann, M., Guo, Z., Lloret, A. & Vaunat, J. Fast physically-based model for rainfall-induced landslide susceptibility assessment at regional scale. *CATENA* **201,** 105213. ISSN: 0341-8162. https://www.sciencedirect.com/science/article/pii/S0341816221000722 (2021) (June 1, 2021) (cit. on pp. 2, 3).

12. Scheidl, C. *et al.* The influence of climate change and canopy disturbances on landslide susceptibility in headwater catchments. *Science of The Total Environment* **742,** 140588. ISSN: 0048-9697. https://www.sciencedirect.com/science/article/pii/S0048969720341103 (2021) (Nov. 10, 2020) (cit. on pp. 2, 4, 5, 17).

13. Aristizábal, E., Vélez, J. I., Martínez, H. E. & Jaboyedoff, M. SHIA_Landslide: a distributed conceptual and physically based model to forecast the temporal and spatial occurrence of shallow landslides triggered by rainfall in tropical and mountainous basins. *Landslides* **13,** 497–517. ISSN: 1612-5118. https://doi.org/10.1007/s10346-015-0580-7 (2021) (June 1, 2016) (cit. on p. 3).

14. Segoni, S., Piciullo, L. & Gariano, S. L. A review of the recent literature on rainfall thresholds for landslide occurrence. *Landslides* **15,** 1483–1501. ISSN: 1612-510X, 1612-5118. http://link.springer.com/10.1007/s10346-018-0966-4 (2021) (Aug. 2018) (cit. on pp. 3, 39).

15. Polemio, M. & Petrucci, O. Occurrence of landslide events and the role of climate in the twentieth century in Calabria, southern Italy. *QUARTERLY JOURNAL OF ENGINEERING GEOLOGY & HYDROGEOLOGY* **43.** https://trid.trb.org/view/1100062 (2021) (Nov. 2010) (cit. on p. 4).

16. Donat, M. G., Lowry, A. L., Alexander, L. V., O'Gorman, P. A. & Maher, N. More extreme precipitation in the world's dry and wet regions. *Nature Climate Change* **6.** Number: 5 Publisher: Nature Publishing Group, 508–513. ISSN: 1758-6798. https://www.nature.com/articles/nclimate2941 (2021) (May 2016) (cit. on p. 4).

17. Brönnimann, S. *et al.* Changing seasonality of moderate and extreme precipitation events in the Alps. *Natural Hazards and Earth System Sciences* **18.** Publisher: Copernicus GmbH, 2047–2056. ISSN: 1561-8633. https://nhess.copernicus.org/articles/18/2047/2018/ (2021) (July 27, 2018) (cit. on p. 5).

18. Liu, Y., Yin, K., Chen, L., Wang, W. & Liu, Y. A community-based disaster risk reduction system in Wanzhou, China. *International Journal of Disaster Risk Reduction* **19,** 379–389. ISSN: 2212-4209. https://www.sciencedirect.com/science/article/pii/S2212420916303405 (2021) (Oct. 1, 2016) (cit. on pp. 6, 20).

19. Xiao, T., Segoni, S., Chen, L., Yin, K. & Casagli, N. A step beyond landslide susceptibility maps: a simple method to investigate and explain the different outcomes obtained by different approaches. *Landslides* **17,** 627–640. ISSN: 1612-5118. https://doi.org/10.1007/s10346-019-01299-0 (2021) (Mar. 1, 2020) (cit. on pp. 6, 19).

20. Huang, F., Yin, K., Huang, J., Gui, L. & Wang, P. Landslide susceptibility mapping based on self-organizing-map network and extreme learning machine. *Engineering Geology* **223,** 11–22. ISSN: 0013-7952. https://www.sciencedirect.com/science/article/pii/S0013795216303143 (2021) (June 7, 2017) (cit. on pp. 6, 20–22).

21. Xiao, L., Wang, J., Zhu, Y. & Zhang, J. Quantitative Risk Analysis of a Rainfall-Induced Complex Landslide in Wanzhou County, Three Gorges Reservoir, China. *International Journal of Disaster Risk Science* **11,** 347–363. ISSN: 2192-6395. https://doi.org/10.1007/s13753-020-00257-y (2021) (June 1, 2020) (cit. on pp. 6, 20, 22, 23, 41, 48, 93).

22. Coles, S. *An Introduction to Statistical Modeling of Extreme Values* ISBN: 978-1-85233-459-8. https://www.springer.com/gp/book/9781852334598 (2021) (Springer-Verlag, London, 2001) (cit. on pp. 11, 41).

23. Crozier, M. *Landslides: Causes, Consequences and Environment.* (Routledge, London, 1989) (cit. on p. 12).

24. Hong, M., Kim, J. & Jeong, S. Rainfall intensity-duration thresholds for landslide prediction in South Korea by considering the effects of antecedent rainfall. *Landslides* **15,** 523–534. ISSN: 1612-510X, 1612-5118. http://link.springer.com/10.1007/s10346-017-0892-x (2021) (Mar. 2018) (cit. on p. 12).

25. Khan, Y. A., Lateh, H., Baten, M. A. & Kamil, A. A. Critical antecedent rainfall conditions for shallow landslides in Chittagong City of Bangladesh. *Environmental Earth Sciences* **67,** 97–106. ISSN: 1866-6280, 1866-6299. http://link.springer.com/10.1007/s12665-011-1483-0 (2021) (Sept. 2012) (cit. on p. 12).

26. Kim, S. W. *et al.* Effect of antecedent rainfall conditions and their variations on shallow landslide-triggering rainfall thresholds in South Korea. *Landslides* **18,** 569–582. ISSN: 1612-510X, 1612-5118. http://link.springer.com/10.1007/s10346-020-01505-4 (2021) (Feb. 2021) (cit. on pp. 12, 39, 48, 117).

27. Ma, T., Li, C., Lu, Z. & Wang, B. An effective antecedent precipitation model derived from the power-law relationship between landslide occurrence and rainfall level. *Geomorphology* **216,** 187–192. ISSN: 0169555X. https://linkinghub.elsevier.com/retrieve/pii/S0169555X14001676 (2021) (July 2014) (cit. on p. 12).

28. Marques, R., Zêzere, J., Trigo, R., Gaspar, J. & Trigo, I. Rainfall patterns and critical values associated with landslides in Povoação County (São Miguel Island, Azores): relationships with the North Atlantic Oscillation. *Hydrological Processes* **22,** 478–494. ISSN: 08856087, 10991085. http://doi.wiley.com/10.1002/hyp.6879 (2021) (Feb. 15, 2008) (cit. on p. 12).

29. Mathew, J., Babu, D. G., Kundu, S., Kumar, K. V. & Pant, C. C. Integrating intensity–duration-based rainfall threshold and antecedent rainfall-based probability estimate towards generating early warning for rainfall-induced landslides in parts of the Garhwal Himalaya, India. *Landslides* **11,** 575–588. ISSN: 1612-510X, 1612-5118. http://link.springer.com/10.1007/s10346-013-0408-2 (2021) (Aug. 2014) (cit. on pp. 12, 13, 39).

30. Tang, D., Li, D.-Q. & Cao, Z.-J. Slope stability analysis in the Three Gorges Reservoir Area considering effect of antecedent rainfall. *Georisk: Assessment and Management of Risk for Engineered Systems and Geohazards* **11,** 161–172. ISSN: 1749-9518, 1749-9526. https://www.tandfonline.com/doi/full/10.1080/17499518.2016.1193205 (2021) (Apr. 3, 2017) (cit. on pp. 12, 15, 39).

31. Tu, X., Kwong, A., Dai, F., Tham, L. & Min, H. Field monitoring of rainfall infiltration in a loess slope and analysis of failure mechanism of rainfall-induced landslides. *Engineering Geology* **105,** 134–150. ISSN: 00137952. https://linkinghub.elsevier.com/retrieve/pii/S0013795208003153 (2021) (Apr. 2009) (cit. on pp. 12, 13).

32. Segoni, S., Pappafico, G., Luti, T. & Catani, F. Landslide susceptibility assessment in complex geological settings: sensitivity to geological information and insights on its parameterization. *Landslides* **17,** 2443–2453. ISSN: 1612-5118. https://doi.org/10.1007/s10346-019-01340-2 (2021) (Oct. 1, 2020) (cit. on p. 12).

33. Dahal, R. K. & Hasegawa, S. Representative rainfall thresholds for landslides in the Nepal Himalaya. *Geomorphology* **100,** 429–443. ISSN: 0169-555X. https://www.sciencedirect.com/science/article/pii/S0169555X08000172 (2021) (Aug. 15, 2008) (cit. on pp. 13, 14, 39).

34. Alvioli, M. *et al.* Implications of climate change on landslide hazard in Central Italy. *Science of The Total Environment* **630,** 1528–1543. ISSN: 00489697. https://linkinghub.elsevier.com/retrieve/pii/S0048969718307150 (2021) (July 2018) (cit. on pp. 16, 17).

35. Song, Y. *et al.* Landslide Susceptibility Mapping Based on Weighted Gradient Boosting Decision Tree in Wanzhou Section of the Three Gorges Reservoir Area (China). *ISPRS International Journal of Geo-Information* **8.** Number: 1 Publisher: Multidisciplinary Digital Publishing Institute, 4. https://www.mdpi.com/2220-9964/8/1/4 (2021) (Jan. 2019) (cit. on pp. 20, 21).

36. Xiao, T., Yin, K., Yao, T. & Liu, S. Spatial prediction of landslide susceptibility using GIS-based statistical and machine learning models in Wanzhou County, Three Gorges Reservoir, China. *Acta Geochimica* **38,** 654–669. ISSN: 2365-7499. https://doi.org/10.1007/s11631-019-00341-1 (2021) (Oct. 1, 2019) (cit. on p. 21).

37. Tong, Y. *et al.* Bias correction of temperature and precipitation over China for RCM simulations using the QM and QDM methods. *Climate Dynamics.* ISSN: 1432-0894. https://doi.org/10.1007/s00382-020-05447-4 (2021) (Sept. 8, 2020) (cit. on pp. 27, 46, 47, 107, 120).

38. Huang, Y. *et al.* Hydrological projections in the upper reaches of the Yangtze River Basin from 2020 to 2050. *Scientific Reports* **11.** Bandiera_abtest: a Cc_license_type: cc_by Cg_type: Nature Research Journals Number: 1 Primary_atype: Research Publisher: Nature Publishing Group Subject_term: Climate change;Hydrology Subject_term_id: climate-change;hydrology, 9720. ISSN: 2045-2322. https://www.nature.com/articles/s41598-021-88135-5 (2021) (May 6, 2021) (cit. on pp. 27–29, 31, 46, 48, 103, 117, 118, 120).

39. Yang, Y., Tang, J., Xiong, Z., Wang, S. & Yuan, J. An intercomparison of multiple statistical downscaling methods for daily precipitation and temperature over China: present climate evaluations. *Climate Dynamics* **53,** 4629–4649. ISSN: 1432-0894. https://doi.org/10.1007/s00382-019-04809-x (2021) (Oct. 1, 2019) (cit. on pp. 27, 46, 121).

40. Gao, X., Xu, Y., Zhao, Z., Pal, J. S. & Giorgi, F. On the role of resolution and topography in the simulation of East Asia precipitation. *Theoretical and Applied Climatology* **86,** 173–185. ISSN: 1434-4483. https://doi.org/10.1007/s00704-005-0214-4 (2021) (Sept. 1, 2006) (cit. on pp. 27, 45).

41. Gao, X. *et al.* Performance of RegCM4 over major river basins in China. *Advances in Atmospheric Sciences* **34,** 441–455. ISSN: 1861-9533. https://doi.org/10.1007/s00376-016-6179-7 (2021) (Apr. 1, 2017) (cit. on pp. 29, 30, 121).

42. Liu, J., Du, J., Yang, Y. & Wang, Y. Evaluating extreme precipitation estimations based on the GPM IMERG products over the Yangtze River Basin, China. *Geomatics, Natural Hazards and Risk* **11.** Publisher: Taylor & Francis _eprint: https://doi.org/10.1080/19475705.2020.1734103, 601–618. ISSN: 1947-5705. https://doi.org/10.1080/19475705.2020.1734103 (2021) (Jan. 1, 2020) (cit. on pp. 30, 34).

43. Jingwei, X. *et al.* The Assessment of Surface Air Temperature and Precipitation Simulated by Regional Climate Model REMO over China. *CLIMATE CHANGE RESEARCH* **12.** Number: 4, 286–293. ISSN: 1673-1719. http://www.climatechange.cn (2021) (July 2016) (cit. on p. 31).

44. Xu, J. *et al.* Downstream effect of Hengduan Mountains on East China in the REMO regional climate model. *Theoretical and Applied Climatology.* Publisher: SPRINGER WIEN. ISSN: 0177-798X. http://doi.org/10.1007/s00704-018-2721-0 (2021) (Dec. 14, 2018) (cit. on p. 31).

45. Gu, H., Yu, Z., Yang, C. & Ju, Q. Projected Changes in Hydrological Extremes in the Yangtze River Basin with an Ensemble of Regional Climate Simulations. *Water* **10.** Number: 9 Publisher: Multidisciplinary Digital Publishing Institute, 1279. https://www.mdpi.com/2073-4441/10/9/1279 (2021) (Sept. 2018) (cit. on p. 31).

46. Gu, H. *et al.* Assessing CMIP5 general circulation model simulations of precipitation and temperature over China. *International Journal of Climatology* **35,** 2431–2440. ISSN: 1097-0088. https://rmets.onlinelibrary.wiley.com/doi/abs/10.1002/joc.4152 (2021) (2015) (cit. on p. 32).

47. He, J. *et al.* The first high-resolution meteorological forcing dataset for land process studies over China. *Scientific Data* **7.** Bandiera_abtest: a Cc_license_type: cc_publicdomain Cg_type: Nature Research Journals Number: 1 Primary_atype: Research Publisher: Nature Publishing Group Subject_term: Environmental sciences;Hydrology Subject_term_id: environmental-sciences;hydrology, 25. ISSN: 2052-4463. https://www.nature.com/articles/s41597-020-0369-y (2021) (Jan. 21, 2020) (cit. on pp. 33, 35).

48. Jacob, D. *et al.* Assessing the Transferability of the Regional Climate Model REMO to Different COordinated Regional Climate Downscaling EXperiment (CORDEX) Regions. *Atmosphere* **3.** Number: 1 Publisher: Molecular Diversity Preservation International, 181–199. https://www.mdpi.com/2073-4433/3/1/181 (2021) (Mar. 2012) (cit. on pp. 33, 38).

49. Zhe, L., DaWen, Y. & Hong, Y. Multi-scale evaluation of high-resolution multi-sensor blended global precipitation products over the Yangtze River. *Journal of Hydrology (Amsterdam)* **500.** Publisher: Elsevier Ltd, 157–169. ISSN: 0022-1694. https://www.cabdirect.org/cabdirect/abstract/20133322462 (2021) (2013) (cit. on p. 34).

50. Huffman, G. J. *et al.* The TRMM Multisatellite Precipitation Analysis (TMPA): Quasi-Global, Multiyear, Combined-Sensor Precipitation Estimates at Fine Scales. *Journal of Hydrometeorology* **8.** Publisher: American Meteorological Society Section: Journal of Hydrometeorology, 38–55. ISSN: 1525-7541, 1525-755X. https://journals.ametsoc.org/view/journals/hydr/8/1/jhm560_1.xml (2021) (Feb. 1, 2007) (cit. on p. 34).

51. Yatagai, A. *et al.* A 44-Year Daily Gridded Precipitation Dataset for Asia Based on a Dense Network of Rain Gauges. *Sola* **5,** 137–140 (2009) (cit. on p. 35).

52. Yang, X. *et al.* The Optimal Multimodel Ensemble of Bias-Corrected CMIP5 Climate Models over China. *Journal of Hydrometeorology* **21.** Publisher: American Meteorological Society Section: Journal of Hydrometeorology, 845–863. ISSN: 1525-7541, 1525-755X. https://journals.ametsoc.org/view/journals/hydr/21/4/jhm-d-19-0141.1.xml (2021) (Apr. 1, 2020) (cit. on pp. 35, 37, 121).

53. Zhenyu, H. a. N. & Tianjun, Z. Assessing the Quality of APHRODITE High-Resolution Daily Precipitation Dataset over Contiguous China. *59276c1479d15b66* **36.** Publisher: 59276c1479d15b66, 361–373. ISSN: 1006-9895. http://www.iapjournals.ac.cn/dqkx/en/article/doi/10.3878/j.issn.1006-9895.2011.11043 (2021) (2012) (cit. on p. 35).

54. Taylor, K. E., Stouffer, R. J. & Meehl, G. A. An Overview of CMIP5 and the Experiment Design. *Bulletin of the American Meteorological Society* **93.** Publisher: American Meteorological Society Section: Bulletin of the American Meteorological Society, 485–498. https://journals.ametsoc.org/view/journals/bams/93/4/bams-d-11-00094.1.xml (2021) (Apr. 1, 2012) (cit. on p. 36).

55. Moss, R. H., Nakicenovic, N. & O'Neill, B. C. *Towards New Scenarios for Analysis of Emissions, Climate Change, Impacts, and Response Strategies* 132 pp. ISBN: 978-92-9169-125-8. http://www.ipcc.ch/pdf/supporting-material/expert-meeting-report-scenarios.pdf (2021) (IPCC, Geneva, 2008) (cit. on p. 36).

56. Riahi, K. *et al.* RCP 8.5—A scenario of comparatively high greenhouse gas emissions. *Climatic Change* **109,** 33. ISSN: 1573-1480. https://doi.org/10.1007/s10584-011-0149-y (2021) (Aug. 13, 2011) (cit. on p. 37).

57. Giorgi, F. *et al.* The Regional Climate Change Hyper-Matrix Framework. *Eos, Transactions American Geophysical Union* **89,** 445–446. ISSN: 2324-9250. https://agupubs.onlinelibrary.wiley.com/doi/abs/10.1029/2008EO450001 (2021) (2008) (cit. on p. 37).

58. Giorgi, F. & Coppola, E. Does the model regional bias affect the projected regional climate change? An analysis of global model projections. *Climatic Change* **100,** 787–795. ISSN: 1573-1480. https://doi.org/10.1007/s10584-010-9864-z (2021) (June 1, 2010) (cit. on pp. 37, 121).

59. Christensen, J. H., Kjellström, E., Giorgi, F., Lenderink, G. & Rummukainen, M. Weight assignment in regional climate models. *Climate Research* **44,** 179–194. ISSN: 0936-577X, 1616-1572. https://www.int-res.com/abstracts/cr/v44/n2-3/p179-194/ (2021) (Dec. 9, 2010) (cit. on pp. 37, 121).

60. Olmos Giménez, P., García Galiano, S. G. & Giraldo-Osorio, J. D. Identifying a robust method to build RCMs ensemble as climate forcing for hydrological impact models. *Atmospheric Research* **174-175,** 31–40. ISSN: 0169-8095. https://www.sciencedirect.com/science/article/pii/S0169809516300035 (2021) (June 15, 2016) (cit. on pp. 37, 121).

61. Giorgi, F. *et al.* RegCM4: model description and preliminary tests over multiple CORDEX domains. *Climate Research* **52,** 7–29. ISSN: 0936-577X, 1616-1572. https://www.int-res.com/abstracts/cr/v52/p7-29/ (2021) (Mar. 22, 2012) (cit. on p. 38).

62. Jones, C. D. *et al.* The HadGEM2-ES implementation of CMIP5 centennial simulations. *Geoscientific Model Development* **4.** Publisher: Copernicus GmbH, 543–570. ISSN: 1991-959X. https://gmd.copernicus.org/articles/4/543/2011/gmd-4-543-2011.html (2021) (July 1, 2011) (cit. on p. 38).

63. Ilyina, T. *et al.* Global ocean biogeochemistry model HAMOCC: Model architecture and performance as component of the MPI-Earth system model in different CMIP5 experimental realizations. *Journal of Advances in Modeling Earth Systems* **5,** 287–315. ISSN: 1942-2466. https://agupubs.onlinelibrary.wiley.com/doi/abs/10.1029/2012MS000178 (2021) (2013) (cit. on p. 39).

64. *EasyBal* 2021. https://h2ogeo.upc.edu/en/investigation-hydrogeology/software/147-easybal-en (2021) (cit. on pp. 41, 55).

65. Guo, Z. *EasyBal Water Balance Calculations for 1995-2005 over Wanzhou County, China.* 2021 (cit. on pp. 41, 57–59, 117).

66. Fischer, M., Rust, H. W. & Ulbrich, U. Seasonal Cycle in German Daily Precipitation Extremes. *Meteorologische Zeitschrift.* Publisher: Schweizerbart'sche Verlagsbuchhandlung, 3–13. ISSN: , https://www.schweizerbart.de/papers/metz/detail/27/88248/Seasonal_Cycle_in_German_Daily_Precipitation_Extre?af=crossref (2021) (Jan. 29, 2018) (cit. on pp. 41, 118).

67. Rust, H. W., Maraun, D. & Osborn, T. J. Modelling seasonality in extreme precipitation. *The European Physical Journal Special Topics* **174,** 99–111. ISSN: 1951-6401. https://doi.org/10.1140/epjst/e2009-01093-7 (2021) (July 1, 2009) (cit. on pp. 41, 118).

68. Delignette-Muller, M. L. & Dutang, C. fitdistrplus: An R Package for Fitting Distributions. *Journal of Statistical Software* **64.** Number: 1, 1–34. ISSN: 1548-7660. https://www.jstatsoft.org/index.php/jss/article/view/v064i04 (2021) (Mar. 20, 2015) (cit. on p. 42).

69. Laio, F. Cramer–von Mises and Anderson-Darling goodness of fit tests for extreme value distributions with unknown parameters. *Water Resources Research* **40.** ISSN: 1944-7973. https://agupubs.onlinelibrary.wiley.com/doi/abs/10.1029/2004WR003204 (2021) (2004) (cit. on pp. 43, 44).

70. Marsaglia, G. & Marsaglia, J. Evaluating the Anderson-Darling Distribution. *Journal of Statistical Software* **9.** Number: 1, 1–5. ISSN: 1548-7660. https://www.jstatsoft.org/index.php/jss/article/view/v009i02 (2021) (Feb. 25, 2004) (cit. on p. 43).

71. Xu, L. & Wang, A. Application of the Bias Correction and Spatial Downscaling Algorithm on the Temperature Extremes From CMIP5 Multimodel Ensembles in China. *Earth and Space Science* **6,** 2508–2524. ISSN: 2333-5084. https://agupubs.onlinelibrary.wiley.com/doi/abs/10.1029/2019EA000995 (2021) (2019) (cit. on pp. 46, 107, 120, 121).

72. Cannon, A. J., Sobie, S. R. & Murdock, T. Q. Bias Correction of GCM Precipitation by Quantile Mapping: How Well Do Methods Preserve Changes in Quantiles and Extremes? *Journal of Climate* **28.** Publisher: American Meteorological Society Section: Journal of Climate, 6938–6959. ISSN: 0894-8755, 1520-0442. https://journals.ametsoc.org/view/journals/clim/28/17/jcli-d-14-00754.1.xml (2021) (Sept. 1, 2015) (cit. on p. 46).

73. Maraun, D. Bias Correcting Climate Change Simulations - a Critical Review. *Current Climate Change Reports* **2,** 211–220. ISSN: 2198-6061. https://doi.org/10.1007/s40641-016-0050-x (2021) (Dec. 1, 2016) (cit. on p. 47).

74. Kim, S., Shin, J.-Y., Ahn, H. & Heo, J.-H. Selecting Climate Models to Determine Future Extreme Rainfall Quantiles. *Journal of the Korean Society of Hazard Mitigation* **19.** Publisher: Korean Society of Hazard Mitigation, 55–69. ISSN: 1738-2424, 2287-6723. http://www.j-kosham.or.kr/journal/view.php?doi=10.9798/KOSHAM.2019.19.1.55 (2021) (Feb. 28, 2019) (cit. on p. 47).

75. Durman, C. F., Gregory, J. M., Hassell, D. C., Jones, R. G. & Murphy, J. M. A comparison of extreme European daily precipitation simulated by a global and a regional climate model for present and future climates. *Quarterly Journal of the Royal Meteorological Society* **127,** 1005–1015. ISSN: 1477-870X. https://rmets.onlinelibrary.wiley.com/doi/abs/10.1002/qj.49712757316 (2021) (2001) (cit. on p. 47).

76. Li, J., Wasko, C., Johnson, F., Evans, J. P. & Sharma, A. Can Regional Climate Modeling Capture the Observed Changes in Spatial Organization of Extreme Storms at Higher Temperatures? *Geophysical Research Letters* **45,** 4475–4484. ISSN: 1944-8007. https://agupubs.onlinelibrary.wiley.com/doi/abs/10.1029/2018GL077716 (2021) (2018) (cit. on p. 48).

77. Kim, S., Joo, K., Kim, H., Shin, J.-Y. & Heo, J.-H. Regional quantile delta mapping method using regional frequency analysis for regional climate model precipitation. *Journal of Hydrology* **596,** 125685. ISSN: 0022-1694. https://www.sciencedirect.com/science/article/pii/S002216942031146X (2021) (May 1, 2021) (cit. on pp. 48, 49).

78. Nguyen, H., Mehrotra, R. & Sharma, A. Can the variability in precipitation simulations across GCMs be reduced through sensible bias correction? *Climate Dynamics* **49,** 3257–3275. ISSN: 1432-0894. https://doi.org/10.1007/s00382-016-3510-z (2021) (Nov. 1, 2017) (cit. on p. 49).

79. Maraun, D. & Widmann, M. Cross-validation of bias-corrected climate simulations is misleading. *Hydrology and Earth System Sciences* **22.** Publisher: Copernicus GmbH, 4867–4873. ISSN: 1027-5606. https://hess.copernicus.org/articles/22/4867/2018/ (2021) (Sept. 18, 2018) (cit. on p. 50).

80. Koutsoyiannis, D. Statistics of extremes and estimation of extreme rainfall: I. Theoretical investigation. *Hydrological Sciences Journal* **49,** 3. ISSN: 0262-6667, 2150-3435. https://www.tandfonline.com/doi/full/10.1623/hysj.49.4.575.54430 (2021) (Aug. 2004) (cit. on pp. 95, 118).

81. Sandvik, M. I., Sorteberg, A. & Rasmussen, R. Sensitivity of historical orographically enhanced extreme precipitation events to idealized temperature perturbations. *Climate Dynamics* **50,** 143–157. ISSN: 1432-0894. https://doi.org/10.1007/s00382-017-3593-1 (2021) (Jan. 1, 2018) (cit. on p. 108).

82. Napoli, A., Crespi, A., Ragone, F., Maugeri, M. & Pasquero, C. Variability of orographic enhancement of precipitation in the Alpine region. *Scientific Reports* **9,** 13352. ISSN: 2045-2322. https://www.nature.com/articles/s41598-019-49974-5 (2021) (Sept. 16, 2019) (cit. on p. 108).

83. Miura, T. & Nagai, S. Landslide Detection with Himawari-8 Geostationary Satellite Data: A Case Study of a Torrential Rain Event in Kyushu, Japan. *Remote Sensing* **12.** Number: 11 Publisher: Multidisciplinary Digital Publishing Institute, 1734. https://www.mdpi.com/2072-4292/12/11/1734 (2021) (Jan. 2020) (cit. on p. 117).

84. Tseng, C.-W. *et al.* Application of High-Resolution Radar Rain Data to the Predictive Analysis of Landslide Susceptibility under Climate Change in the Laonong Watershed, Taiwan. *Remote Sensing* **12.** Number: 23 Publisher: Multidisciplinary Digital Publishing Institute, 3855. https://www.mdpi.com/2072-4292/12/23/3855 (2021) (Jan. 2020) (cit. on p. 117).

85. Kumar, P. *et al.* Towards an operationalisation of nature-based solutions for natural hazards. *Science of The Total Environment* **731,** 138855. ISSN: 0048-9697. https://www.sciencedirect.com/science/article/pii/S004896972032372X (2021) (Aug. 20, 2020) (cit. on p. 119).

86. Wood, A. W., Leung, L. R., Sridhar, V. & Lettenmaier, D. P. Hydrologic Implications of Dynamical and Statistical Approaches to Downscaling Climate Model Outputs. *Climatic Change* **62,** 189–216. ISSN: 1573-1480. https://doi.org/10.1023/B:CLIM.0000013685.99609.9e (2021) (Jan. 1, 2004) (cit. on p. 120).